

**UNIVERSITY OF SOUTHERN QUEENSLAND**

**Variability and Change of the Indo-Pacific Climate System and  
their Impacts upon Australia Rainfall**

**A Dissertation submitted by**

**Ge Shi**

**For the award of**

**Doctor of Philosophy**

**2008**

## **Abstract**

Australia is one of the driest continents in the world, and over the past decades, severe drought has plagued most of the country. Water security is an important national issue. The ultimate water supply, rainfall, however, is one of the most variable ones in the world and is complicated by the fact that it is affected by several remote ocean-atmospheric teleconnection systems simultaneously, including the El Niño-Southern Oscillation, the Indian Ocean Dipole and Southern Hemisphere oceanic and atmospheric variability. These three systems sometimes conspire to produce a severe impact, whereas sometimes they offset each other to produce a mild influence. The recent severe water shortage has generated a surge of investments with strong regional applications. The present study focuses on areas and issues outside the scope of these regional studies, aiming to provide an Australia-wide assessment of future Australian rainfall under climate change. Firstly, we unravel a process of the Indo-Pacific oceanic teleconnection and examine its role in influencing variability of the Indian Ocean, and hence Australian rainfall variations. An examination of their contribution to the warming structure of the Indian Ocean is carried out. Secondly, we explore dynamics of North West Australian rainfall variability and mechanisms of a rainfall increase over the past decades, and benchmark climate models in terms of their ability to reproduce the observed variability and trends, focusing on the role of increasing northern hemispheric aerosols in the rainfall increase. Thirdly, we provide a dynamical explanation to the common future of a fast Tasman Sea warming rate under climate change, and identify the impacts of such warming on Australian rainfall. Finally, we examine the relative importance of the three systems, in addition to Tasman Sea warming, in driving rainfall changes under greenhouse conditions. This project contributes to no less than six peer-reviewed journal publications.

## **Certification of Dissertation**

I certify that the ideas, experimental, results, analyses, software and conclusions reported in this dissertation are entirely my own effort, except where otherwise acknowledged. I also certify that the work is original and has not been previously submitted for any other award, except where otherwise acknowledged.

\_\_\_\_\_  
Signature of Candidate

\_\_\_\_\_  
Date

ENDORSEMENT

\_\_\_\_\_  
Signature of Supervisor/s

\_\_\_\_\_  
Date

## **Acknowledgement**

I am ever so grateful to my supervisor, Dr. J. Ribbe, for his guidance, encouragement and support. I sincerely thank the University of Southern Queensland for a scholarship over the past two years, which accelerates the completion of this project. I am indebted to CSIRO Marine and Atmospheric Research for providing a host of my research, and more importantly a world-class research environment, in which I was able to interact and collaborate with many inspiring scientists, particularly, my supervisors Drs Brian Ryan and Ian Smith, and access the modern computing facility and outputs of the CSIRO climate models.

## List of Content

Chapter 1: Introduction .....	1
1.1 Australia's major climate drivers: The Three-headed dog .....	1
1.1.1 ENSO .....	1
1.1.2 The IOD .....	2
1.1.3 The SAM .....	3
1.2 Long-term rainfall trends over Australia .....	3
1.3 Foci of the present project .....	5
1.3.1 Indo-Pacific transmission and impact on Australian rainfall .....	5
1.3.1.1 Current knowledge .....	5
1.3.1.2 Scope .....	8
1.3.2 Dynamics of NWA rainfall variability and change .....	8
1.3.2.1 Current knowledge .....	8
1.3.2.2 Scope .....	10
1.3.3 The future of Australian rainfall .....	11
1.3.3.1 Current knowledge .....	11
1.3.3.2 Scope .....	13
1.4 Summary .....	13
Chapter 2: Data and Methodologies .....	15
2.1 Data .....	15
2.1.1 Observations and reanalyses .....	15
2.1.2 Climate models and outputs .....	16
2.2 Methodologies .....	17
2.2.1 Empirical Orthogonal Function (EOF) .....	17
2.2.2 CEOFs and Statistical Significance of Monthly and Filtered Time Series .....	20
2.2.3 Projections of spatially and temporally varying data onto a pattern ...	24
2.2.4 Godfrey's island rule models .....	24
Chapter 3: Indo-Pacific teleconnection .....	31
3.1 Background .....	31
3.1.1 Teleconnection between EIO SST and SEA rainfall .....	31
3.1.2 The Indo-Pacific teleconnection .....	32
3.1.3 Details of data used .....	32
3.2 Indo-Pacific transmission in the Post-1980 period .....	33
3.2.1 ENSO discharge/recharge signals within the Indo-Pacific system..	33
3.2.2 the off-equatorial NP ray-path .....	35
3.3 Comparison between the pre-1980 and post-1980 period .....	39
3.3.1 Data quality of SODA-POP .....	39
3.3.2 Decadal difference of the Indo-Pacific transmission .....	40
3.3.3 Decadal difference of the importance of the off-equatorial NP pathway .....	43
3.3.4 The dynamics for the decadal difference .....	44
3.4 Contribution of decadal differences to Indian Ocean temperature trends	47
3.5 Summary .....	48

Chapter 4: NWA rainfall variability and trends .....	50
4.1 Background .....	50
4.2 Specific detail of Data, methodology, and model experiments .....	52
4.3 Observed trend and variability of NWA rainfall .....	53
4.3.1 Seasonal stratification of trends and variability .....	53
4.3.2 Variability of DJF rainfall and Indo-Pacific SSTs .....	58
4.3.3 The dynamics of the observed DJF rainfall trend .....	64
4.4 Model rainfall variability and trend .....	67
4.4.1 Seasonal stratification of trends and variability .....	67
4.4.1.1 Seasonal trends .....	67
4.4.1.2 Seasonal correlation between NWA rainfall and global SST .....	69
4.4.1.3 Seasonal correlation between NWA rainfall with EIO SST and Niño3.4 .....	71
4.4.2 Variability of DJF rainfall .....	71
4.4.2.1 EOF of DJF SST in the Indian Ocean .....	71
4.4.2.2 Rainfall EOF in DJF without ENSO and IOD .....	75
4.4.2.3 Circulation pattern associated with DJF rainfall EOFs .....	76
4.4.3 Dynamics of DJF model rainfall trend with increasing aerosols .....	76
4.5 Discussion .....	80
Chapter 5: The future of Australian rainfall .....	84
5.1 Background .....	84
5.2 Dynamics of Tasman warming .....	86
5.3 Dynamics of SEA rainfall variability and change .....	90
5.3.1 Changes in summer and winter rainfall in the CSIRO model .....	90
5.3.2 Australian rainfall teleconnection in the control climate .....	92
5.3.2.1 Tasman Sea temperature anomalies and Australian rainfall .....	93
5.3.2.2 The impact of ENSO .....	95
5.3.2.3 The impact of IOD .....	96
5.3.2.4 The impact of the SAM .....	96
5.4 Interpretation of rainfall changes .....	99
5.4.1 Summer rainfall change .....	100
5.4.2 Winter rainfall change .....	101
5.5 Summary and discussion .....	103
Chapter 6: Conclusions .....	105
6.1 Indo-Pacific oceanic teleconnection .....	105
6.2 Dynamics of NWA rainfall variability and trend .....	106
6.3 Australian rainfall under a changing climate .....	107
6.4 Future directions .....	107
References .....	109
List of Figures .....	123
Appendix: Glossary and Acronyms .....	129

# Chapter 1: Introduction

## 1.1 Australia's major climate drivers: The Three-headed dog

Australia is one of the driest continents in the world, and any factors that affect the frequency and intensity of rainfall (hence the water supply) must be explored. Australian climate variability is influenced by the El Niño-Southern Oscillation (ENSO) in the Pacific Ocean, the Indian Ocean Dipole (IOD) of the Indian Ocean (IO), and the Southern Annular Mode (SAM) of the Southern Hemisphere. The three systems can be identified from sea surface temperature (SST) and mean sea level pressure (MSLP). These three systems sometimes conspire to produce a severe impact, whereas sometimes they offset each other to produce a mild influence.

### 1.1.1 ENSO

The term El Niño (La Niña) refers to a periodic warming (cooling) in SST across the central and east-central equatorial Pacific Ocean (Figure 1.1, upper left). The phrase Southern Oscillation describes coherent variations of MSLP between Tahiti and Darwin (Philander, 1990). When MSLP is higher than normal in Darwin, MSLP pressure in Tahiti is lower than normal. ENSO was coined in the early 1980s in recognition of an intimate linkage between El Niño events and the Southern Oscillation, which prior to the late 1960s had been viewed as two unrelated phenomena. The global ocean-atmosphere phenomenon to which this term applies is sometimes referred to as the “ENSO cycle.”

ENSO is associated with droughts and floods in many parts of the globe (Philander, 1990; Kiladis and Diaz, 1989). Rainfall variations over the Australian continent, especially north-eastern Australia, have been found to be significantly influenced by ENSO events (Pittock, 1975; Nicholls and Woodcock, 1981; Smith, 2004). But some El Niño events have severe impacts while some produce a mild influence. Despite great advances in ENSO theories, the underlying causes for the varying impacts are not clear.

### 1.1.2 The IOD

Recent studies (Saji et al., 1999; Webster et al., 1999; Allan et al., 2001) have discovered an El Niño-like SST anomaly pattern in the IO – the so-called IOD. It refers to the episodic occurrence of an anomalous zonal gradient in SST across the equatorial IO and related changes in the topography of the thermocline. During a positive IOD event, SST drops in the southeastern part of the IO and off the northern coast of Australia. At the same time, SST rises in the western equatorial IO (Figure 1.1, upper right). This SST change leads to heavy rainfall over the east Africa and droughts over northwest and southeast of Australia. The relationship between IOD and ENSO has not been fully explored. Some El Niño events develop with an accompanying positive IOD event, whereas some with a negative IOD event.

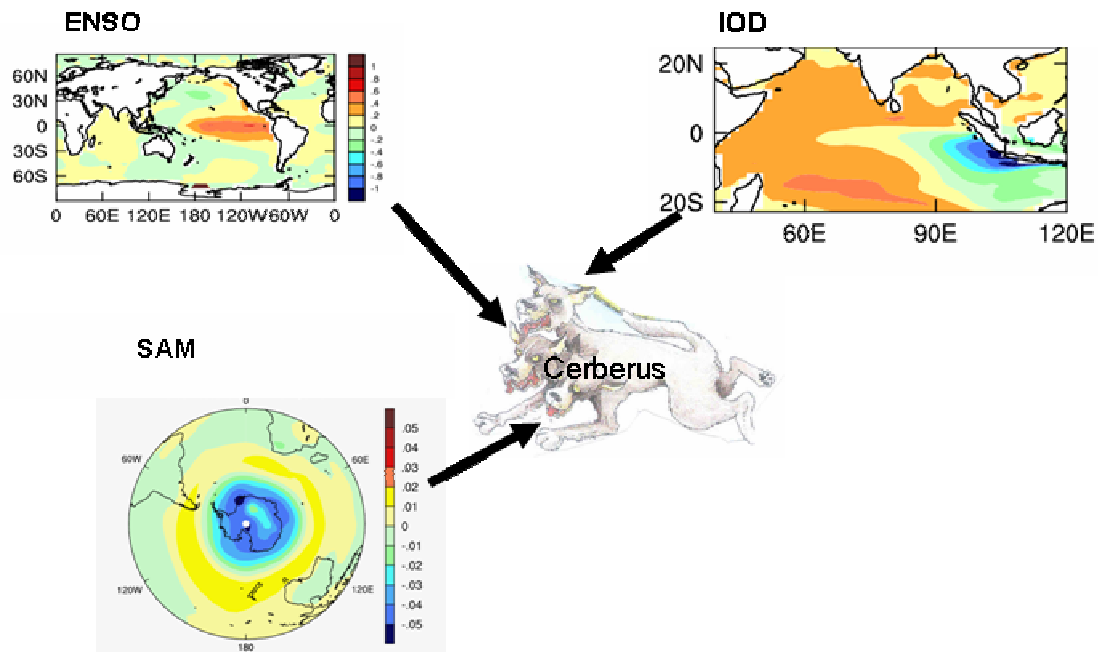


Figure 1.1: Cerberus (three-headed dog) of the Australian Climate: one head is ENSO (higher temperature in the equatorial Pacific), the second head is the IOD (higher temperature in the west and lower in the east of the IO), and the third head is the SAM (oscillating MSLP between high and midlatitudes). The ENSO anomaly pattern is obtained by regressing SST anomalies using Globe Sea Ice and Sea Surface Temperature data (GISST, Rayner et al., 1996) on an ENSO index, Niño3.4, which is defined as SST anomaly averaged over 170°W-120°W, 5°S -5°N. The IOD anomaly pattern is obtained from an empirical orthogonal function (EOF) analysis on SST anomalies, and the SAM is defined as the EOF1 of MSLP anomaly from the National Center for Environmental Predictions (NCEP) reanalysis (Kalnay et al., 1996). (Courtesy of Wenju Cai).

There are two pathways for the inter-basin exchange within the Indo-Pacific system. One takes place through the Indonesian Throughflow Passage (tropical pathway), and the other, via a flow of the East Australia Current (EAC) through the Tasman Sea, which then veers northwestward feeding into the subtropical gyre of the southern IO and Atlantic (subtropical pathway). These flows are intimately linked to variations of the Southern Ocean circulation. One of the major processes controlling the relationship between ENSO and IOD is the oceanic teleconnection through the Indonesian Throughflow, in particular, the way in which ENSO signals are transmitted to the IO.

### 1.1.3 The SAM

Another driver of Australian rainfall variability, particularly over the southern part of Australia is the SAM, which is the dominant mode of variability of the Southern Hemisphere atmospheric circulation, operating on all time scales (Kidson, 1988; Thompson and Wallace, 2000). It involves opposite variations of MSLP (and geopotential height) between middle and high latitudes (Figure 1.1, lower panel). Rainfall variability at middle latitudes associated with the SAM could interfere with the influence from the Indian-Pacific system and must also be investigated.

The three systems are often referred as the “three-headed dog” (Cerberus, an ancient Greek myth) of the Australian climate (Figure 1.1). Given that climate change signals mainly project onto existing modes of variability, trends of the three modes of variability may contribute to the rainfall trend over Australia.

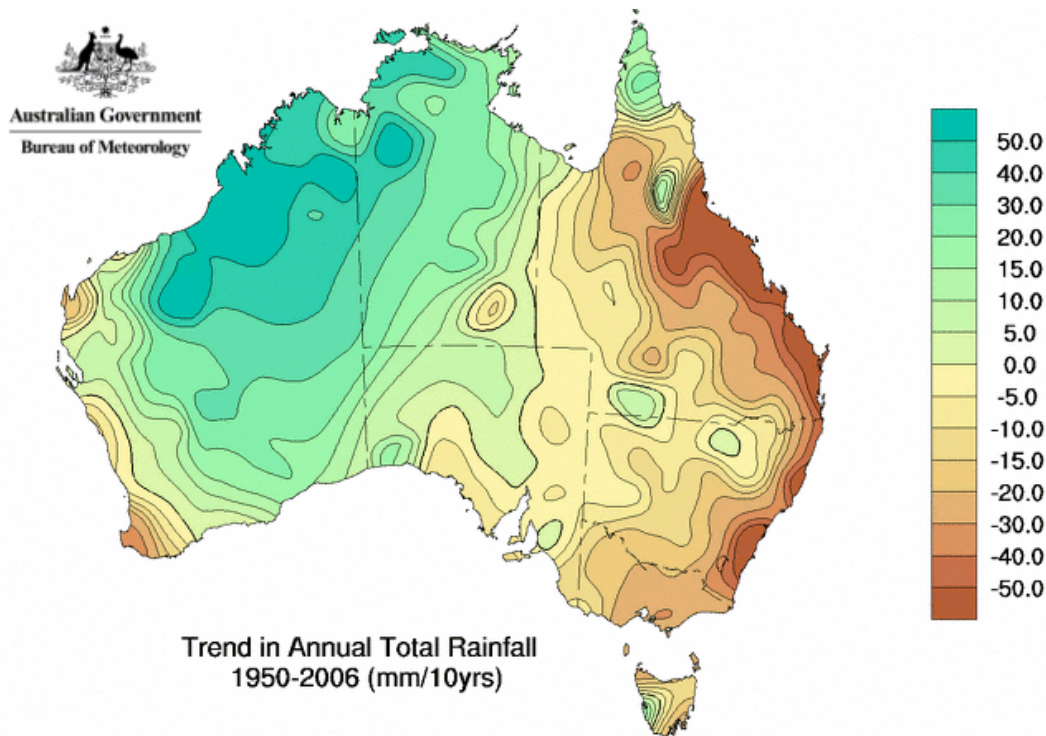


Figure 1.2: Total rainfall trend over the period 1950-2002 (courtesy of BMRC).

## 1.2 Long-term rainfall trends over Australia

Rainfall trends using half century-long rainfall record of the Bureau of Meteorological Center (BMRC) is plotted in Fig. 1.2. A disturbing feature is that in many densely

populated regions rainfall decreases, particularly over eastern and southwest West Australia (SWWA). While part of the trends is simply due to multi-decadal scale variability, if these trends continue, it has important implications for water resource management across Australia.

Significant efforts have been directed to understanding the cause of some of the trends. For example, the observed rainfall decreases along the east Australia coast may reflect an increased frequency of El-Niño events in the late 20th century, which could be related to an increase in greenhouse gases; indeed, coupled atmosphere-ocean general circulation models (GCMs) forced by increasing atmospheric CO<sub>2</sub> have simulated an El-Niño-like warming pattern in the Pacific Ocean (e.g., Meehl and Washington, 1995; Cai and Whetton, 2000). This suggests the possibility that the observed rainfall decrease might be attributable to an El Niño-like warming pattern, and that future average rainfall might be lower over eastern Australia. To the west, rainfall over SWWA may be in part linked to a shift of the SAM towards its “positive” state, with decreased MSLP over Antarctica and increased MSLP over the SH midlatitudes (Cai et al., 2003a; Cai and Cowan, 2006). It may also be linked to multi-decadal variability of the SAM (Cai et al., 2005a), and to land-cover change (Pitman et al., 2004). One such robust feature of the Southern Hemisphere (SH) response of coupled GCMs to an increase of greenhouse gases is a strengthening (weakening) of the circumpolar (midlatitude) westerlies. (Fyfe et al., 1999; Kushner et al., 2001; Cubasch et al., 2001; Cai et al., 2003a). However, as with interannual rainfall variations, the relative importance of the contributions from the trends in the three systems is not clear.

As shown in Fig. 1.2, there has been an overall positive trend in rainfall over North West Australia (NWA). In an environment in which decadal-scale droughts have plagued most of the country, and the long-term rainfall over southern Australia is projected to decrease further, continued upward trends in NWA rainfall may provide a source of future water resources in NWA. However, the dynamics governing the rainfall increase is not fully understood. There is evidence that the upward trend in the SAM index has caused considerable changes in ocean circulation (Cai et al., 2005b). Will this in turn, modulate the rainfall response?

### **1.3 Foci of the present project**

Based on an extensive literature review, focus will be placed on three areas:

- 1) Indo-Pacific transmission and impact on Australian rainfall. Variability in the IO affects Australian rainfall (Ashok et al., 2003), which is in turn influenced by ENSO through atmospheric teleconnection as proposed by Annamalai et al. (2005), who argued that IOD events since 1980s are stronger due to the stronger atmospheric teleconnection. A less understood process is the transmission of

ENSO signals into the IO via oceanic teleconnection. We will focus on the decadal-scale variability of the process and the impacts on Australian rainfall.

- 2) Dynamics of the NWA rainfall trends. This is an area in which our knowledge is virtually void, but the robustness of the water abundance is very important because it could provide a resource to alleviate Australia's water shortage.
- 3) The future of Australian rainfall, in terms of the response of climate drivers and their teleconnection with Australian rainfall to climate change forcing. This will take into account that the net rainfall change in the future will be a consequence of both super-imposing effects and offsetting influences by the three climate engines.

In the following sections, current status of the research in each of the areas is described; the knowledge gaps in which contribution can be made are identified.

### **1.3.1 Indo-Pacific transmission and impact on Australian rainfall**

This area concerns the tropical pathway of the Indo-Pacific exchange. Statistical analyses of historical SST records (e.g., Pan and Oort, 1983, 1990; Kiladis and Diaz, 1989; Hastenrath et al., 1993; Kawamura, 1994; Tourre and White, 1995; Lanzante, 1996; Nicholson, 1997; Harrison and Larkin, 1998; Klein et al., 1999; Enfield and Mestas-Nun˜ez, 1999; Larkin and Harrison, 2001) have indicated that the surface conditions of the IO are related to ENSO events. Some of these studies reported that the strongest SST anomalies in IO typically appear several months after the mature phase of the ENSO signal in the central equatorial Pacific. But there are few studies dealing with ways in which ENSO signals are transmitted from the Pacific into the IO. The location where the Pacific Ocean signals end up, however, affects variability in the IO, which in turn influences rainfall variability over south-eastern Australia. The objective is to address this issue by utilizing available oceanic reanalysis data and reconstructed sea level data, which is a surrogate for oceanic heat content, recently made available.

#### **1.3.1.1 Current knowledge**

While rainfall in north-eastern Australia (e.g. Queensland) is found to be mainly affected by SST anomalies of the equatorial eastern Pacific Ocean region, there is no doubt that variability of the eastern IO (EIO) SST has a great impact on the rainfall over Australia's southeastern states (Smith, 1993; Smith et al, 2000; Ansell et al, 2000). This is illustrated in Figure 1.3, which compares the relationship of rainfall over the important region of Murray Darling Basin (MDB) with EIO SST anomalies and with ENSO ( Ni˜no 3.4 index). The left panel of the figure is a scatter plot of rainfall anomalies over the MDB region and SST anomalies of the EIO, with the regression line superimposed. The rainfall anomalies are obtained from data provided by BMRC, while SST anomalies data is from GISST. The slope is an indication of the strength of their relationship. The right panel of Figure 2 describes a similar relationship between MDB rainfall and ENSO.

SST anomalies in the EIO are dominated by IOD events in the IO. This discovery has raised a number of new questions about its generation and possible interactions with other climate phenomena such as ENSO. An IOD (Saji et al., 1999; Webster et al., 1999) episode usually begins with anomalous cooling in the tropical EIO during May–June, when enhanced surface easterlies generate an anomalously shallow thermocline, enhanced latent heat flux, and upwelling off the Sumatra–Java coast. The cold anomaly usually peaks in September–October, by which time the western IO has warmed as a result of increased insolation, reduced evaporation, and deepened thermocline. The demise of an IOD often occurs soon after the Australian summer monsoon commences in December, when the mean winds become westerly in the equatorial EIO. The induced easterly anomalies then act to reduce the wind speed. Reduced latent heat flux alone with increased surface shortwave radiation acts to warm the EIO, yielding basin-scale warm anomalies. This seasonality in the evolution of the IOD is often referred to as the seasonal phase-locking feature. Development of an IOD, typically, but not always, accompanies development of an El Niño in the Pacific Ocean.

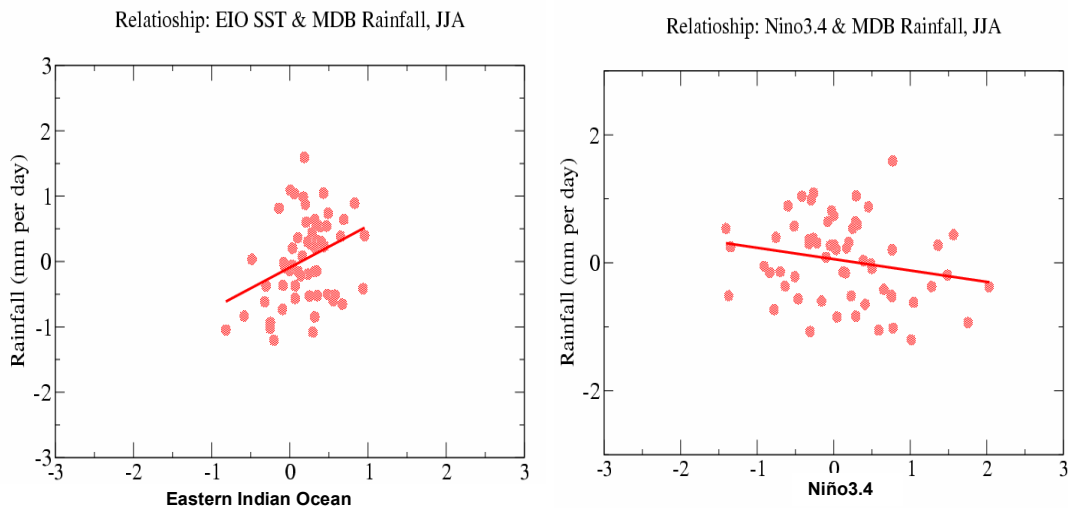


*Figure 1.3: Relationship between winter rainfall anomalies over MDB region and winter EIO SST anomalies (averaged over an area bounded by 5°S–10°S and 100°E–110°E), and between winter rainfall anomalies over MDB region and winter Niño3.4 index. The figure shows that for MDB region, the winter rainfall is influenced more by SST in the EIO.*

The Indo-Pacific linkage in terms of tropical oceanic teleconnection is via the Indonesian Throughflow (Meyers, 1996; Potemra, 2001), which is a system of surface currents flowing from the Pacific to the IO through the Indonesian seas. It is the only flow

between the ocean basins at low latitudes and, consequently, plays an important role in the meridional transport of heat in the climate system, all the more so since this transport originates from the warm-pool of the Pacific Ocean and enters into the colder waters of the South Equatorial Current of the IO.

The variability of Indonesian Throughflow and its linkage with ENSO has long been a subject of great interest. Wyrki (1987) compared the sea level measured at Davao (Philippines) and Darwin (Australia). He noticed that while there are variations of sea level at both ends of the throughflow, the difference between these levels remains almost constant. According to Barnett (1983), the convergence of surface winds over Indonesia is subject to strong interannual variations in its intensity and location because of the coupling of the trade winds over the Pacific with monsoons over the IO. A strong convergence of the wind field is associated with a high state of the Southern Oscillation Index, i.e. a La Niña phase, sea level rises both in the EIO and in the western Pacific Ocean. During a low state of Southern Oscillation Index, i.e., an El Niño, winds are divergent over Indonesia, and sea level drops on both sides of the Indonesian archipelago. These characteristics of the wind field imply that the difference of sea level between the western Pacific and the EIO is only weakly affected by the principal wind patterns associated with ENSO. Wyrki attributes the slow interannual variations of the sea level difference between Davao and Darwin to fluctuations in the wind field which are not associated with the Southern Oscillation, or may be due to uncertainties in the sea level records themselves.

However, Clarke and Liu (1994) suggest that the volume transport of throughflow is expected to vary during ENSO, with a larger than normal transport during La Niña, when strong easterlies along the equatorial Pacific Ocean build up high sea level in the western Pacific. In theory, the Pacific Ocean signal is regarded to be transmitted to the north-western coast of Australia and influences the throughflow by geostrophy by the difference in sea level between the Indian and Pacific Ocean. Clark and Liu argue that Wyrki (1987) did not use a sea level difference that is representative of the relevant pressure gradient due to the choice of Darwin to representing the IO. Darwin is, in fact, representative of the Pacific Ocean during ENSO cycle. The difference between Davao and the southern coast of Java is a more appropriate gradient to measure the Pacific to IO pressure gradient. Meyers (1996) studied the observed data from the expendable bathythermograph (XBT) line between Fremantle and Sumatra. He concluded that the ENSO signal that appears on the northwestern coast of Australia is forced by winds in the equatorial Pacific. He also proposed that thermocline variations along the Java coast are driven by zonal wind: easterly wind anomalies over the equatorial IO are associated with shallow thermocline and colder waters.

Recently, Cai et al. (2005c) found that the north Pacific (NP) Ocean is involved in the transmission of ENSO signals to the IO. The Pacific signals arrive at the central Western Australia (WA) coast. They showed that the signal propagates through an off-equatorial NP ray-path, whereby the anomaly, after an initial development near Hawaii, propagates

westward as a Rossby wave. Upon impinging on the western boundary, it moves equatorward along the Kelvin-Munk ray-path proposed by Godfrey (1975), and reflects as an equatorial Kelvin wave. As the reflected Kelvin wave propagates eastward, it impinges on the Australasian continent and moves poleward along the WA coast as a coastally-trapped wave, radiating Rossby waves into the south IO (Wijffels and Meyers, 2004). Along the above path, the NP anomaly reaches the central WA coast some 9 months later. On-route to the WA coast the anomaly is reinforced by evolving winds associated with ENSO.

Coupled climate models have largely been unable to simulate the transmission process of ENSO signals from the Pacific into the IO (Cai et al., 2005d). The underlying cause is not clear yet. The likelihood that the process is non-stationary needs to be investigated.

### **1.3.1.2 Scope**

While much of the focus of recent research has been on the ENSO linkage to the IO on interannual time scales, analysis so far has largely been limited to the period since 1980 due to limitations of available data. Multidecadal variability of the linkage has not been explored. Since the mid-1970s, climate has been known to shift to a state considerably different from that prior to mid-1970s (IPCC, 2007; Hartmann, 1994; Hurrell and Trenberth, 1996). Our hypothesis is that associated with this climate shift, the statistical relationship between variability in the Indian and the Pacific Ocean may undergo a significant change. Understanding the physical processes responsible for these changes is crucial for realistic simulations of the Indo-Pacific dynamics in coupled climate models, for assessing their climate impacts, and for detection of climate change signals. Recent reconstructed oceanic analysis will enable such a study to proceed.

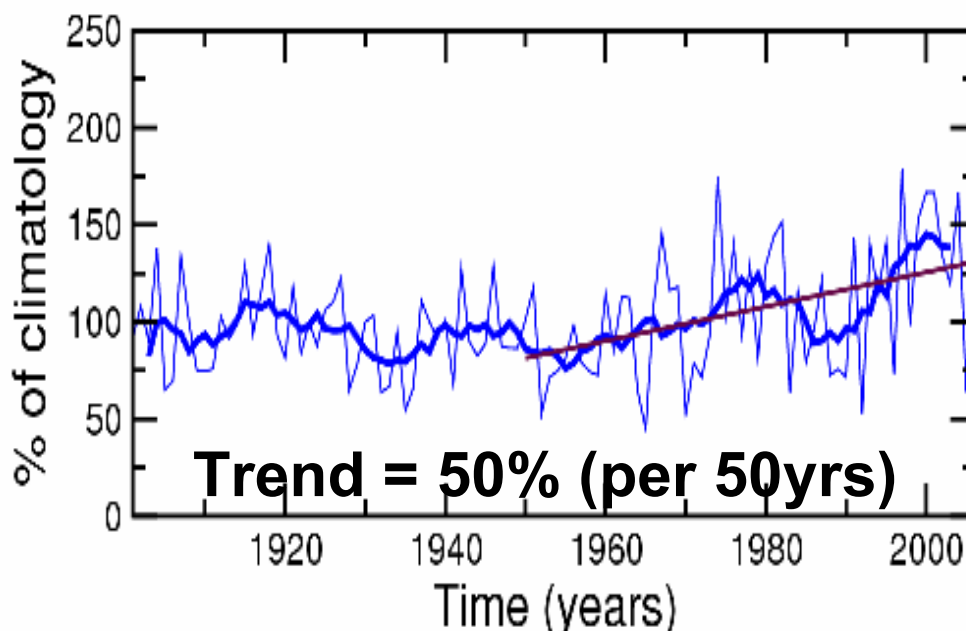
## **1.3.2 Dynamics of NWA rainfall variability and change**

Figure 1.2 shows that, in sharp contrast to significant drying trends in other regions of the country, there has been an overall positive trend in rainfall over NWA. The observed annual increase is approximately 50% of the climatological value (Fig. 1.4). Policy makers are considering a northern development, to take advantage of the water abundance. However, a detailed knowledge of climate processes governing its stability under a changing climate is still lacking. We will examine the dynamics of observed rainfall variability and trends, benchmark the performance of available climate models focusing on role of anthropogenic forcing in driving the observed trend, and identify model deficiencies so as to improve projection of future NWA rainfall changes.

### **1.3.2.1 Current knowledge**

Considerable effort has been made to understand the dynamics of the drying trend over a number of Australian regions (e.g., Smith, 2004; Cai and Cowan, 2006). For example, the observed rainfall decreases along the east Australia coast may reflect an increased frequency of El-Niño events in the late 20th century, which could be related to an increase in greenhouse gases; indeed, coupled atmosphere-ocean GCMs forced by

increasing atmospheric CO<sub>2</sub> have simulated an El-Niño-like warming pattern in the Pacific Ocean (e.g., Meehl and Washington, 1995; Cai and Whetton, 2000). This suggests the possibility that the observed rainfall decrease might be attributable to an El Niño-like warming pattern, and that future average rainfall might be lower over eastern Australia. To the west, rainfall over SWWA may be in part linked to a shift of the SAM towards its “positive” state, with decreased MSLP over Antarctica and increased MSLP over the SH midlatitudes (Cai et al., 2003a; Cai and Cowan, 2006). It may also be linked to multi-decadal variability of the SAM (Cai et al., 2005a), and to land-cover change (Pitman et al., 2004). One such robust feature of the SH response of coupled GCMs to an increase of greenhouse gases is a strengthening (weakening) of the circumpolar (midlatitude) westerlies. (Fyfe et al., 1999; Cubasch et al., 2001; Cai et al., 2003a).



*Figure 1.4: Time series of summer NWA rainfall in terms of percentage of climatology. NWA is defined as the area of 110°E-130°E, 10°S-20°S.*

By contrast, there is relatively little understanding of the dynamics of NWA rainfall variability and trends. Two recent studies have shed some light. Wardle and Smith (2004) hypothesized that during the latter half of the 20th century, the observed increase in temperature gradient between Australia and neighbouring oceans drove a stronger monsoonal circulation. They found that by artificially altering this contrast through a change to the land albedo in a model, they could simulate an increase in rainfall over the entire continent, with stronger totals over the north. Their experiment also resulted in a

temperature response similar to the observed. They concluded that the temperature changes were possibly leading to a strengthening of the monsoon and that this was the cause of the increased rainfall. However, the prescribed changes were much larger than could be justified based on current knowledge, so the authors left the cause of the land-ocean temperature contrast as an open question.

An alternative explanation for the increased northwest rainfall was provided by Rotstayn et al. (2007) who, by using simulations from a low resolution coupled GCM, demonstrated that including (excluding) anthropogenic aerosol changes in 20th century gives increasing (decreasing) rainfall and cloudiness over Australia during 1951–1996. Rotstayn et al. (2007) showed that the pattern of increasing rainfall when aerosols are included is strongest over NWA, in agreement with the observed trends. The strong impact of aerosols is predominantly due to the massive Asian aerosol haze, as confirmed by a sensitivity test in which only Asian anthropogenic aerosols are included. The Asian haze alters the north-south temperature and pressure gradients over the tropical IO in the model, thereby increasing the tendency of monsoonal winds to flow towards Australia.

The argument of an impact from aerosols seems to be supported by the fact that transient climate model simulations forced only by increased greenhouse gases, without the inclusion of aerosol forcing, have generally not reproduced the observed rainfall increase over northwestern and central Australia. Whetton et al. (1996) compared rainfall changes in five enhanced greenhouse climate simulations that used coupled GCMs, and five that used atmospheric GCMs with mixed-layer ocean models. The coupled experiments mostly gave a decrease in summertime rainfall over northwestern and central Australia, whereas the mixed-layer experiments mostly gave an increase (in better agreement with the observed 20th century trends). They attribute the difference to the coupled model feature that a stronger overall warming occurs in the northern Hemisphere than in the SH, which is expected to lead to a similar hemispheric imbalance in rainfall (Murphy and Mitchell, 1995). The hemispheric asymmetry in warming is due to the greater proportion of ocean in the SH, and much greater thermal inertia of the SH oceans causing a delayed warming relative to the northern Hemisphere (Stouffer et al., 1989, Cai et al., 2003a).

### **1.3.2.2 Scope**

Available observations and reanalysis data are used to examine the dynamics of observed rainfall variability over NWA and circulation patterns associated with the observed increasing rainfall trend. We then benchmark the performance of the climate model used in the Rotstayn et al. (2007) study. The focus will be on whether the model reproduces the observed variability and circulation trend associated with the increased rainfall (section 3). As will be shown, the modeled rainfall change over NWA in the Rotstayn et al. (2007) study might be a by-product of a well-known model deficiency associated with an equatorial Pacific cold tongue, common in most climate models. The cold tongue extends into the EIO, generating an unrealistic relationship between the EIO SST and Australian rainfall.

### **1.3.3 The future of Australian rainfall**

Within the Indo-Pacific system, the subtropical pathway, i.e., through the EAC, for transmission of Pacific signals has not been well studied. Observational evidence suggests the strength of the sub-tropical exchange has been changing with strong impacts on climate and marine ecosystem. The changing strength means that the properties of the Pacific Ocean circulation, such as the EAC, its separation location, and the inflow/outflow partition have been changing. Simultaneously, Southern Hemisphere atmospheric circulation has been marked by substantial trends. We will explore the dynamics of their possible linkage, and the combined impact, in particular, the likelihood of a feedback into the atmosphere as a consequence of the changing EAC that provides an influence on future Australian rainfall.

#### **1.3.3.1 Current knowledge**

Variations of the SH atmospheric circulation have been shown to be organized into a number of well-defined spatial patterns (Kidson, 1999). The most prominent of these low-frequency circulation patterns is characterized by a predominantly zonally-symmetric pattern, a see-saw meridional variation in the zonal wind strength between 40°S and 60°S, and an equivalent barotropic structure in the vertical (Kidson, 1988a; Shiotani, 1990; Hartmann and Lo, 1998; Thompson and Wallace, 2000; Rashid and Simmonds, 2004). It has variously been called the Antarctic Oscillation (Gong and Wang, 1999), and the SAM (Limpasuvan and Hartmann, 1999). It will be referred to as the SAM throughout this thesis.

The SAM is the leading mode of Southern Hemisphere circulation variability. Thompson and Wallace (2000) revealed the SAM as the leading EOF in many atmospheric fields, including MSLP, geopotential height, surface temperature, and zonal wind. The oscillations exist year-round in the troposphere, but it amplifies with height upward into the stratosphere during certain times of the year or “active seasons.” The SAM contributes to a significant proportion of SH climate variability from high-frequency (Baldwin, 2001) through to very low-frequency time scales (Kidson, 1999). Modeling studies indicate that the SAM is also likely to drive the large-scale variability of the Southern Ocean (Hall and Visbeck, 2002).

As shown in Fig. 1.2, SWWA has experienced a substantial drying trend with a winter rainfall decrease of some 20% (IOCI, 2002). The decline manifests itself as a reduction in high-intensity winter rainfall events, and is accompanied by an upward trend of the SAM (Thompson et al., 2000; Marshall, 2003; Marshall et al., 2004) with increasing MSLP in the midlatitudes. The cause of the upward trend of the SAM is a contentious issue. Observational (Thompson and Solomon, 2002) and other modelling studies (Sexton, 2001; Gillett and Thompson, 2003) indicate that it is attributable to ozone depletion over the past decades. Climate models produce increasing midlatitude MSLP under increasing atmospheric CO<sub>2</sub> incorporated in an upward trend of the SAM (Fyfe et al., 1999; Kushner et al., 2001; Cai et al., 2003a). In the mean time, model rainfall over

SWWA decreases in the transient period while CO<sub>2</sub> increases (Cai et al., 2003a). A recent study (Cai and Cowan, 2006) indicates that at least 50% of the observed SWWA

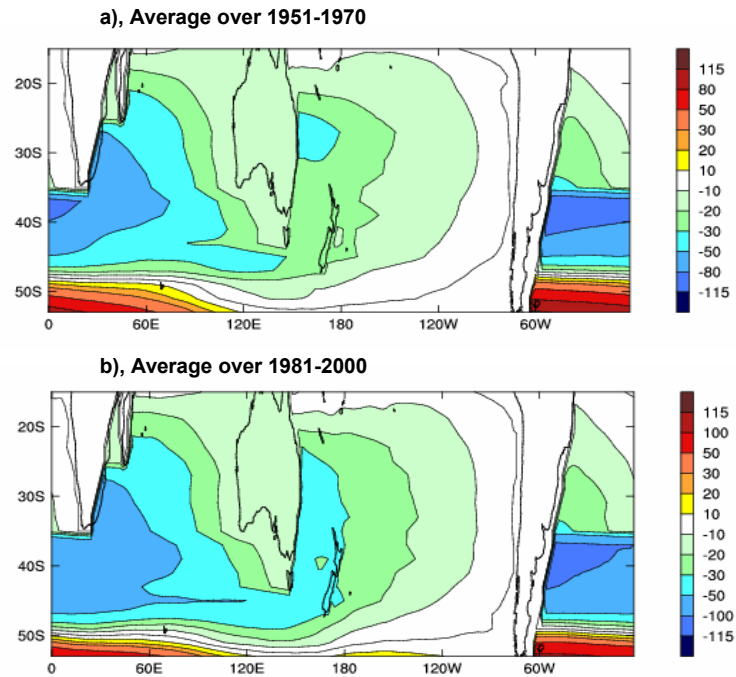


Figure 1.5: Wind-drive ocean circulation (in Sv,  $1 \text{ Sv} = 10^6 \text{ m}^3 \text{ s}^{-1}$ ) calculated using NCEP winds, a) over the period of 1948-1967, and b) over the period of 1981-2000. The comparison shows a stronger EAC flow passing the Tasman Sea, consistent with what is predicted by couple climate models.

rainfall reduction is driven by anthropogenic forcing. Although such a decrease in midlatitude rainfall is consistent with a reduction in extratropical SH cyclones, one would expect that a similar reduction in rainfall over the southeastern Australia, where however, the model rainfall reduction is less than that over SWWA. We hypothesize that changing ocean current as a result of wind changes associated the SAM is a potential process accounting for the different rainfall response between SWWA and southeast Australia. Specifically, an intensifying EAC will transport warmer water south, which promotes convection and rainfall, providing a mechanism offsetting the rainfall reduction associated with rising MSLP incorporated in the upward trend of the SAM.

There are little ocean observations available to examine the oceanic impacts of the atmosphere circulation trends, but it can be assessed partially through surface wind changes. We will use the trends in surface winds to estimate oceanic circulation change and assess the importance of ozone depletion in driving the change. Figure 1.5 shows the wind-driven barotropic ocean circulation (in Sv,  $1 \text{ Sv} = 10^6 \text{ m}^3 \text{ s}^{-1}$ ), determined with

Godfrey's Island Rule model (Godfrey, 1989) forced with NCEP reanalysis data (Kalnay et al., 1996). The results indicate that over the past decades the entire Indo-Pacific Southern Ocean circulation has changed significantly, with an intensifying southern mid-latitude ocean circulation including the EAC. All climate models consistently produce an upward trend of the SAM. We will examine its influence on ocean circulation change, and its impact on Australian rainfall.

### 1.3.3.2 Scope

Attention will focus on how the subtropical oceanic circulation pathway has been changing over the past 50 years, and identify the level of impact it exerts. The issue of how the Southern pathway may respond to anthropogenic forcing. There is virtually no ocean observation in the South Pacific which covers a meaningfully long period. However, there are sufficient atmospheric observations and reanalysis, from which aspects of the ocean circulation can be derived. The impact of the changing ocean circulation on Australia rainfall will be assessed, together with the impacts from the trends of other climate drivers. Coupled climate model simulations under climate change forcing will provide the needed data sources.

### 1.4 Summary

We will focus on the three key areas in which a contribution can be made to better understand the dynamics governing rainfall variability and changes in Australia. Significant progress in our knowledge is needed in order to enhance our projection capability of future rainfall and hence water resources. The key questions we pose are:

- Is there a varying relationship between variability in the Pacific Ocean (ENSO) and in the IO, and how it contributes to the observed rainfall variations and trends? This and the related issues are addressed in Chapter 3.
- What are the dynamics governing variability and trends of rainfall over NWA? Is it really caused by anthropogenic aerosol forcing? We explore these questions in Chapter 4.
- What is the future of Australian rainfall, taking into account of possible changes in climate drivers and in ocean-atmosphere circulation? Chapter 5 provides a consensus projection and an interpretation.

The project has so far contributed to many publications, some are listed below. These are:

1. **Shi, G.**, J. Ribbe, W. J. Cai, and T. Cowan (2008a), An interpretation of Australian summer and winter rainfall projection. *Geophysical Research Letters*, 35, L02702, doi:10.1029/2007GL032436.
2. **Shi, G.**, W. J. Cai, T. Cowan, J. Ribbe, L. Rotstayn (2), and M. Dix (2008b), Variability and trend of the northwest Western Australia Rainfall: observations and coupled climate modeling. *Journal of Climate*, 21, 2938–2959
3. **Shi, G.**, J. Ribbe, W. J. Cai, and T. Cowan (2007), Multidecadal variability in the transmission of ENSO signals to the Indian Ocean. *Geophysical Research Letters*, 34, L09706, doi:10.1029/2007GL029528.

4. Cai, W. J., T. Cowan, M. Dix, L. Rotstayn, J. Ribbe, **G. Shi**, and S. Wijffels (2007) Anthropogenic aerosol forcing and the structure of temperature trends in the southern Indian Ocean. *Geophysical Research Letters*, 34, L14611, doi:10.1029/2007GL030380.
5. Cai, W. J., Meyers, G. A., and **Shi, G.** (2005). Transmissions of ENSO signal to the Indian Ocean. *Geophysical Research Letters*, 32 (5): 5616, doi:10.1029/2004GL021736.
6. Cai, W. J., **Shi, G.**, Cowan, T. D., Bi, D., and Ribbe, J. (2005). The response of the Southern Annular Mode, the East Australian Current (EAC), and the southern mid-latitude ocean circulation to global warming. *Geophysical Research Letters*, 32 (23): L23706, doi:10.1029/2005GL024701.

## Chapter 2: Data and Methodologies

To elucidate a physical process, multiple data sets and a combined deployment of several analytical techniques are required. Detailed rationales for a specific combination of data and methods adopted will be provided in Chapters 3 to 5, as we address specific issues identified in Chapter 1. Here, we outline the details of the models, data and methodologies used. These have been applied by Shi et al. (2007), Shi et al. (2008a, 2008b).

### 2.1 Data

#### 2.1.1 Observations and reanalyses

The observed rainfall data are from the Australian BMRC and updated version of GISST datasets (Rayner et al., 1996). Although these two datasets cover a period from late 19<sup>th</sup> century to 2006, we focus on the 50 year period from 1951-2000. To understand the circulation associated with rainfall patterns, MSLP and surface winds data, and other fields from the NCEP reanalysis are used (Kalnay et al., 1996).

The ocean thermal analysis is the operational subsurface temperature reanalysis from the BMRC (Meyers et al., 1991; Smith, 1995a, 1995b), which is an optimal interpolation on a 1°C latitude by 2°C longitude grid at 14 depth levels, throughout the Indo-Pacific basin. It is based primarily on XBT profiles and time-series from the Tropical Atmosphere Ocean buoy array (McPhaden et al., 1998), and covers a 20-year period since 1980. The data in the Pacific Ocean domain has been used in numerous studies (Meinen and McPhaden, 2000; Cai et al., 2004; Kessler, 2002). The relationship of oceanic variability to the wind field is documented with data from the NCEP reanalysis (Kalnay et al., 1996).

We utilize the newly available reanalysis of the Simple Ocean Data Assimilation Parallel Ocean Programme (SODA-POP) version 1.4.2 (Carton and Giese, 2006). The new model product uses the European Center for Medium Range Forecasts ERA-40 atmospheric reanalysis winds. It has a spatial resolution of 0.5°C latitude by 0.5°C longitude grid, and covers a period from 1958 to 2001. Both the SODA-POP and BMRC reanalyses independently incorporated Expendable Bathythermograph profiles and time-series from the Tropical Atmosphere Ocean buoy array (McPhaden et al., 1998). We find that there are remarkable differences in the transmission between the pre- and post-1980 periods. Cai et al. (2005c) discussed the post-1980 transmission. Our analysis focuses on the pre-1980 period.

Throughout this project, seasonal anomalies are constructed for each season into December-January-February (DJF), March-April-May (MAM), June-July-August (JJA), and September-October-November (SON), referenced to the respective seasonal average.

### 2.1.2 Climate models and outputs

The CSIRO Mark 3.0 climate model has been significantly improved relative to the Mark 3a model (Gordon et al., 2002). It is run without the use of flux adjustments. The horizontal resolution of the atmospheric model is spectral T63 (approximately 1.875° latitude, 1.875° longitude) with 18 vertical levels (hybrid sigma-pressure vertical coordinate). The atmospheric model includes a comprehensive cloud microphysical parameterization (Rotstayn et al., 2000) and a convection parameterization based on that used in the Hadley Centre model (Gregory and Rowntree, 1990). This convection parameterization is linked to the cloud microphysics scheme via the detrainment of liquid and frozen water at the cloud top. Atmospheric moisture advection (vapor, liquid, and frozen) is carried out by the semi-Lagrangian method (McGregor, 1993). A simple treatment of the direct radiative effect of sulphate entails a perturbation of the surface Albedo (Mitchell et al., 1995). The land surface scheme (six layers of moisture and temperature) with a vegetation canopy (Kowalczyk et al., 1991, 1994) includes a three-layer snow model. Multiple soil types and vegetation types are included.

The Mk3.0 ocean module is based upon the Modular Ocean Model (MOM2.2) version of the Geophysical Fluid Dynamics Laboratory model. The oceanic component has a horizontal resolution matching that of the atmospheric model's grid in the east–west direction and twice that in the north–south direction. Thus the grid spacing is approximately 0.9375° latitude × 1.875° longitude. Because there are two ocean grid points per atmospheric grid point in the meridional direction, the atmosphere model and ocean model subcomponents have identical land–sea masks. There are 31 vertical levels and the level spacing gradually increases from 10 m at the surface to 400 m in the deep ocean. A parameterization of mixing of tracers based on the formation of Griffies et al. (1998) and Griffies (1998) is included.

In this thesis, the analysis of outputs from a control simulation and four climate change experiments is discussed. The control simulation will be used to examine the relationship of Australian rainfall with the three engines of the Australia climate and with the Tasman Sea Surface Temperature (SST). For this purpose anomalies are obtained and referenced to a 300 year climatology. Previous studies have described the simulation of the ENSO and the IOD in this version of the model (Cai et al., 2003b; Cai et al., 2005a). Four climate change experiments follow the Intergovernmental Panel on Climate Change (IPCC) A2 (two experiments), A1B, and B1 scenarios that all incorporate CO<sub>2</sub> forcing, the direct effect of sulfate aerosols (direct effect only), and stratospheric ozone depletion. Each of the four experiments starts from a different time of the control experiment and together they provide an ensemble strategy. These data are used to study the impact of the Tasman Sea warming on Australia rainfall and the future Australia rainfall changes (see Chapter 5).

The CSIRO Mk3a climate model is developed while Mk3.0 is performing a multi-century control experiment and long-term climate change runs. It includes a comprehensive interactive aerosol scheme. In this version, the atmospheric and the ocean models both have a low-resolution (spectral R21) and the atmosphere has 18 hybrid vertical levels,

while the ocean has 21 vertical levels. A detailed description is provided by Rotstayn et al. (2007). The low-resolution allows fast integration of experiments with the comprehensive aerosol scheme, all covering the period 1871 to 2000. The aerosol species treated interactively are sulfate, particulate organic matter (POM), black carbon (BC), mineral dust and sea salt. As well as the direct effects of these aerosols on shortwave radiation, the indirect effects of sulfate, POM and sea salt on liquid-water clouds are included in the model. Historical emission inventories are used for sulfur. POM and BC derived from the burning of fossil fuels and biomass. Other forcings included are those due to changes in long-lived greenhouse gases, ozone, volcanic aerosol and solar variations (but changes in land cover are omitted). The ensemble consists of eight runs with all of these forcings (ALL ensemble). A further eight runs with all forcings, except those related to anthropogenic aerosols (AXA ensemble), differ only from the ALL ensemble in that the anthropogenic emissions of sulfur, POM and BC were fixed at their 1870 levels.

The analysis of these experiments is presented in Chapter 4 and focuses upon the causes of the NWA rainfall trends. Outputs from a multicentury (300 years) control experiment without climate change forcing are also used to examine if the model reproduces the rainfall teleconnection with large scale circulation fields. Outputs from the ALL ensemble are projected onto modes of variability in the control experiment.

The CSIRO Mk3.5 climate model has the same resolution as that of Mk3.0, but is improved in many aspects. During the course of my Ph. candidature, the improved model is run without climate change forcing, i.e., in the control climate setting. One of the most important improvements is that it overcomes a problem associated with the timing of signal transmission from the Pacific to the IO. We use the output to examine the robustness of multidecadal variability in the transmission. We use the results of a multi-century control experiment with this model. The new version simulates a more realistic transmission process, although it still suffers from the common cold tongue bias, i.e., the equatorial Pacific cold tongue extends too far west. The ENSO frequency is reasonably simulated as reported earlier (Cai et al., 2003b) but the amplitude is too large. Despite these deficiencies the model produces multidecadal variations in the transmission similar to the observed (see Chapter 3).

## **2.2 Methodologies**

Besides the commonly used correlation and regression analyse, we also apply EOF analysis, complex EOF (CEOF), and projections onto modes of variability. These and others are described below. We also point out Chapters where these methodologies are used.

### **2.2.1 EOF (Empirical Orthogonal Function)**

An EOF analysis is a mathematical method for analysing the spatial and temporal variability of geophysical data with long time series (Peixoto and Oort, 1992). It

identifies patterns of variability, and if variance of an identified pattern is large enough, there is often an identifiable physical mechanism that operates to generate the pattern.

A main feature of an EOF analysis is that it identifies correlations inherent in the data by re-organizing the original data into individual clusters in space or time. This can effectively compress a large number of spatially and temporally correlated values into both space and time components, while also splitting the temporal variance of the data series into a set of orthogonal spatial modes (also called eigenvectors) that explain a large proportion of the measured variance (Peixoto and Oort, 1992). This type of analysis has been used in climatological work for many years (e.g. in particular Lorenz since 1956) and its usage has steadily increased. It is a convenient method for analysing climatological fields (e.g., North *et al.*, 1982).

Consider the value of a field at  $N$  spatial locations which have  $M$  monthly observations ( $t$ ). Thus, the field at any one time form a spatial map of, for example, SSTs. Each map in the time series can be written mathematically as a vector of length  $N$ , producing,

$$z_m = (z_{m1}, z_{m2}, \dots, z_{mN})$$

where  $m$  represents the time instant in the series of observations, e.g.,  $m = 1, 2, \dots, M$ . As a result, a  $M \times N$  matrix containing the full time series of spatial elements is easily formed,

$$Z = \begin{bmatrix} z_{11} & z_{12} & \dots & z_{1N} \\ z_{21} & z_{22} & \dots & z_{2N} \\ \vdots & \vdots & \vdots & \vdots \\ z_{M1} & z_{M2} & \dots & z_{MN} \end{bmatrix}$$

The  $M$  rows represent the spatial maps at each time step and the  $N$  columns are the time histories at individual spatial locations. Therefore, an individual element of the matrix  $Z$  represents the SST at time  $m$  and spatial location  $n$ . To carry out the EOF analysis (i.e., find the orthogonal spatial modes), we need to maximize the expression,

$$\frac{1}{M-1} \sum_{m=1}^M (z_m \cdot v_n)^2 \quad (E1)$$

for each individual spatial location (i.e.,  $n = 1, 2, \dots, N$ ) subject to the conditions,

$$v_n \cdot v_i = v_n^T v_i = \begin{cases} 1 & \text{if } n = i \\ 0 & \text{if } n \neq i \end{cases} \quad (E2)$$

where  $v_n$  is the orthonormal vector that optimally represents the original data vector,  $z_m$ . In matrix form, expression E1 can be written as,

$$\frac{1}{M-1} \sum (z_m \cdot v_n)^2 = \frac{1}{M-1} (v_n^T Z Z^T v_n) = v_n^T C v_n$$

where  $C$  would normally symbolize the *covariance* matrix (Peixoto and Oort, 1992). However, if one is comparing different model output fields, the *correlation* matrix ( $C$ ) should be used as it will provide equal weighting of the different variables analysed and a sensible comparison of results between the model fields (von Storch and Zwiers, 1999).

The correlation matrix of the SST anomalies is defined by:

$$C = \frac{Cov}{\sqrt{Var(Z^T)Var(Z)}}$$

This is an  $M \times M$  real symmetric matrix where

$$Cov = \frac{1}{M-1} Z^T Z$$

The maximization of  $[v_n^T C v_n]$ , subject to the condition (E2), establishes a variational problem which leads to eigenvalue problems or characteristic value problems. However the problem can be solved by,

$$C v_n = \lambda_n v_n$$

where  $\lambda_n$  is the eigenvalue associated with the characteristic eigenvector ( $v_n$ ) of the correlation matrix,  $C$ . Each of the associated eigenvalues ( $\lambda_n$ ) identifies the fraction of the total data variance explained by the eigenvector, which is given by,

$$\frac{\lambda_n}{\sum_{i=1}^N \lambda_i}$$

The eigenvalues are ordered to decrease with successive modes such that the first eigenvector and its associated eigenvalue explain the largest portion of the total variance, while the second eigenvector and its associated eigenvalue explain the second largest portion of the total variance and so forth (von Storch and Zwiers, 1999). The total number of spatial modes generated in an EOF analysis is equal to the smallest dimension of the original data matrix.

The spatial pattern of each of the eigenvector's (modes) weighting coefficients can be constructed by projecting  $z_m$  onto  $v_n$  ( $n = 1, 2, \dots, N$ ) using,

$$w_{mn} = v_n z_m$$

These weighting coefficients represent how well the mode  $v_n$  describes the observation  $z_n$  (Peixoto and Oort, 1992). Thus, theoretically any observation of SST ( $z_n$ ) can be expressed as the linear combination of the eigenvectors  $v_n$ ,

$$z_m = \sum_{n=1}^N w_{mn} v_n$$

This can be written in matrix notation as,

$$W = ZV$$

The elements of the columns of  $W$  [ $w_{1n}$ ,  $w_{2n}$ , ...,  $w_{Mn}$ ] are the dimensional time coefficients associated with the eigenvector  $v_n$ . Thus, it is the eigenvector's corresponding time series that displays the temporal behaviour of the mode. These time components are commonly referred to as expansion coefficients. It is also important to note that these column vectors [ $w_{1n}$ ,  $w_{2n}$ , ...,  $w_{Mn}$ ] are mutually orthogonal (Peixoto and Oort, 1992).

Although this method of analysis is purely mathematical, the larger the variance explained by the dominant modes of a system, the more likely they are to be physically meaningful (Peixoto and Oort, 1992). The number of important spatial modes identified by an EOF analysis is determined based on the eigenvector spectrum and, for example, the mode degeneracy (e.g., North et al., 1982). In most cases, the majority of the data variance can normally be explained by only the first few EOFs (von Storch and Zwiers, 1999).

### 2.2.2 CEOFs and Statistical Significance of Monthly and Filtered Time Series

An EOF analysis allows identification of a stationary pattern. In Chapter 3 we will be discussing the propagation of the Indo-Pacific signals into the IO, and we used filtered data. This propagation can be described by lag correlation and regression, or by complex EOF (CEO). All these methods are used. Here, we use a routine described by Barnett (1983). Time sequence data at each spatial location is Hilbert-transformed to obtain a complex time sequence, the real part being the input data and the imaginary part representing signals that are identified to be related with the real part but are 90° out of phase. The complex eigenvectors and complex principal components are then found by singular value decomposition of the matrix. These procedures are well developed, below we discuss the statistical significance based on monthly and filtered time series.

The conventional theory of statistical significance and estimation is highly developed and extensive. However, its application to specific data sets depends on the following assumptions. (1) The data are jointly statistically stationary over the length of the record.

(2) The variables being considered are all jointly normally distributed, being part of respective populations that have underlying means, variances, and covariances. (3) The data sets used are unbiased samples of these populations.

In an analysis of climate data, there may be problems with each of these assumptions. Long-period variations such as the Interdecadal Pacific Oscillation may affect data sets of length  $< 20$  years or so, and the normality of variables on these timescales is uncertain. The representativeness of samples is perhaps the least questionable of these assumptions, but this is also sensitive to processes on timescales longer than the length of the record. Given these uncertainties, a statistical analysis of uncertainties of climate data sets is probably only useful as a guide, and though it provides answers, these should not be expected to constitute firm conclusions about significance. Nevertheless, we pursue it here.

The relationship between the time series of any two observed variables  $x(t)$  and  $y(t)$  (such as the SST at two particular grid points) is measured by covariance between them and, as computed from the data, is denoted  $v_{xy}$ . However, this computed covariance is just an estimate from the sample of data available of the underlying covariance  $\mu_{xy}$  of the assumed population of SSTs at these two grid points. It is this latter quantity that we are trying determine. How good is the estimate? A measure of this is given by the variance  $s_{xy}^2$  (or standard error  $s_{xy}$ ) of  $v_{xy}$  defined by

$$s_{xy}^2 = E(v_{xy} - \mu_{xy})^2 = E(v_{xy})^2 - \mu_{xy}^2, \quad (\text{A1})$$

where  $E$  denotes the expected value, and  $\mu_{xy} = E(v_{xy})$ . We do not know  $\mu_{xy}$  but must estimate it  $v_{xy}$ , so that

$$s_{xy}^2 = E(v_{xy})^2 - v_{xy}^2 \quad (\text{A2})$$

If  $x$  and  $y$  are complex time series,

$$v_{xy} = cov(x,y) = \frac{1}{N} \sum_{i=1}^N [x(t_i) - \bar{x}][y(t_i) - \bar{y}],$$

$$\bar{x} = \frac{1}{N} \sum_{i=1}^N x(t_i) \quad (\text{A3})$$

$$s_{xy}^2 = \frac{1}{N^2} E \left\{ \sum_{i=1}^N \sum_{j=1}^N [x(t_i) - \bar{x}][y(t_i) - \bar{y}]^* \times [x(t_j) - \bar{x}][y(t_j) - \bar{y}]^* \right\} - E[(v_{xy})]^2 \quad (\text{A4})$$

where an asterisk denotes a complex conjugate. covariances such as  $v_{xy}$  may be complex, but variances and  $s_{xy}^2$  are real. We assume that  $x$  and  $y$  are jointly normally distributed,

with means  $\mu_x$  and  $\mu_y$ , variances  $\sigma_x^2$  and  $\sigma_y^2$ , and (complex) correlation coefficient  $r_{xy}$ . Then (A4) reduces to (Papoulis, 1965; Davis, 1976)

$$S_{xy}^2 = \frac{\sigma_x^2 \sigma_y^2}{N} \left\{ 1 + |r_{xy}|^2 + \sum_{j=1}^{N-1} [\text{Re}(r_{xx}(j)r_{yy}(j)) + |r_{xy}(j)|^2] \right\} \quad (\text{A5})$$

where  $N$  is assumed to odd for convenience,  $\text{Re}$  denotes real part, and  $r_{xx}(j)$  denotes the time-lagged correlation coefficient for  $x$  with lag  $j\Delta t$ , where  $\Delta t$  is the time interval between samples. Quantities on the right-hand side of (A5) must be estimated from their sample values, taking  $\sigma_x^2 = v_{xx}$ ,  $\sigma_y^2 = v_{yy}$ ,  $r_{xy} = v_{xy}/(v_{xx} v_{yy})^{1/2}$ , etc. If  $\Delta t$  was significantly large, so that the values of  $x(t_i)$ ,  $y(t_i)$  were all independent from each other, the lag correlation terms would all vanish. We would have  $N$  independent sample pairs, or “degrees of freedom,” so that in this case,

$$S_{xy}^2 = \frac{\sigma_x^2 \sigma_y^2}{N} [1 + |r_{xy}|^2] J. \quad (\text{A6})$$

Equation (A5) may then be used to define an effective number of degrees of freedom  $N^*$  in (A6) (Davis, 1976)

$$N^* = \frac{N(1 + |r_{xy}|^2)}{\{1 + |r_{xy}|^2 + 2 \sum_{j=1}^{N-1} [\text{Re}(r_{xx}(j)r_{yy}(j)) + |r_{xy}(j)|^2]\}} \quad (\text{A7})$$

Taking  $v_{xy} + / -s_{xy}$  gives an estimate of  $\mu_{xy}$ , with error bars the width of the standard error.

To test the significance of CEOFs, we follow the procedure described by North et al. (1982) and consider an array of  $m$  grid points at each of which there is an observed series of values of a variable  $x$  at  $N$  times. These times are simultaneous and evenly spaced with interval  $\Delta t$ . Hence we have an array of data  $x_j(t_k)$ ,  $j = 1, \dots, m$  and  $k=1, \dots, N$ . From these we may obtain CEOF by taking the Hilbert transform  $h_j(t_k)$  of the time series at each grid point and then defining the complex time series

$$X_j(t_k) = x_j(t_k) + ih_j(t_k). \quad (\text{A8})$$

We then define the  $m \times m$  matrix of complex covariances  $S_{ij} = \text{cov}(X_i, X_j)$  by (A3). The spatial structure of the CEOFs is then given by the eigenvalue equation

$$\sum_{j=1}^m S_{ij} f_\alpha(j) = l_\alpha f_\alpha(i), \quad \alpha, i = 1, \dots, m, \quad (\text{A9})$$

where  $S_{ij}$  is Hermitian, so that the eigenvalues  $l_\alpha$  are all real and positive and the eigenvectors  $f_\alpha$  are complex. These form a linearly independent set, with  $\alpha = 1, \dots, m$ .

In accordance with the assumptions mentioned above the background population of which the  $x_i$  represent a sample are assumed to be statistically and have underlying values of the covariances at the  $m$  grid locations that may be represented by  $v_{ij}$ . From these exact (but unknown) covariances the exact eigenvalues  $\lambda_\alpha$  and eigenvectors  $\phi_\alpha(i)$  are given by

$$\sum_{j=1}^m v_{ij} f_\alpha(j) = \lambda_\alpha \phi_\alpha(i), \quad \alpha, i = 1, \dots, m. \quad (\text{A10})$$

One may expect that the deviations of the sample covariances  $S_{ij}$  from the actual covariances  $v_{ij}$  will be of the order of the standard errors of the  $S_{ij}$ , so that we may write

$$S_{ij} = v_{ij} + \varepsilon V_{ij}, \quad (\text{A11})$$

where  $\varepsilon$  is a small parameter of order  $(2/N^*)^{1/2}$  and  $V_{ij}$  is of the order of

$$V_{ij} = [(v_{ii} v_{jj} + v_{ij}^* v_{ij})/2]^{1/2} \quad (\text{A12})$$

where  $N^*$  is given by (A7) with  $X_i$  and  $X_j$  in the place of  $x$  and  $y$ . In practice, we take a mean value for  $N^*$  over all pairs  $X_i, X_j$ . for values of the  $v_{ij}$  we use the sample values  $S_{ij}$ . One may then use a standard perturbation expansion of the form

$$f_\alpha = \phi_\alpha(i) + \varepsilon f_\alpha^{(\perp)} + \dots, \quad (\text{A13})$$

$$l_\alpha = \lambda_\alpha + \varepsilon l_\alpha^{(\perp)} + \dots, \quad (\text{A14})$$

to obtain the first-order deviations due to the perturbations in the  $v_{ij}$ . These give (North *et al.*, 1982)

$$l_\alpha^{(\perp)} = \sum_{i=1}^m \sum_{j=1}^m \phi_\alpha^*(i) V_{ij} \phi_\alpha(j), \quad (\text{A15a})$$

$$\lambda_\alpha^{(\perp)} = \sum_{i=1}^m \sum_{j=1}^m \phi_\alpha^*(i) v_{ij} \phi_\alpha(j), \quad (\text{A15b})$$

$$f_\alpha = \sum_{\beta=1}^m a_{\alpha\beta} \phi_\beta(i), \quad \beta \neq \alpha, \quad (\text{A16a})$$

$$a_{\alpha\beta} = \frac{\sum_{i=1}^m \sum_{j=1}^m \phi_{\beta}^*(i) V_{ij} \phi_{\alpha}(j)}{\lambda_{\alpha} - \lambda_{\beta}}. \quad (\text{A16b})$$

Since  $V_{ij}$  is of the same order as  $v_{ij}$  ( $V_{ii} \approx v_{ii}$ ), from (A15) we have  $l_{\alpha}^{(1)} = O(\lambda_{\alpha})$ , so that the magnitude of the uncertainty in the eigenvalue  $\delta \lambda_{\alpha}$  is approximately

$$\delta \lambda_{\alpha} = \varepsilon \lambda_{\alpha}^{(\pm)} \approx \left[ \frac{2}{N^*} \right]^{1/2} \lambda_{\alpha}. \quad (\text{A17})$$

If one eigenvalue is much larger than the others, the form of (A15) indicates that (A17) may be an overestimate. In these cases, sample computed values for  $l_{\alpha}^{(\pm)}$  using (A15) generally give much smaller values than those from (A17). Clearly, this criterion should be taken as a guide and these uncertainties are interpreted as error bars in our analysis.

### 2.2.3 Projections of spatially and temporally varying data onto a pattern

It is increasingly recognized that anthropogenic climate change can project onto existing natural variability modes of the climate system (Clarke et al., 2001). To examine how climate change signals may project onto existing modes of variability, a pattern regression onto a pattern of a known mode is carried out. The patterns of variability modes are identified using common statistical analysis technique such as EOF, regression onto climate indices, for example, a Niño3.4 (170°W-120°W, 5°S-5°N, an index of ENSO).

A linear projection method is then used to investigate the evolution of a given circulation pattern  $G(x,y)$  and the extent to which climate change signals project onto the given pattern. For a circulation field  $A(x,y,t)$ , this is carried out in the following way: for each given instant  $t_n$ , we regress  $A(x,y, t_n)$  onto  $G(x,y)$  to yield a pattern regression coefficient. When this is done for all  $t$ , a time series  $f(t)$  of the pattern regression coefficient is generated. The time series  $f(t)$  is employed to estimate the trend  $\nabla f(t)$  of the pattern, and the trend associated with the pattern is given by  $\nabla f(t) \times G(x,y)$ .

This technique is used extensively in Chapter 4. It involves an identification of modes of variability using linearly detrended data; thereafter, raw data are then projected onto these modes of variability to assess whether the observed rainfall increase over NWA can be understood in terms of a projection onto the existing variability modes.

### 2.2.4 Godfrey's Island Rule models

There is little long-term ocean observation to determine if and to what extent the ocean circulation has changed. To this end, we have to rely on wind data. Some 40 years after Sverdrup (1947) developed his fundamental wind-driven circulation theory, Australian

scientist Dr. Stuart Godfrey, advanced it in an elegant and provoking way (Godfrey, 1989). He proposed an “Island Rule” and used it in conjunction with the Sverdrup relationship such that given a set of surface wind-stress field, global wind-driven circulation can be determined. This Island Rule model is used to monthly surface wind stress fields from National Centre for Environmental Prediction (Kalnay et al., 1996) reanalysis and ERA40 (Uppala, et al., 2005) reanalysis to generate the wind-driven circulation history in terms of barotropic stream function and steric height. The Island Rule model is also applied to model-generated winds in climate change experiments to determine how much of the ocean circulation change is due to changes in wind and how much is due to changes in buoyancy forcing (see Chapter 5). In the following section, the model is described briefly.

For the interior ocean, the stream function  $\psi$  is determined by the Sverdrup relationship:

$$-\beta \frac{\partial \psi}{\partial x} = \text{curl}_z \tau_s, \quad (\text{G1})$$

Where  $\beta = \frac{\partial f}{\partial y}$  describes the derivative of  $f$  with respect to  $y$ ,  $f$  is the Coriolis coefficient, and  $\tau_s$  is the surface wind stress. The flow along the western boundary, where the Sverdrup relationship breaks down, is calculated using the “Island Rule” for flows around an island, such as Australasia, New Zealand, and Madagascar (see upper panel, Fig. 2.1). The total flow  $T_o$  is determined by the pressure head between each island’s northern and southern extremities and is the integral of wind along the red loop (Fig. 2.1):

$$T_o = \oint_{QRST} \tau^{(l)} dl / \rho_0 (f_Q - f_T). \quad (\text{G2})$$

Here,  $f_Q$  and  $f_T$  are the Coriolis coefficient at  $Q$  and  $T$  latitude,  $\rho_0$  is the mean water density. Both the streamfunction and the steric heights have been calculated for NCEP and ERA40 wind products, with the Indonesian Throughflow Passage open in a quasi-realistic topographic setting. The data provides monthly, annual mean and seasonal outputs of both variables in NetCDF format. This data is now available from the Tasmania Partnership of Advanced Computing (<http://www.tpac.org.au>). The Indonesian Throughflow, which is the path integral of the wind stress around the red loop QRST (upper panel, Fig. 2.1, based on that calculated using NCEP winds), shows a realistic seasonal cycle, strongest in southern winter and weaker in southern summer (lower panel, Fig. 2.1).

One primary application of this model and the outputs is to calculate ocean climate trends. An assumption of the Island Rule is that the wind forcing has acted on the ocean for a timescale longer than that of the oceanic adjustment, i.e., Rossby wave process, long enough such that the ocean can be assumed to be at a steady state. In other words, the timescale for Rossby wave to traverse from the eastern boundary to the western boundary, which is longer as latitude increases, must be shorter than the time duration

within which a trend is to be determined. These time scales have been calculated by previous studies for the South Pacific (e.g., Qiu and Chen, 2006, see Fig. 2.2). For example, at 45°S, it would take 22 years to complete the full Rossby wave adjustment process from the South Pacific's eastern boundary to its western boundary.

To determine the wind-driven South Pacific circulation trend at this latitude from 1978-2003 (e.g., Cai, 2006), which is 25 years, the Island Rule can be applied. At any latitudes north of 45°S, e.g., in the tropics, where the Rossby wave adjustment time scale is much shorter, the Island Rule is applicable. For the same time duration (1978-2003) discussed above, one can use the Island Rule to calculate maps of the wind-driven circulation trends. This is discussed in Chapter 5.

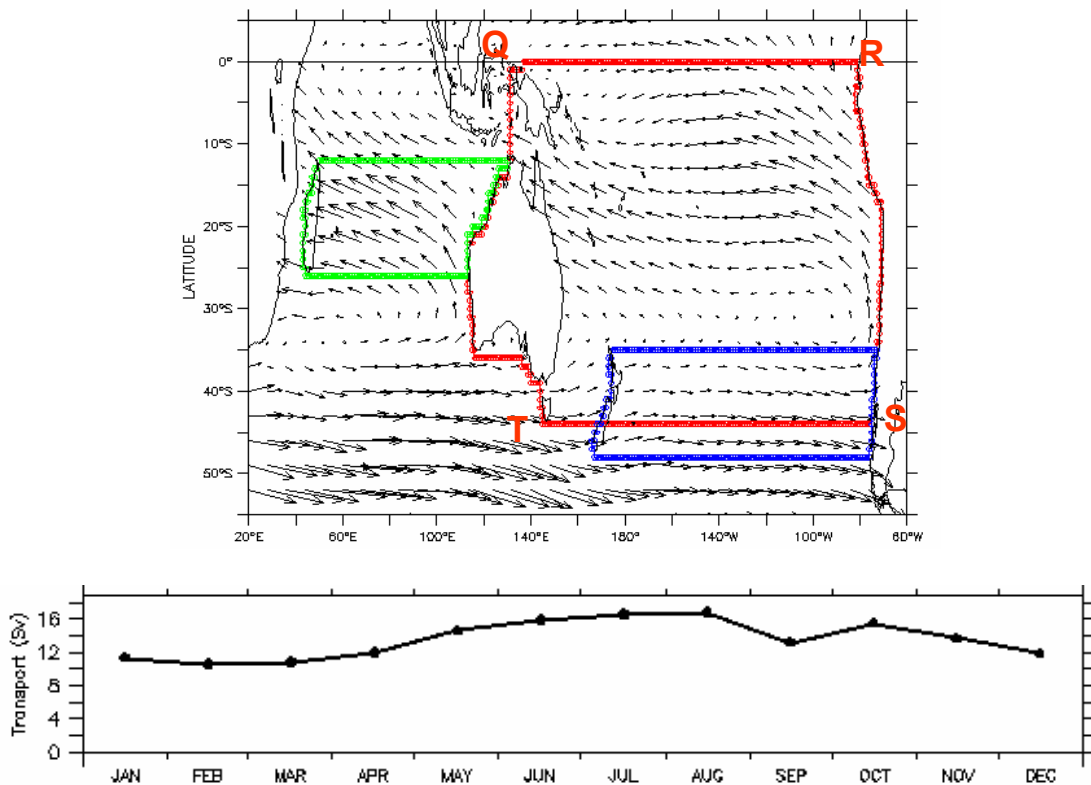


Figure 2.1: Upper panel, illustration of the Island Rule in the Indo-Pacific system, superimposing on annual mean winds. Three islands are included. For island such as Australasia, the circulation around the island can be obtained from the path integral of the wind stress around a path like the red loop QRST. Lower panel, transport in (absolute value) using NCEP monthly mean winds for Australasia, which is the modelled Indonesian Throughflow.

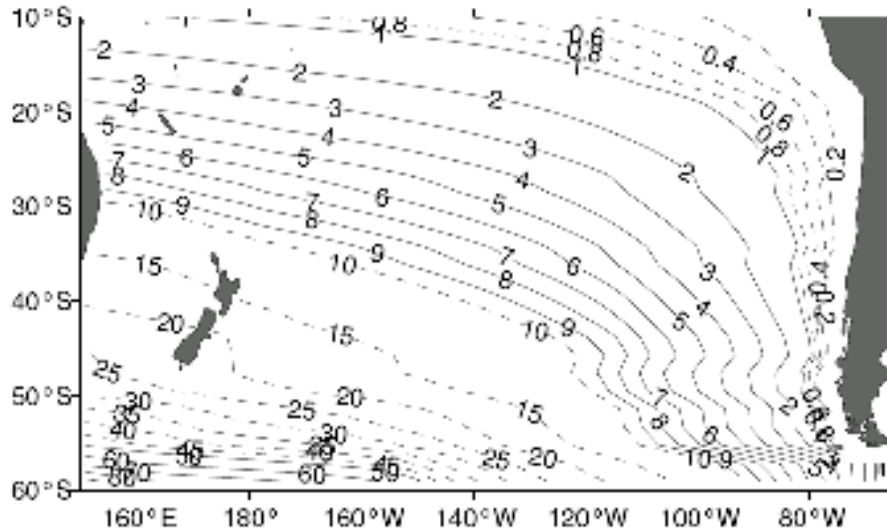
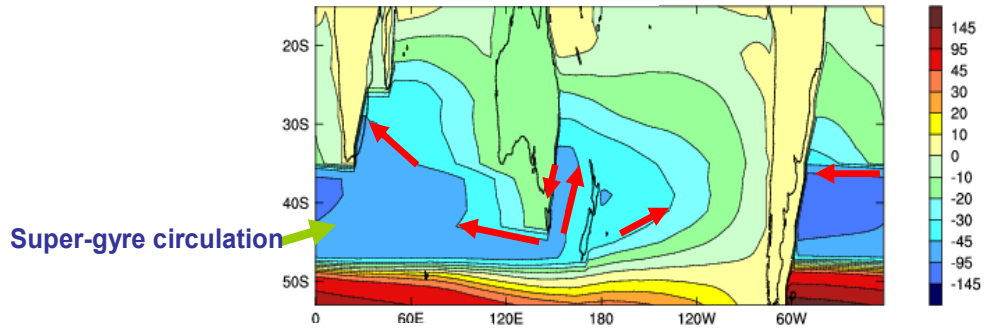


Figure 2.2: Time [years] required for the long baroclinic Rossby waves to traverse the South Pacific Ocean from the eastern boundary to the west (from Qiu and Chen, 2006). Notice that the contour intervals are not uniform.

The model is tested through several applications. Due to lack of observations in the SH oceans, we have very little understanding of the seasonality of the ocean circulation. The Island Rule model can be used to reveal the seasonality of the wind-driven component. Figure 2.3 displays such circulation for two seasons, the southern summer (upper panel) and the southern winter (lower panel). It shows a strong influence of the mid-latitude westerly jet on the ocean. In summer, the subtropical ridge is at latitudes furthest to the south. As a result, the associated wind stress curl, which determines the ocean circulation, moves furthest to the south, and the zero-curl line, which defines the southern-most boundary of the subtropical gyres, stretches across the three oceans, intersecting the South American coast (see Fig. 2 of Cai, 2006). This generates the so-called super-gyre circulation, linking the subtropical circulation of the South Pacific, South Indian, and South Atlantic. The flow of the EAC through the Tasman Sea (Tasman leakage) veers into the IO and to the South Atlantic. The super-gyre circulation is thought to be involved in the global thermohaline circulation, with the Tasman leakage contributing 3.2 Sv of the total 20 Sv of the North Atlantic Deep Water formation (Speich et al., 2007). In winter, as the wind system moves northwards, the gyre circulation in the South Pacific is isolated from the Indian and Atlantic circulation. The EAC separates from the coast at about 32°S. These wind-driven features are consistent with what is revealed by limited observations.

**Wind-driven Eastern Australian Current  
Dec. Jan. Feb. average**



**June July August average**

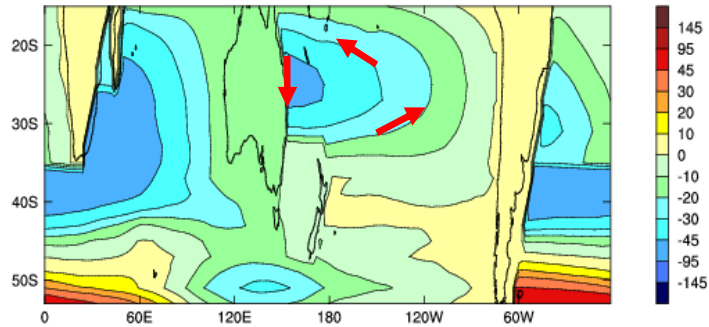


*Figure 2.3: Wind-driven climatological circulation for southern summer (upper panel) and southern winter (lower panel) based on NCEP winds. Unit in Sv ( $1 \text{ Sv} = 10^6 \text{ m}^3 \text{ s}^{-1}$ ).*

Another example is the decadal difference in the Pacific discharge/recharge via Sverdrup transport. The Pacific Ocean climate experienced a shift towards a warm state in the late 1970s, with marked changes in the ENSO properties and in many other circulation fields. During the post-1980 period, El Niño events are stronger than La Niña events contributing to significant difference in the mean circulation between the pre- and post-1980 periods. In the post-1980 periods, the equal Pacific circulation features weaker equatorial easterlies, stronger positive curls from the equator to  $5^\circ\text{N}$  and negative curl in the  $5^\circ\text{S} - 15^\circ\text{S}$  (Fig. 2.4a). The curls, through Sverdrup balance promotes a greater discharge of heat from the equatorial region and hence a shallower equatorial Pacific thermocline in the post-1980 period (Fig. 2.4b) (Jin, 1997a; 1997b; Meinen and McPhaden, 2000), consistent with an El Niño-like multidecadal-long condition for the post-1980 period. On interannual time scales, the discharge signal is transmitted into the WA coast and radiates into the IO, leading to a shallower mean thermocline off the WA coast and throughout the southern tropical IO (Fig. 2.4b).

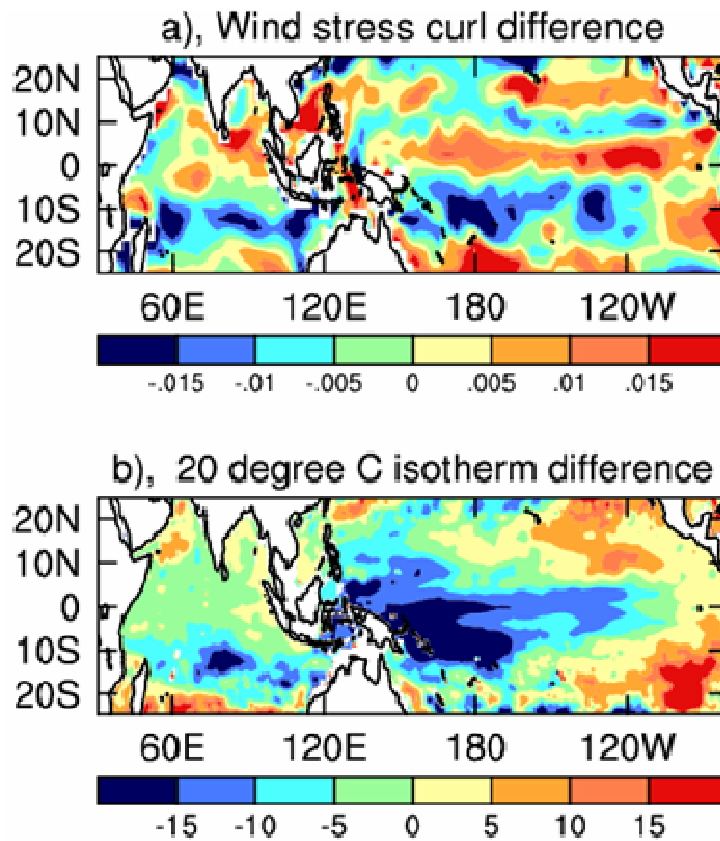
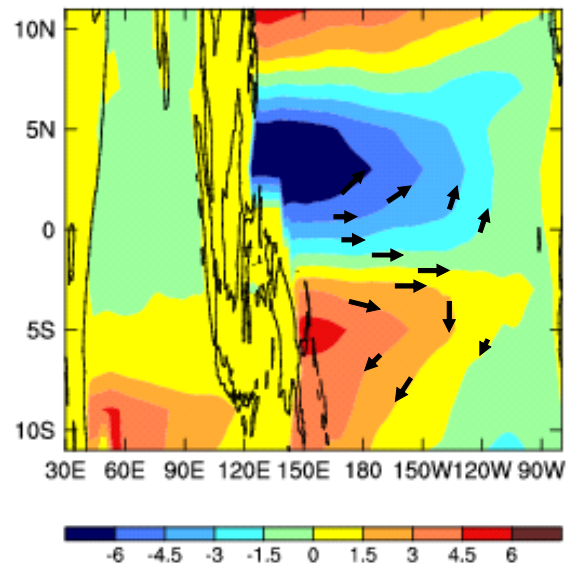


Figure 2.4: Difference in 20-year averaged a) wind stress curl ( $N m^{-3}$ ) based on ERA40 winds, and b) thermocline depth (m) between the pre- and post-1980 period (post-1980 minus pre-1980) based on the Simple Ocean Data Assimilation (SODA) (Carton and Giese, 2007).

Using the Island Rule calculation, we examine ways in which the discharge process operates. In the tropics, where Rossby wave time scale is short, the model is particularly applicable. The difference in the wind driven circulation (Fig. 2.5) features broad interior poleward flows. These are important pathways for discharging heat from the equatorial Pacific. Another way is the equatorward flows along the boundaries, replacing the discharged warm equatorial warm water with the off-equatorial colder water. These processes also operate in the southern tropical IO, and are supported by negative wind stress curl (Fig. 2.4a).



*Figure 2.5: Decadal difference in wind-driven circulation (1981-2000 average minus the 1960-1980 average). Unit in Sv. The post-1980 period features stronger ENSO, with greater discharge of heat from the equatorial Pacific to the tropical latitudes.*

In order to address issues in each Chapter, various methodologies and data will be used in combination. For example, in Chapter 4, EOF analysis, correlation and time series regression will all be used. A brief description of detail will be provided.

# Chapter 3: Indo-Pacific Teleconnection

In this Chapter, we address the process of the Indo-Pacific oceanic teleconnection through the Indonesian Throughflow passage. We then discuss the robustness of the teleconnection in terms of differences between the pre-1980 and post-1980 period. As already alluded in the Chapter 1, the motivation is to unravel the dynamics of rainfall variability over Australia, because previous studies have demonstrated a linkage between variability of EIO SSTs and South East Australia (SEA) rainfall, and a strong influence of Pacific variability and occurrence of the IOD since 1980.

The main findings reported in this Chapter are:

- The transmission of the Pacific ENSO signals to the IO involves an off-equatorial Pacific pathway;
- The transmission of El Niño discharge signals from the Pacific to the IO is far stronger during the post-1980 period, therefore contributing to the shallowing of the EIO thermocline and to the higher occurrence of stronger IOD events;
- This multidecadal difference is essential for explaining the structure of the temperature trends in the IO.

This chapter covers contents of published papers arising from, and contributed to by this Ph. D project. The candidate initiates the original idea of, and leads the analysis of one paper (Shi et al., 2007), and contributes to the other two papers (Cai et al., 2007; Cai et al., 2005c).

## 3.1 Background

### 3.1.1 Teleconnection between EIO SST and SEA rainfall

While rainfall in north-eastern Australia (e.g. Queensland) is mainly affected by SST anomalies of the equatorial eastern Pacific Ocean region, there is no doubt that variability of the EIO SST has a great impact on the rainfall over Australia's southeastern states (Smith, 1993; Smith et al, 2000; Ansell, 2000; Ashock et al., 2004; Cai et al., 2005c). This is illustrated in Figure 1.3, which compares the relationship of rainfall over the important region of MDB with EIO SST anomalies and with ENSO (Niño 3.4 index) for JJA. The figure suggests that the relationship between MDB rainfall and EIO SST anomalies is stronger than that between MDB rainfall and ENSO, although opposite in sign.

It is proposed that through atmospheric teleconnection, i.e., El Niño-induced easterlies which raise the EIO thermocline, the stronger and more protracted El Niño since 1980s make IOD events stronger as proposed by Annamalai et al. (2005). The analysis presented in the following sections investigate if an oceanic teleconnection plays a similar role.

### **3.1.2 The Indo-Pacific teleconnection**

SST variability in the EIO is not independent from that in the Pacific and it is therefore necessary to study the linkage between them. The Indo-Pacific linkage in terms of a tropical oceanic teleconnection occurs via the Indonesian Throughflow (Meyers, 1996; Potemra, 2001), which is a system of surface currents flowing from the Pacific to the IO through the Indonesian seas. It is the only flow between the ocean basins at low latitudes and, consequently, plays an important role in the meridional transport of heat in the climate system. This transport originates from the warm-pool of the Pacific Ocean and enters into the colder waters of the South Equatorial Current of the IO.

The Indo-Pacific atmospheric linkage has been documented previously (Cadet, 1985; Reason et al., 2000). In terms of an oceanic teleconnection, variability of the Pacific Ocean is known to be transmitted to the IO (reference). However, the involvement of off-equatorial Pacific processes is not clear.

In a recent study utilizing XBT sections since 1983, Wijffels and Meyers (2004) show that part of the thermal variance on seasonal and interannual time scales in the EIO can be accounted for by Kelvin and Rossby waves. These waves are generated by remote zonal winds along the equator of the Pacific Ocean. Much of the rest of the variance in the EIO is generated by local winds. Wijffels and Meyers (2004) provide observational evidence that variations in zonal Pacific equatorial winds force a response in the IO, primarily along the WA coast (Clark, 1991; Clark and Liu, 1993; Meyers, 1996; Masumoto and Meyers, 1998; Potemra, 2001; Potemra et al., 2002). These previous studies suggest that the energy off WA arises from equatorial Rossby waves generated by zonal wind anomalies in the central equatorial Pacific. These become coastally trapped waves where the New Guinea coast intersects the Pacific equator. Cai et al. (2005d) examined the relationship between the temperature distribution along a Fremantle to Java XBT section and variability of the equatorial Pacific to investigate the ENSO recharge-oscillator paradigm (Jin, 1997a; 1997b; Meinen and McPhaden, 2000). This study confirmed the transmission of coastally trapped wave to the central WA coast. However, Cai et al. (2005d) study is limited to the analysis of one XBT line, and a detailed pathway is not fully established.

The following section begins by examining the pathway using a thermal analysis covering the whole Indo-Pacific domain during 20 years since 1980. The robustness of the amount of energy transmission via each of the pathway in the pre-1980 period is examined to show that there are significant differences to the post-1980 period. The presence of such multidecadal variability in the CSIRO Mk3.5 is also examined.

### **3.1.3 Details of data used**

The thermal analysis is the operational subsurface temperature analysis from the Australian Bureau of Meteorology Research Center (Meyers et al., 1991; Smith, 1995a, 1995b), which is an optimal interpolation on a 1°C latitude by 2°C longitude grid at 14 depth levels, throughout the Indo-Pacific basin. It is based primarily on XBT profiles and

time-series from the Tropical Atmosphere Ocean buoy array (McPhaden et al., 1998), and covers a 20-year period since 1980. The data in the Pacific Ocean domain has been used in numerous studies (Meinen and McPhaden, 2000; Cai et al., 2004; Kessler, 2002). The relationship of oceanic variability to the wind field is documented with data from the NCEP reanalysis (Kalnay et al., 1996). To focus on interannual time scales, a 13-month running mean operation is applied before analysis.

We utilize the newly available reanalysis of SODA-POP (version 1.4.2) (Carton and Giese, 2005b). The new model product uses the European Center for Medium Range Forecasts ERA-40 atmospheric reanalysis winds. It has a spatial resolution of  $0.5^{\circ}\text{C}$  latitude by  $0.5^{\circ}\text{C}$  longitude grid, and covers a period from 1958 to 2001. Both the SODA-POP and BMRC reanalyses independently incorporated Expendable Bathythermograph profiles and time-series from the Tropical Atmosphere Ocean buoy array (McPhaden et al., 1998). We find that there are remarkable differences in the transmission between the pre- and post-1980 periods.

To examine the robustness of such multidecadal variability, we take outputs of a multi-century control experiment with the new CSIRO coupled climate model (version 3.5). The new version simulates a more realistic transmission process, although it still suffers from the common cold tongue bias, i.e., the equatorial Pacific cold tongue extends too far west. The ENSO frequency is reasonably simulated as reported earlier (Cai et al., 2003b), but the amplitude is too large. Despite these deficiencies the model produces similar multidecadal variations in the transmission.

## **3.2 Indo-Pacific transmission in the post-1980 period**

### **3.2.1 ENSO discharge/recharge signals within the Indo-Pacific system**

A CEOF analysis is applied to the filtered thermocline anomalies in the whole Indo-Pacific domain (see Chapter 2 for details) to investigate the equatorial Pacific discharge/recharge process and the propagation of off-equatorial Rossby waves. Since variance of thermocline anomalies is much greater in the equatorial than in the off-equatorial region, to enhance the spatial coherence, the grid point anomalies are normalized to have unit variance. The CEOF analysis brings out additional features at higher latitudes associated with the ENSO process. The spatial pattern is further documented using a simple lag-correlation analysis.

The recharge-oscillator paradigm (Jin, 1997a; 1997b) states that El Niño is preceded by a buildup of heat content with a deepened thermocline and followed by a heat deficit with an anomalously shallow thermocline, which in turn precedes a La Niña event. The characteristics of this paradigm were validated from analysis of the upper Pacific Ocean heat content over the past two decades (Meinen and McPhaden, 2000). They showed that the first and second EOF of equatorial Pacific thermocline anomalies (their Fig. 3), represented by anomalies of  $20^{\circ}\text{C}$  isotherm depth (D20), account for a similar percentage of the total variance, and together EOFs 1 and 2 describe ENSO cycles with a phase lag of approximately  $90^{\circ}$ . EOF1 has a zonal dipole structure representing the mature phase

of ENSO, and EOF2 a zonal symmetric pattern indicating the recharge/discharge phase. The CEOF analysis discussed below allows an exploration of the transition between these two EOFs. Although we focus on El Niño and the associated discharge, the features discussed below apply to the opposite phase, i.e. La Niña and the associated recharge.

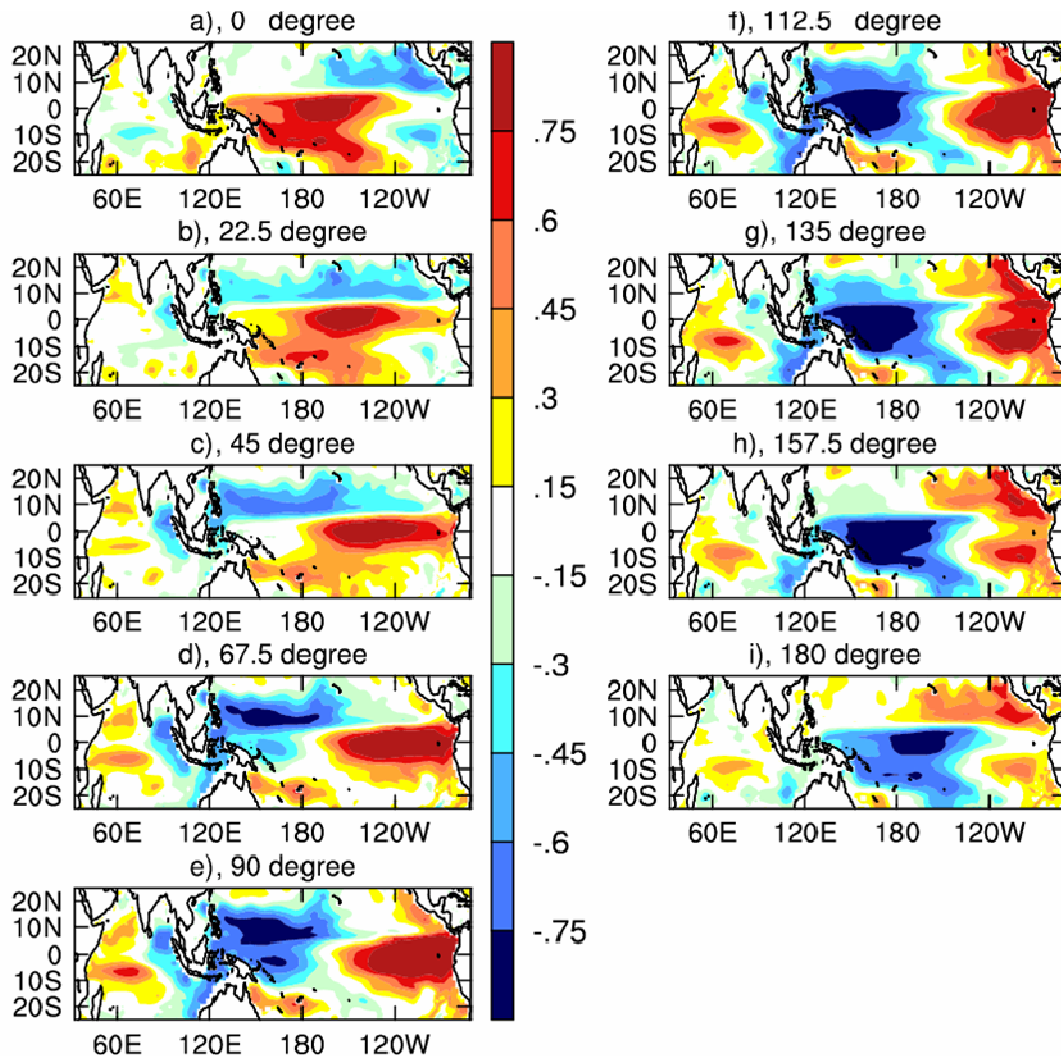


Figure 3.1: Evolution of normalized D20 anomaly pattern obtained from CEOF analysis in the whole Indo-Pacific domain covering half of an ENSO cycle at a phase interval of  $22.5^\circ$ . Negative values are in dashed contour.

Figure 3.1 displays half a cycle of the leading CEOF mode of the D20 anomalies, which accounts for 53% of the total variance, at a phase interval of  $22.5^\circ$  corresponding to a time interval of approximately three months for a four-year ENSO cycle. At phase  $0^\circ$ , the pattern in the equatorial Pacific ( $10^\circ\text{S} - 10^\circ\text{N}$ ) corresponds to the recharged phase, and at

phase  $90^\circ$ , the pattern corresponds to the mature phase of an El Niño with a zonal dipole in the equatorial Pacific, and at phase  $180^\circ$ , to the discharged phase.

The extension to the off-equatorial region brings out several additional features, i.e., the involvement of the off-equatorial Rossby wave processes (Cai et al., 2005c). At phase  $0^\circ$ , upwelling Rossby wave (indicated by negative contours) develops and radiates from the eastern boundary. At phase  $22.5^\circ$ , the upwelling Rossby wave is reinforced in the off-equatorial NP in the vicinity of ( $155^\circ\text{W}$ ,  $17^\circ\text{N}$ ). Subsequently, the Rossby wave experiences a strong growth south of  $10^\circ\text{N}$ , and propagates westward. It impinges on the western boundary, moves equatorward and then reflects back on the equator as an equatorial Kelvin wave (phase  $25^\circ$  to phase  $67.5^\circ$ ). This equatorward movement was first identified by (Godfrey, 1975), who named it the Kelvin-Munk wave, and was confirmed by the (McCreary, 1983) study. The reflected Kelvin wave then switches into a coastally-trapped wave and propagates poleward along the WA coast, a path discussed by previous studies (Clark, 1991; Clark and Liu, 1993; Meyers, 1996; Masumoto and Meyers, 1998; Potemra, 2001; Potemra et al., 2002) contributing to a discharged phase of an El Niño at phase  $180^\circ$ . The evolution described above strengthens the notion that the recharge-oscillator paradigm is consistent with the delayed-oscillator paradigm (Jin, 1997a; 1997b).

After reaching the central WA coast, the discharge radiates westward into the IO  $20^\circ$ - $30^\circ$  of longitude. Thus an increasingly large area of the IO is seen to participate in the discharge process. The discharge off WA reaches a maximum approximately three months after an El Niño peaks (phase  $112.5^\circ$ ). Thus some of the signal along the central WA coast can be traced to the off-equatorial NP in the vicinity of ( $155^\circ\text{W}$ ,  $17^\circ\text{N}$ ), where the Rossby wave initially appeared. This NP transmission "ray-path" is further discussed below in a simple correlation analysis.

### **3.2.2 The off-equatorial NP ray-path**

The off-equatorial NP ray-path is further illustrated by a lag-correlation analysis of D20 and zonal wind stress anomalies with time series of D20 anomalies averaged over a central WA box (Fig. 3.2). To compare with Fig. 3.1, the time series is sign-reversed so that a discharge signal is represented by negative correlation. Maximum discharge on the WA coast appears at Lag 0, and at Lag -3 it corresponds to an El Niño peak. Overall, there is strong similarity between Figs. 3.1 and Fig 3.2, suggesting that the WA anomaly is predominantly generated by ENSO processes (Wijffels and Meyers, 2004; Cai et al., 2005c).

Some 15 months prior to the maximum of discharge along the WA coast (Lag -15), the D20 anomaly pattern resembles that of Fig 3.1a, and the equatorial Pacific is at a recharged phase. To the east of Hawaii ( $20^\circ\text{N}$ ), negative D20 anomalies develop with reinforcing westerly anomalies immediately south. The anomalies strengthen and propagate westward for the next 6 months (Lag -12 to Lag -9) accompanied by the westerly anomalies. In the mean time, westerly anomalies develop over the Indonesian

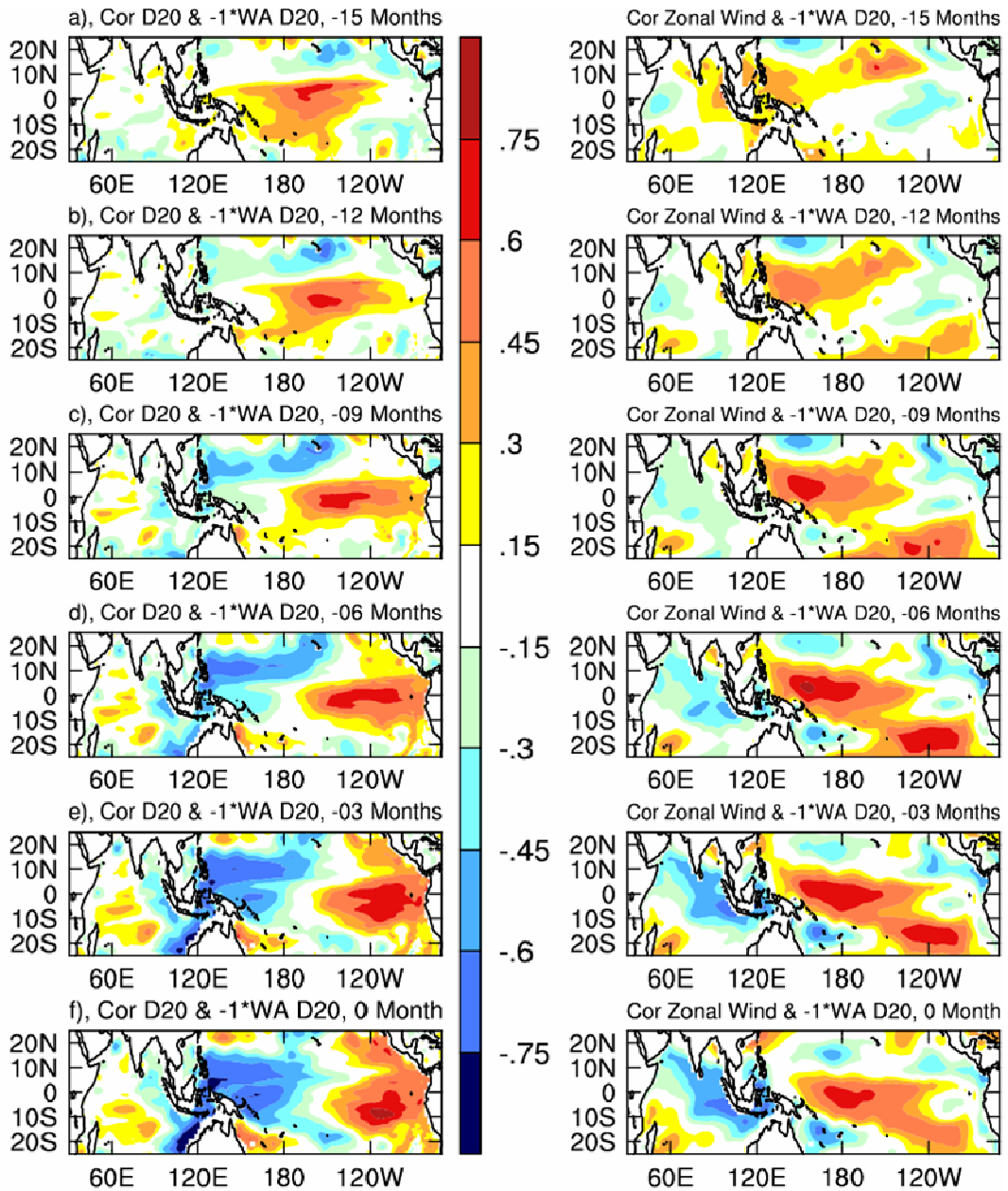


Figure 3.2: The relationship between D20 anomalies at the central WA coast (114°-118°E, 17°-22°S) and gridpoint D20 and zonal wind stress anomalies at various lags with a 3-month interval. To show a discharge signal at the WA coast at Lag 0, the WA time series is sign-reversed before analysis. Positive correlations imply deeper depths, and negative lags mean the WA D20 lags.

region (Lag -15) and subsequently in the equatorial Western Pacific (Lag -9) with a maximum at about 5°N (asymmetric about the equator) and join the westerly patch south

of Hawaii. The westerly anomalies then move eastward and southward, reinforcing the discharge, especially between  $10^{\circ}\text{N}$  and the equator. There is no southern hemispheric counterpart.

At Lag -3, the pattern is similar to that of the mature phase of El Niño (Fig. 3.2e). By this time, the intense discharge near the western boundary reaches the northwest coast of Australia. The westerly anomalies over the equatorial Pacific have become more or less symmetric about the equator, and a response in the thermocline begins to develop in the Southern Hemisphere. The equatorial westerlies generate a Rossby wave in the southern off-equatorial western Pacific (SEWP) region around  $160^{\circ}\text{E}$ . The evolution indicates that in some El Niño events easterly anomalies develop over the equatorial EIO and sometimes contributes to the development of an IOD event (Yamagata et al., 2004; Feng et al., 2002). The easterly anomalies raise the thermocline along the Sumatra-Java coast (Wijffels and Meyers, 2004), and in the months from June to November induce an enhanced evaporative heat loss (Hendon, 2003). Both processes are conducive to the development of cold anomalies off the Sumatra-Java coast. Note that NOT all El Niño events are associated with an IOD; this is underscored by the small anomaly off the Sumatra-Java coast.

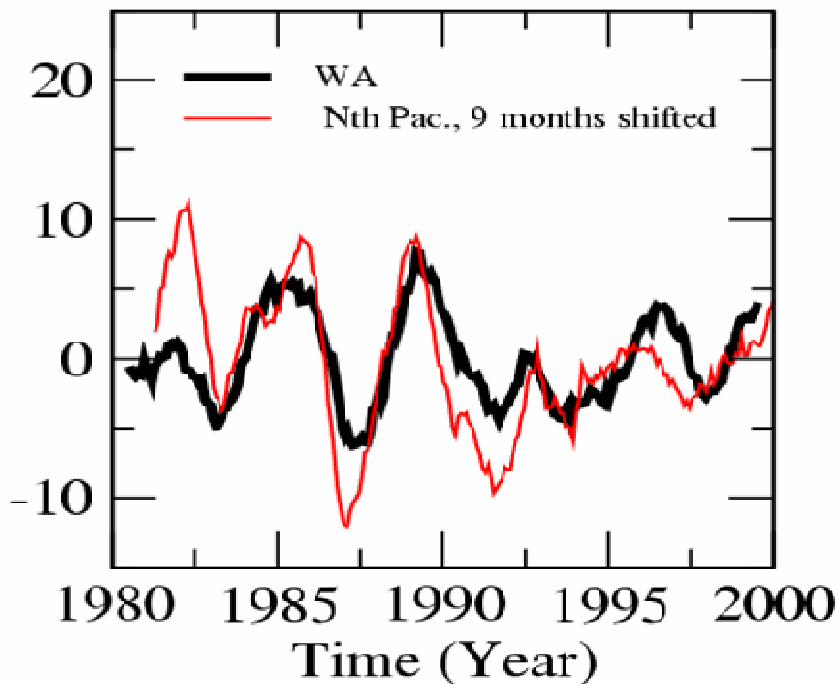


Figure 3.3: Time series of D20 anomaly at the central WA coast (thick solid) and at off-equatorial NP (thin solid) ( $150^{\circ}$ – $155^{\circ}\text{W}$ ,  $17^{\circ}$ – $22^{\circ}\text{N}$ ). Since the WA time series lags that of the NP by 9 months, the NP time series is shifted forward by 9 months to maximize the correlation. (From Cai et al., 2005c).

At Lag 0, approximately 3 months after the mature phase of El Niño, the signal along the central WA coast reaches a maximum. The westerly anomalies in the equatorial Pacific have moved further south (Harrison and Vecchi, 1999), the maximum residing at the southern equatorial latitudes. Meanwhile, easterlies develop in the EIO and the far western equatorial Pacific (Wang, 2001). Equatorial Kelvin waves generated by these processes and by the off-equatorial Rossby wave reflection contribute to the demise of the warm condition in the eastern Pacific.

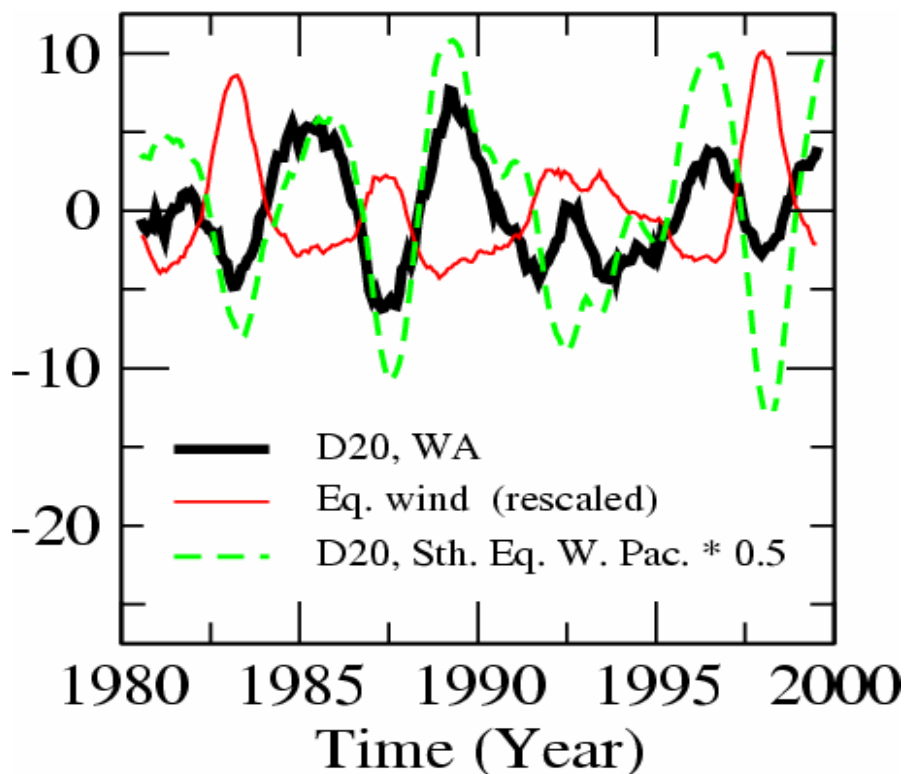


Figure 3.4: Time series of D20 anomalies at the central WA coast (black) wind stress anomalies in the Niño3.4 ( $120^{\circ}$ – $170^{\circ}$ W,  $5^{\circ}$ S– $5^{\circ}$ N) region (red, rescaled for plotting) and D20 anomalies in the SEWP ( $155^{\circ}$ – $160^{\circ}$ E,  $0^{\circ}$ – $5^{\circ}$ S) region (dashed, rescaled for plotting by multiplying a factor of 0.5 because of a larger amplitude than the WA D20 time series). (From Cai et al., 2005c).

One of the surprising results of this analysis is that the discharge in the IO appears to be linked to the region near Hawaii (Figs. 3.2d and 3.2e). The link is further illustrated in Fig. 3.3, which plots the time series of D20 anomalies along the central WA and averaged

over an off-equatorial NP box ( $17^{\circ}\text{N}$ - $22^{\circ}\text{N}$ ,  $155^{\circ}\text{W}$ - $150^{\circ}\text{W}$ ). Because the NP time series leads the WA time series by about 9 months, the former is shifted forward by 9 months. A strong coherence is seen (with a correlation of 0.75 at a 9-month lag, meaning that at least 55% of the interannual variance of the WA thermocline anomaly is linked to that near Hawaii). The coherence is further highlighted by a common lack of strong D20 anomalies during the 1997/1998 El Niño. A strong discharge in the 1997/98 event was confined in the equatorial Pacific (Meinen and McPhaden, 2000, their Fig.3).

Previous studies (e.g., Wijffels and Meyers, 2004) find that there is little lag between anomalies along the central WA coast and the equatorial Pacific wind. Figure 3.4 plots the central WA D20 time series (black curve) and zonal wind anomalies averaged over Niño3.4 region (red curve). The Niño3.4 (or Niño4) wind leads the WA D20 by one month with a correlation of 0.68. The wind leads D20 averaged over a SEWP ( $0^{\circ}$ - $5^{\circ}\text{S}$ ,  $155^{\circ}\text{E}$ - $160^{\circ}\text{E}$ ) box (dashed curve, Fig. 3.4) by two months with a correlation of 0.85. (Note that the SEWP time series shows a large recharge/discharge associated with the 1997/1998 event.) The small lag of the WA and SEWP thermocline variations relative to the equatorial Pacific wind is consistent with the Wijffels and Meyers (2004) result, and the small lag among these indices suggests that the NP signal leads all these indices by a similar amount of time, about 7-9 months.

The picture that emerges from Fig. 3.2 is that thermocline anomalies initially develop at NP some 7 months prior to the mature phase of ENSO. As ENSO develops, the off-equatorial zonal wind anomalies join the zonal wind anomalies over the northern western Pacific and move eastward and southward, reinforcing the NP D20 anomalies as they propagate westward and equatorward. Consequently, the peaking of the equatorial Pacific wind and the western boundary reflection occur nearly simultaneously. In the subsequent 2 months, the NP anomaly reaches the WA coast, hence the 9-month lag.

### **3.3 Comparison between the pre-1980 and post-1980 period**

#### **3.3.1 Data quality of the SODA-POP analysis**

We now use the SODA-POP (see section 2.1.1) reanalysis to examine the robustness of the amount of energy that leaves the Pacific via each of the pathway. The reanalysis reproduces many features of observations. Figure 3.5 compares various results between SODA and the observed GISST data set. You can see that it performs very well. The red line is the SODA results, while black line represents the GISST data. First panel shows the Niño3.4 generated by both data. Second panel shows the warm water volume anomaly. Warm water volume is defined as the volume of water above the thermocline. The third panel shows the EIO sea surface temperature anomaly. As one can see the SODA performs quite well in all the experiments. This gives us confidence in using the SODA data.

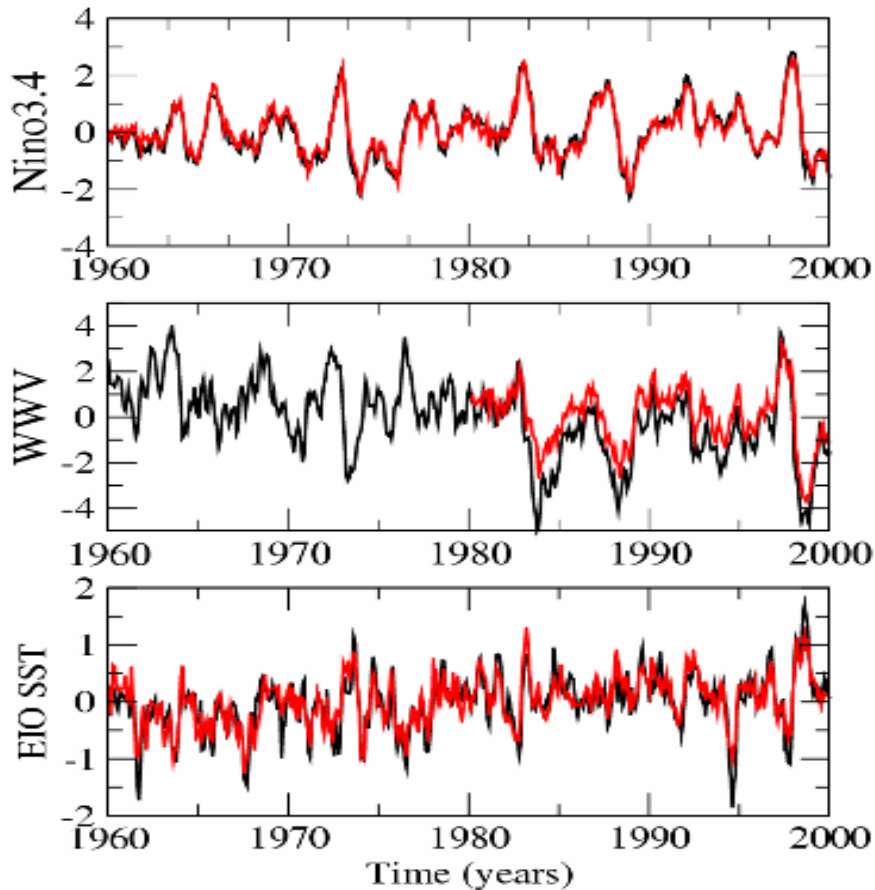


Figure 3.5: Comparisons of SODA and GISST data. Black line represents SODA, while red line represents GISST.

### 3.3.2 Decadal difference of the Indo-Pacific transmission

Figure 3.6 displays the lag-correlation between Niño3.4 and D20 at various lags for the post-1980 (left column) and pre-1980 (right column) from SODA-POP. Because of the significant differences between ENSO properties, we decide not apply any filtering. The ENSO cycle is well simulated in both periods but with noticeable differences. The meridional extent is narrower in the pre-1980 period. This difference, and the feature of stronger ENSO since 1980, has been observed by previous studies (Wang, 1995; Wallace et al., 1998; Wang and An, 2001). A central difference is that little signal is transmitted into the IO in the pre-1980 period.

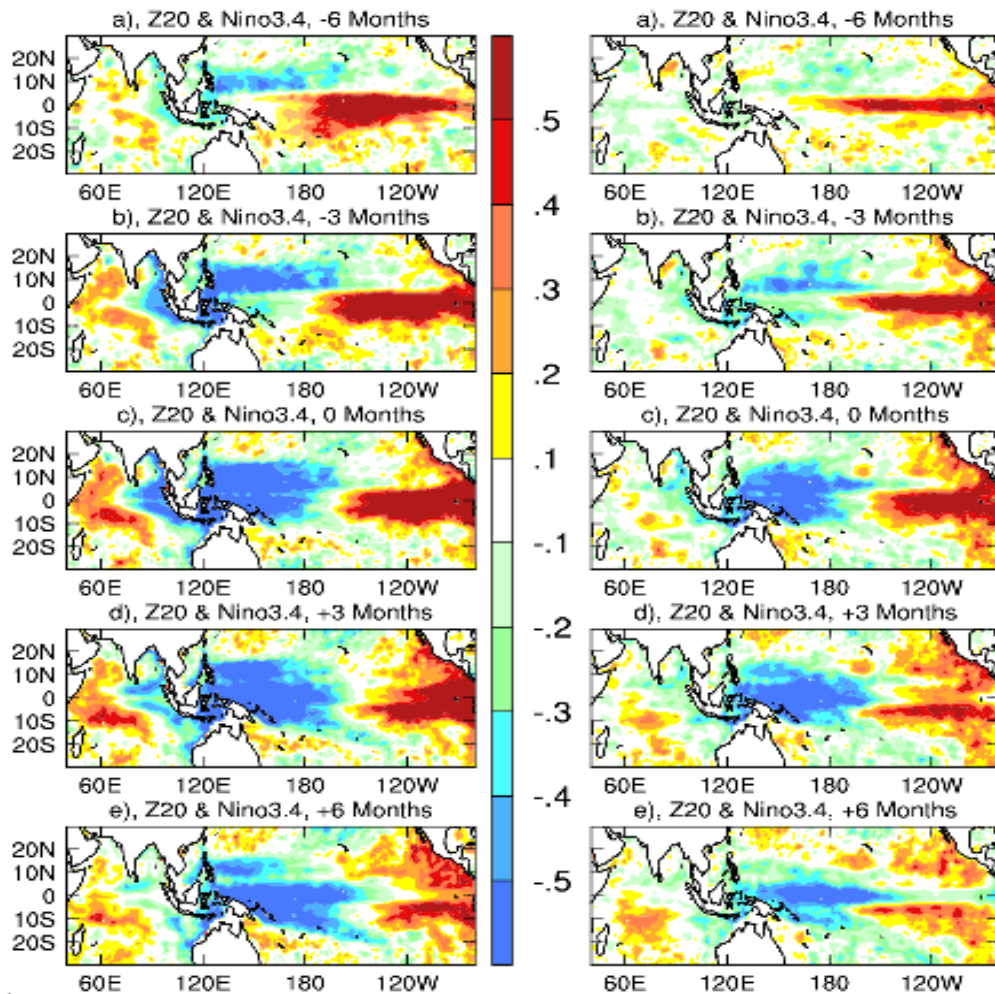


Figure 3.6: Outputs from the SODA-POP reanalysis (Version 1.4.2), showing correlation between Niño3.4 and gridpoint D20 at various lags with a 3-month interval. Positive correlations imply deeper depths, and negative lags mean the Niño3.4 lags. Left column is for the post-1980 and right column for the pre-1980 period. A value of 0.28 indicates statistical significance at 95% confidence level (from Shi et al., 2007).

In the post-1980 period (left column), 7-9 months prior to the peak of an El Niño, the pattern in the equatorial Pacific ( $5^{\circ}\text{S}$ - $5^{\circ}\text{N}$ ) shows a recharged phase, but an off-equatorial upwelling Rossby wave (indicated by negative contours) develops and radiates from the eastern boundary, and is reinforced in the vicinity of ( $155^{\circ}\text{W}$ ,  $17^{\circ}\text{N}$ ). After a strong growth en-route westward, it impinges on the western boundary, moves equatorward and then reflects back as an equatorial Kelvin wave (Lag -3). The reflected Kelvin wave then forces a coastally-trapped wave, which propagates poleward along the WA coast, contributing to a discharged phase of an El Niño at Lag 0. The discharge off the WA coast reaches a maximum approximately three months after an El Niño peaks (Lag +3). Thus some of the signal along the central WA coast can be traced to the subtropical NP. This is the subtropical NP pathway described by (Cai et al., 2005c) and SODA-POP

simulates this well. The phase speed of the off-equatorial Rossby waves is far faster than that of observed Rossby waves (Chelton and Schlax, 1996; Cipollini et al., 2001); however, these waves are not free Rossby waves but are strongly controlled by wind anomalies or by the atmosphere-ocean coupling (Cai et al., 2005c).

Rossby waves in the pre-1980 period are closer to the equator, mostly within about 10°S-10°N. As a result, there is little transmission via the subtropical NP pathway. This is further illustrated in Fig. 3.7, which shows lag correlation between D20 at the NP western boundary (Philippine Sea box, 120°E-125°E, and 12.50°N-17.5°N) and D20 everywhere. To compare with Fig. 3.6, the Philippine Sea D20 is sign-reversed so that a discharge signal is represented by negative correlations. Rossby wave propagation is seen in both periods, but in the post-1980 period (left column), there are strong coherence between ENSO and NP Rossby waves and clear signal transmission to the WA coast; these features are virtually absent in the pre-1980 period (right column).

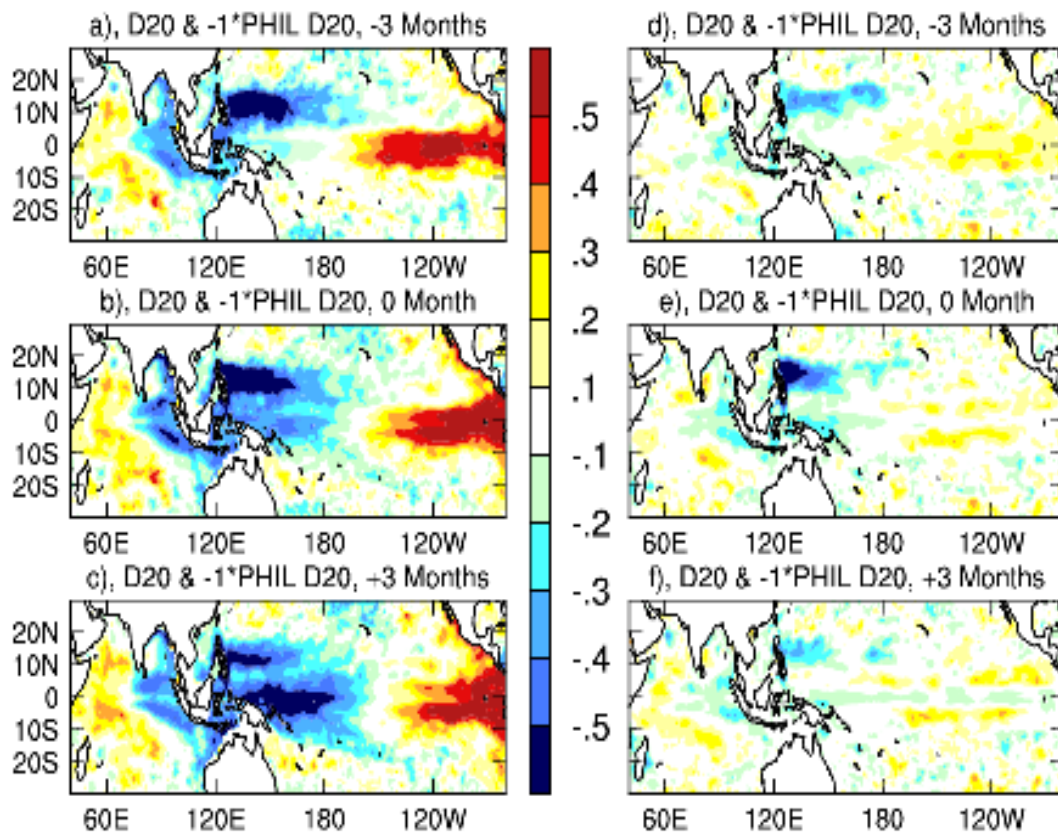


Figure 3.7: The same as Figure 3.6, but with time series of D20 in a Philippine Sea box (120°E-125°E, 12.5°N-17.5°N). To show discharge signals the Philippine Sea D20 is sign-reversed before analysis for comparisons with Figure 3.6 (Shi et al. 2007).

### 3.3.3 Decadal difference of the importance of the off-equatorial NP pathway

Does the energy leave the Pacific Ocean via the equatorial pathway in the pre-1980 period? We conduct a lag-correlation analysis of D20 anomalies with time series of D20 anomalies averaged over a central WA box (112°E-120°E, 15°S-22°S) (Fig. 3.8). To compare with Fig. 3.6, the WA D20 is sign-reversed. Maximum discharge off the WA coast appears at Lag 0, and at Lag -3 it corresponds to an El Niño peak (at Lag 0 in Fig. 3.6).

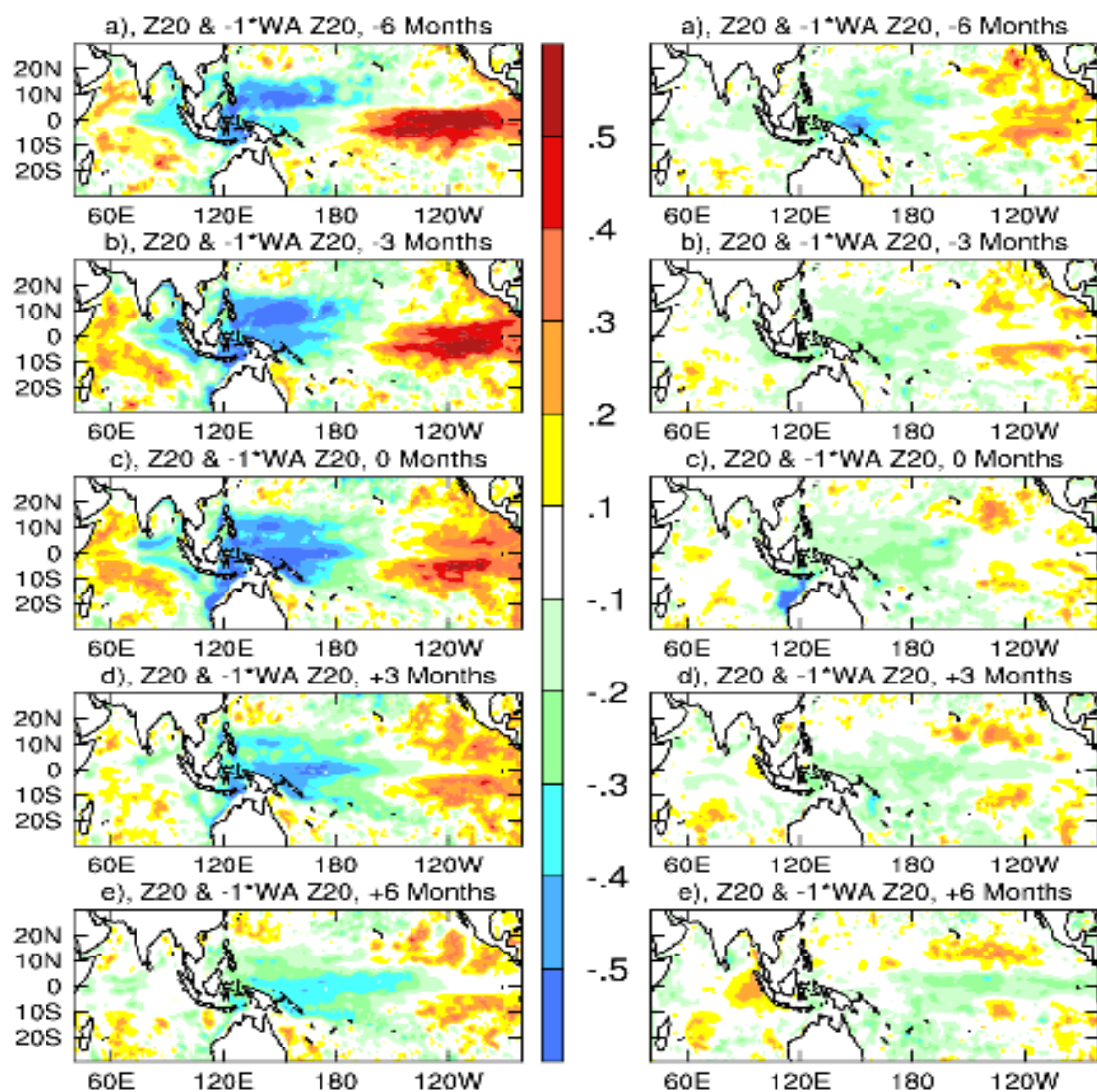


Figure 3.8: The same as Figure 3.7, but with time series of D20 averaged over a central WA box (112°E-120°E, 15°S-22°S). To show discharge signals the WA D20 is sign-reversed before analysis for comparisons with Figure 3.6 (from Shi et al., 2007).

For the post-1980 period (left column, Fig. 3.10) there is a strong similarity between Fig. 3.6 and Fig. 3.8, and the WA anomaly is predominantly generated by ENSO processes. In the pre-1980 period (right column, Fig. 3.10), the evolution is vastly different. There is little correlation between WA D20 and anomalies elsewhere at most lags, except at Lag -6, when weak but significant correlations exist in the western equatorial Pacific. Corresponding maps of correlation with zonal winds also show a maximum in the western equatorial Pacific at Lag -6, implying that some Pacific signals do propagate through the equatorial pathway. Nevertheless, the overall lack of correlation suggests that in the pre-1980 period the transmission via the equatorial pathway is so weak that it does not manifest above the stochastic noise.

What we have described above is the difference of the statistical properties between the two periods. Within each period, the proportion of energy transmission via each pathway varies significantly from one event to another; for example, in the 1997 event, transmission via the NP pathway is smaller than that via the equatorial pathway. Despite this, it is rather significant that the statistical property of events over one 20-year period is so different from that over another 20-year period, highlighting the existence of an underlying mechanism.

The thermocline in the Pacific Ocean has been changing on decadal timescales, and affects the IO (McPhaden and Zhang, 2002; Annamalai et al., 2005). Our results indicate that the stronger post-1980 ENSO discharge signals also contribute to a shallowing thermocline in the southern tropical IO and therefore also affect the development of the IOD, by pre-conditioning a shallower thermocline. This is evident from a better defined IOD pattern during the post-1980 period (Fig. 3.6, lowest panel).

### **3.3.4 The dynamics for the decadal difference**

Pre-1980 ENSO events are weaker and have a narrower meridional extent than the post-1980 ENSOs (Fig. 3.6) (Wang, 1995). Does such multidecadal variability in the ENSO properties contribute to the difference in the pre- and post-1980 transmission? We take outputs of the new CSIRO multi-century control experiment and examine if similar multidecadal variations exist. Time series of WA D20 and Niño3.4 are constructed from the coupled model outputs and a 20-year sliding window is used to calculate the correlation between them at Lags +3 and +6 (Fig. 3.11, black and blue curve). We calculated more than one lag in case the model transmission signal does not peak at exactly the same time as in SODA-POP.

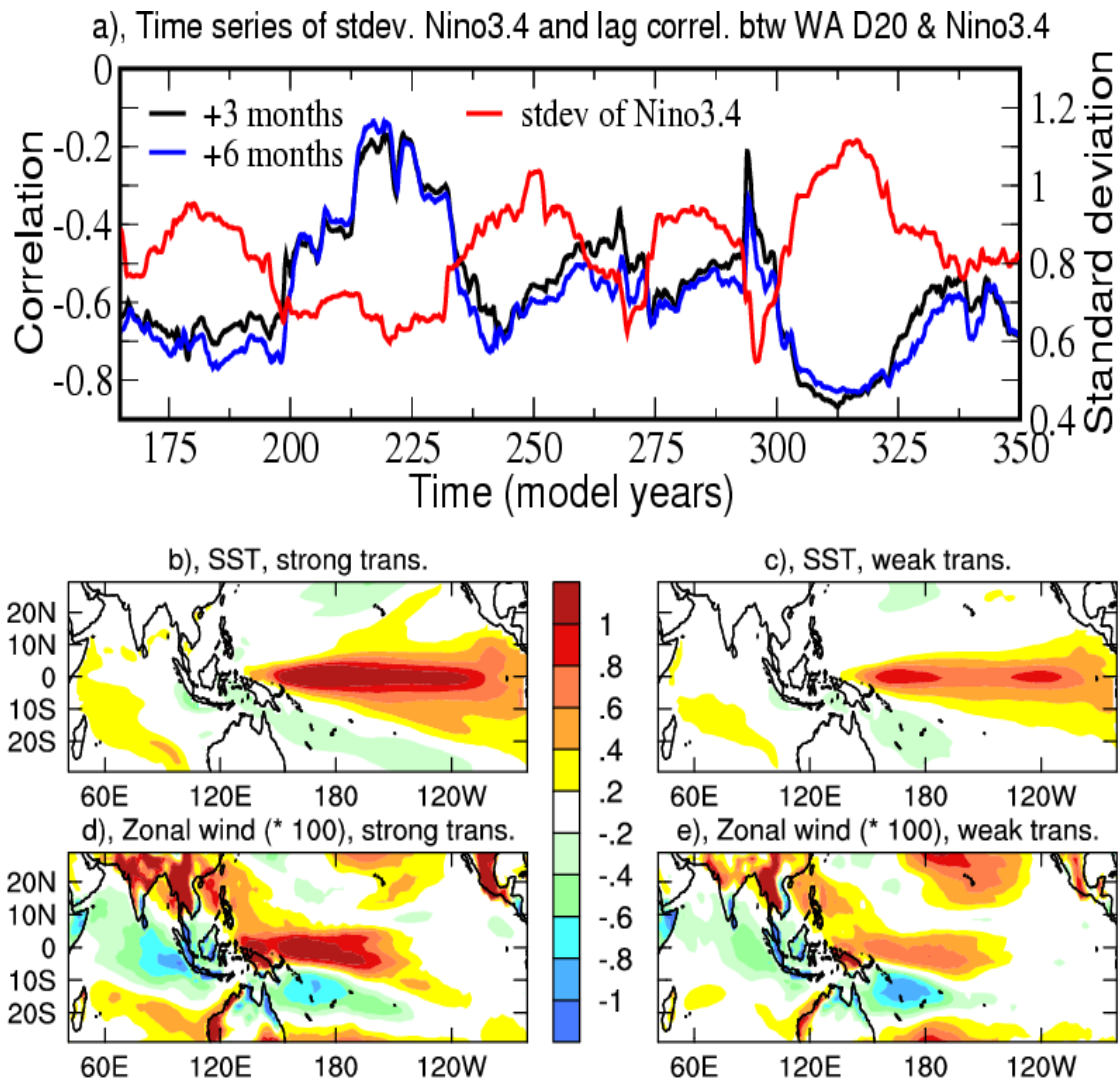


Figure 3.9: Coupled model results: a), time series of correlation between Niño3.4 and the WAD20 at Lags +3 (black curve) and +6 (blue) (i.e., 3 months and 6 months, respectively, after an ENSO event peaks), and time series of standard deviation of Niño3.4 (red curve), calculated using a 20-year sliding window; b) and c), patterns of one-standard deviation anomalies of SST and zonal wind associated with ENSO for a strong transmission period (year 315); d) and e), the same as b) and c) but for a weak transmission period (year 215) (from Shi et al., 2007).

The model transmission undergoes similar multidecadal fluctuations: in some 20-year periods the correlation is not significant, i.e., little is transmitted or generated; in other periods the correlation reaches as high as 0.8 (Shi et al., 2008). A time series is constructed of standard deviation of Niño3.4 using a 20-year sliding window (red curve, Fig. 3.9a). The amplitude fluctuates significantly, between about 0.6°C and 1.1°C. The central point is that a strong correlation exists between the standard deviation curve (red)

and the Lag +3 curve (black) with a correlation of 0.79: a strong transmission is seen when ENSO events are strong, and vice versa. Maps of correlation (not shown) between Niño3.4 and D20 everywhere and between the WA D20 and D20 everywhere for the strong (centered at year 315) and weak (centered at year 215) transmission periods resemble those of Figs. 3.1 and 3 for the post- and pre-1980 periods, respectively. There is little involvement of the subtropical NP pathway and the meridional extent of the ENSO anomaly is narrower during the weak transmission period (year 215).

These contrasts are also reflected in maps of one-standard deviation anomaly patterns of SST and surface wind associated with ENSO for the strong (left column, Fig. 3.9) and weak (right column, Fig. 3.9) transmission periods, reminiscent of the difference between the post- and pre-1980 periods in SODA-POP. During strong-ENSO periods, the tropical Indo-Pacific system is overwhelmed by ENSO signals; therefore the ratio of “ENSO signal to stochastic noise” is greater than that during weak-ENSO periods. To illustrate this, we define “signal” as the standard deviation associated with the Niño3.4, determined from a linear regression onto the Niño3.4 index, and “noise” as the standard deviation of the residual after removing ENSO signals (see Shi et al., 2007 for further discussion). Maps of such ratios for D20 for SODA-POP and the coupled model are displayed in Fig. 3.10. The ratios are generally much larger for the strong-ENSO periods. The results are therefore consistent with the multidecadal variation of the Indo-Pacific teleconnection depicted in Figs. 3.6-3.9, and provide an explanation as to why in weak-ENSO periods a transmission signal might not manifest itself above stochastic noises.

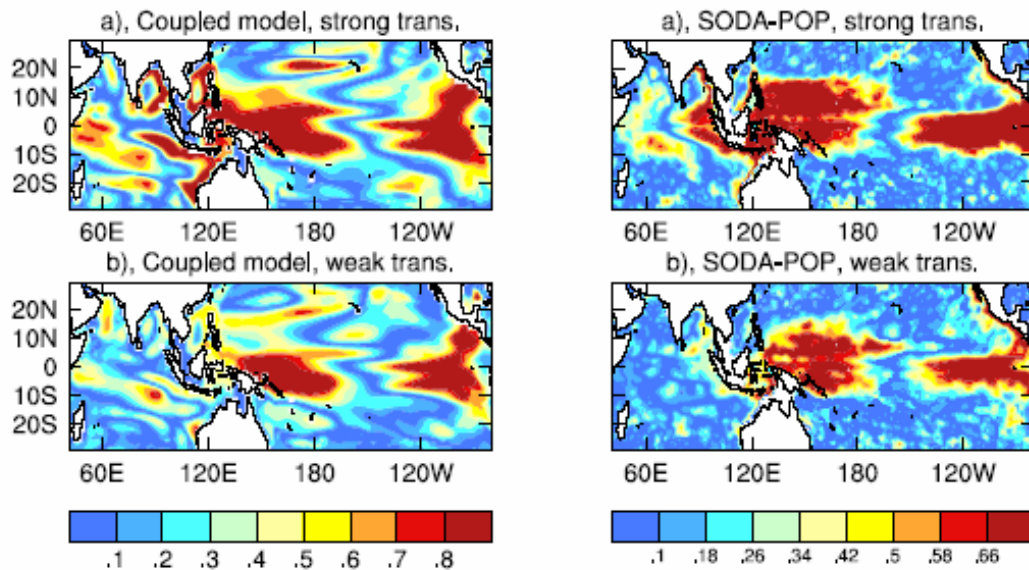


Figure 3.10: Maps of “signal to noise” ratio defined as the standard deviation of a signal over the standard deviation of noise for the coupled model (left column) and SODA-POP (right column) in terms of D20. See text for details. Upper row shows patterns for a strong transmission period (model year 315, and post-1980) while lower row shows those for a weak transmission period (model year 215 and pre-1980 SODA)(from Shi et al.,(2007).

### 3.4 Contribution of decadal differences to IO temperature trends

Figure 2.4b has already shown the difference in 20°C isotherm between the post-1980 and pre-1980 period (post-1980 minus pre-1980). It clearly indicated a general shallowing in the southern off-equatorial IO region during the positive Interdecadal Pacific Oscillation phase which creating a favourable condition for the IOD. Although off the Sumatra-Java coast, the difference is small, it has been shown that it affects the winter and spring Australian rainfall teleconnection.

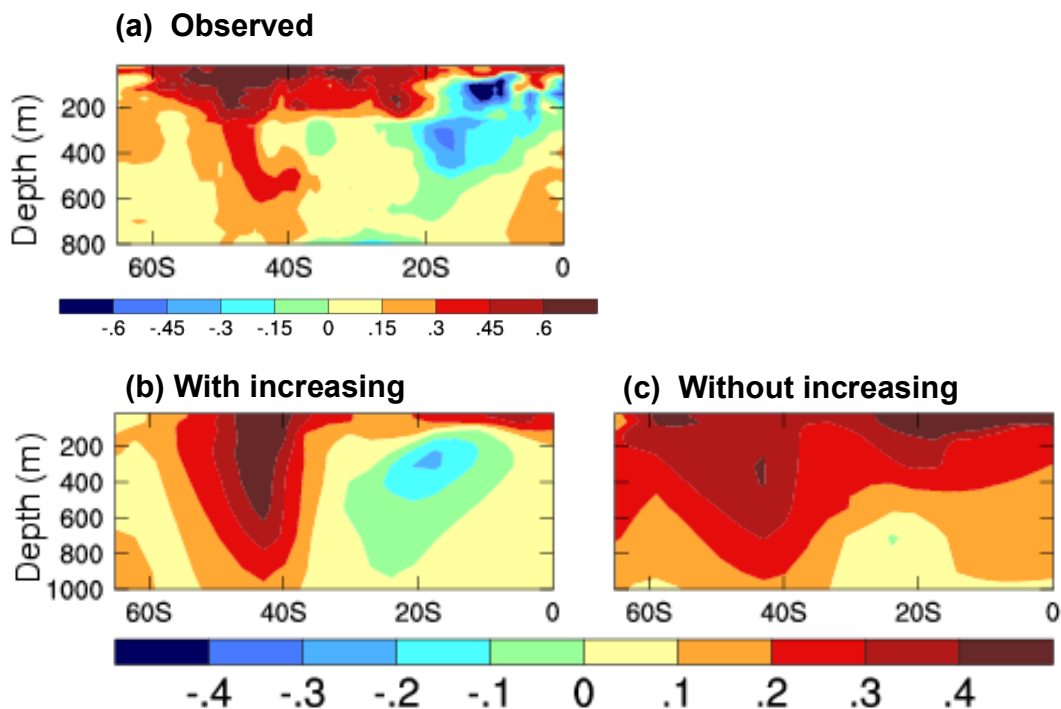


Figure 3.11: (a) Observed zonally averaged temperature trend since 1960 ( $^{\circ}\text{C}$  per 50 years). (b) The same as (a) but in a model ensemble (eight members) with all forcing including solar variability, volcanic, ozone, increasing aerosols, increasing  $\text{CO}_2$ . (c) The same as (c), but with aerosol fixed at pre-industrial level (from Cai et al., 2007).

It turns out that the stronger transmission in the post-1980s, compared with the pre-1980 period, is also an essential ingredient of the structure of the IO warming trend. Historical data (Rayner et al., 1996) show that since 1950 the warming trend of SST is not uniform across the SH subtropical latitudes, but is the largest in the IO (see Fig. 1a in Cai et al., 2007). Such a pattern was not simulated by early climate models, which, under increasing  $\text{CO}_2$ , produced a fast warming rate in the northern Hemisphere, and a much slower warming rate in the SH subtropical oceans (Cai and Whetton, 2001). The deficiency was attributed to some long-standing problems including a weakly stratified, overly convective modelled Southern Ocean (Hirst and Cai, 1994; Toggweiler et al., 1989).

Implementation of an eddy-induced transport parameterization (Gent and McWilliams, 1990; Duffy et al., 1995) onto the Cox (1987) isopycnal scheme improved the stratification but the model problems persisted. The inclusion of increasing aerosol forcing reduces the northern Hemisphere large warming rate (Mitchell et al., 1995). Cai et al. (2007), show that aerosol forcing also improves the structure of warming trends in the SH subtropical ocean, particularly the southern IO sector. However, one feature of the structure cannot be explained without invoking the stronger transmission of the stronger El Niño events in the post-1980 period.

Using a new compilation of historical temperature profiles, the IO Thermal Archive (IOTA), Alory et al.(2007) show that the subtropical zonal-mean IO surface warming penetrates to an 800m depth (Fig. 3.11a), and that models of the IPCC Fourth Assessment Report (AR4) running 20th century experiments capture this surface to deep ocean warming trend. The off-equatorial IO surface warming in IOTA is accompanied by a subsurface cooling, which displays two centres, one 10°S at a 100m depth, and the other 17°S at 400m. Our results suggest that the subsurface cooling at 100m depth is due to the stronger transmission of the ENSO discharge signal in the post-1980 period, as a result of stronger and protracted El Niño events since 1980.

Although the majority of the IPCC experiments include an aerosol forcing, there is no outputs from the same model that singles out the impact of aerosol forcing. Cai et al. (2007) analyse outputs from two newly available ensemble sets, one with aerosols fixed at the pre-industrial level and another that incorporates increasing aerosols through an interactive aerosol scheme (Rotstayn et al., 2007). The study finds that once increasing aerosol forcing is included, most of the structure is reproduced. This includes the stronger surface warming in the subtropical IO than that in other subtropical oceans, the latitude-depth structure (Figs. 3.11b and 3.11c) with the warming penetrating to 800m, and the subsurface cooling at 400m. The subtropical IO warming and the cooling at 400-m depth are due to a stronger Agulhas outflow and its retroflexion, which are in turn driven by an aerosol-induced pan-oceanic ocean circulation change. The increasing aerosols cool both the northern Hemisphere and SH oceans through a strengthening cross-hemispheric transport from the SH oceans to the northern Hemisphere oceans (Cai et al., 2006), particularly to the North Atlantic, mitigating an increasing CO<sub>2</sub> - induced slowdown of the North Atlantic Deep Water Formation (NADWF). The heat needed to mitigate the NADWF is derived from the off-equatorial subsurface ocean, leading to the subsurface cooling at 400m. The subsurface cooling 10°S at 100m does not show up in the Cai et al. (2007) analysis. This is because the model does not produce a greater ENSO discharge after 1980. The result highlights that the decadal difference of the oceanic transmissions is essential to explain the IO warming structure over the past 50 years.

### **3.5 Summary**

The issue of whether the NP is involved in the transmission of ENSO signals into the IO is not addressed in previous studies, although it has been shown to be highly important in preconditioning IOD variability and hence Australian rainfall variability. The analysis presented here confirms that ENSO discharge/recharge arrives mainly at the central WA

coast. The transmission involves an off-equatorial NP ray-path whereby the discharge/recharge anomaly, after an initial development near Hawaii, propagates westward as a Rossby wave. After impinging on the western boundary, the Rossby wave moves equatorward along the Kelvin-Munk ray-path as proposed by Godfrey (1975), and reflects as an equatorial Kelvin wave. As the reflected Kelvin wave propagates eastward, it impinges on the Australasian continent and moves poleward along the WA coast as a coastally-trapped wave radiating Rossby waves into the south IO. Along the above path, the NP anomaly reaches the central WA coast some 9 months later. On-route to the WA coast, the anomaly is reinforced by evolving winds that are associated with ENSO. This study also finds that off-equatorial Rossby waves play a small part in the recharge/discharge during the 1997/1998 ENSO event, with a correspondingly small signal along the WA coast despite the presence of a strong discharge/recharge signal in the equatorial Pacific. We note however that equatorial Kelvin waves generated by easterly anomalies that develop at the mature El Niño phase in the far western equatorial Pacific (Wang, 2001) and by westerly anomalies that move southward from the equator (Harrison and Vecchi, 1999) also contribute to the discharge.

Using SODA-POP, we find that in the pre-1980 period, little ENSO signal is transmitted to the IO. The lack of transmission results from two interconnected factors: firstly, the NP pathway is not involved because of a narrower meridional extent of ENSO; secondly, the ENSO events are weaker leading to smaller transmission signals via the equatorial pathway that are drowned under stochastic noise. A multi-century coupled climate model experiment reproduces these features, confirming that these are not artifacts of the reanalysis system. The presence of these multidecadal fluctuations in the model without climate change forcing suggests that the stronger discharge in the post-1980 may not be greenhouse induced.

We have further shown that because of the stronger and more protracted El Niño events since 1980, a stronger discharge signal is generated over the WA coast. This then radiates into the IO. Thus, like the stronger easterly winds associated with the El Niño events, the stronger discharge also preconditions the IO thermocline, influences the IOD and Australian rainfall. Together with increasing anthropogenic forcing, the stronger discharge explains the warming of the subtropical IO, in which a surface cooling is accompanied by subsurface cooling. It is not clear how the surface warming and the subsurface cooling are linked at this stage. An intriguing aspect is that there is no consistent surface heat flux trend based on available heat flux data.

The IOD's influence occurs mainly in winter and spring. Warming in IO has occurred in all other seasons. In Chapter 4 we focus on the impacts upon NAW DJF rainfall, where, in contrast to other regions of Australia, rainfall has been increasing (Shi et al., 2008b).

# Chapter 4: North West Australian rainfall variability and trends

Since 1950, there has been an overall positive trend in rainfall over NWA. Most of the rainfall increase occurs during the SH summer season. Few studies have focused on this region. Rotstayn et al. (2007) use 20<sup>th</sup> century multi-member ensemble simulations in a global climate model forced with and without increasing anthropogenic aerosols, and suggest that the rainfall increase is attributable to increasing northern Hemisphere aerosols. This chapter investigates the dynamics of the observed trend toward increased rainfall and compares the observed trend with that generated in the Rotstayn et al.'s model (2007) forced with increasing aerosols. The candidate initiates the original idea and carried out the analyses, and receives help from co-authors who conducted the model experiments and helped organize the large amount of data. The content of this chapter derives from the Shi et al. (2008b) paper (J. Climate, in press), which arises from this Ph. D project.

The main findings are summarized below.

- The observed positive trend in rainfall is projected onto two modes of variability. The first mode is associated with an anomalously low MSLP off NWA instigated by the enhanced SST gradients towards the coast. The associated cyclonic flows bring high moisture air to northern Australia, leading to an increase in rainfall. The second mode is associated with an anomalously high MSLP over much of the Australian continent. The anticyclonic circulation pattern with northwesterly flows west of 130°E and generally opposite flows in northeastern Australia, determine that when rainfall is anomalously high, west of 130°E, rainfall is anomalously low east of this longitude.
- The sum of the upward trends in these two modes compares well to the observed increasing trend pattern.
- The modeled rainfall trend, however, is generated by a model artifact arising from model deficiencies associated with the Pacific cold-tongue bias, and therefore different from the dynamics in the model.
- It is not clear whether, in a model without such defects, the observed trend can be generated by increasing aerosols. Thus, the impact of aerosols on Australian rainfall remains an open question.

## 4.1 Background

Runoff in NWA is about 180,000 GL/year which accounts for 60% of Australia's total runoff. There is a vigorous debate as to how the nation takes advantage of this abundance of the water resource in NWA. As discussed in Chapter 1, during the past 50 years, there has been an overall positive trend in rainfall over NWA (Fig. 4.1). In an environment in which decadal-scale droughts have plagued most of the country, and the long-term rainfall over southern Australia is projected to decrease further, continued upward trends in rainfall may provide a source of future water resources for the nation. The observed annual increase is approximately 50% of the climatological value,

compared with a 15% reduction over SWWA throughout the same period (Cai and Cowan, 2006).

The strong regional contrast of the rainfall trend shown in Fig. 4.1 hides the complexity of the climate drivers controlling Australian rainfall. As discussed in Shi et al. (2008b), the influence of ENSO mainly occurs in the eastern Australia region, with El Niño (La Niña) events associated with anomalously low (high) rainfall (e.g., McBride and Nicholls, 1983; Ropelewski and Halpert, 1987; Ashok et al., 2007a). The impact of variability of IO SSTs, such as the IOD, is experienced mainly over the SEA region (Nicholls, 1989; Saji et al., 1999), in a broad band stretching from the northwest to the southeast of the continent (e.g., Ashok et al., 2003; Saji and Yamagata, 2003; Cai et al., 2005a). To the south, the SAM is the dominant mode of the SH extratropical circulation, operating beyond the weather scale (Kidson, 1988; Karoly, 1990; Thompson et al., 2000; Hartmann and Lo, 1998). It has been linked to interannual and interdecadal rainfall variations over SWWA (e.g., Cai et al., 2005d; Hendon et al., 2007; Cai and Cowan, 2006).

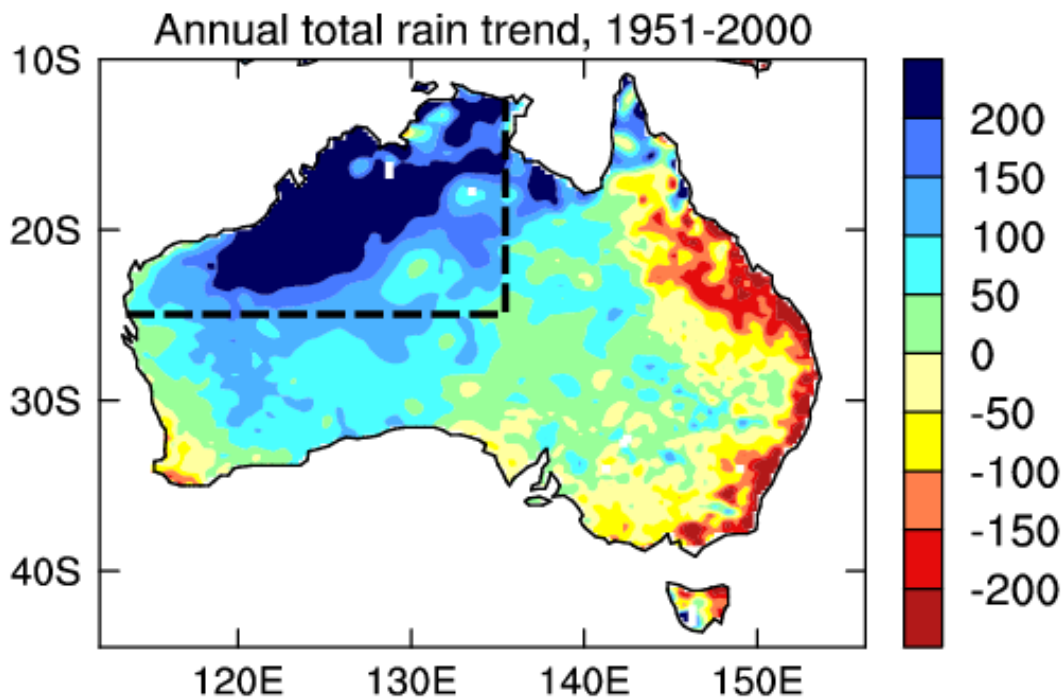


Figure 4.1: Observed annual total rainfall trend (mm) based on the BMRC rainfall data over 1951-2000 (from Shi et al., 2008b). Blue colour shows rainfall increase and red indicates rainfall reduction. The area in the Northwest corner (dotted line) is defined as NWA in this Chapter.

Substantial effort has been devoted to understand the cause of the drying trend over many regions (e.g., Smith, 2004; Cai and Cowan, 2006). For example, along the east Australian coast, observed rainfall decreases may reflect an increased frequency of El Niño events in the late 20<sup>th</sup> century, which could be linked to an increase in greenhouse

gases. Indeed, coupled atmosphere-ocean GCMs forced by increasing atmospheric CO<sub>2</sub> have simulated an El Niño-like warming pattern in the Pacific Ocean (e.g., Meehl and Washington, 1995; Cai and Whetton, 2000). This suggests the possibility that the observed rainfall decrease might be attributable to an El Niño-like warming pattern and that future average rainfall might be lower over eastern Australia. To the west, rainfall over SWWA is in part linked to a shift of the SAM towards its “positive” state, with decreased MSLP over Antarctica and increased MSLP over the SH mid-latitudes (Cai et al., 2003a; Cai and Cowan, 2006). It may also be linked to multi-decadal variability of the SAM (Cai et al., 2005a) and to land-cover change (Pitman et al., 2004).

Only two previous studies have been conducted on the dynamics of NWA rainfall variability and trends. Wardle and Smith (2004) hypothesized that during the latter half of the 20<sup>th</sup> century, the observed increase in temperature gradient between Australia and neighbouring oceans drove a stronger monsoonal circulation. By artificially altering this contrast through a change to the land Albedo in a model, they could simulate a rainfall increase over the entire continent, with stronger totals over the north. Their experiment also generated a temperature response similar to the observed. They inferred that the temperature changes were possibly leading to a strengthening of the monsoon and that this could be the cause of the increased rainfall. However, the prescribed changes were much greater than could be justified based on current knowledge, so the authors left the cause of the land-ocean temperature contrast as an open question. An alternative hypothesis for the increased northwest rainfall was suggested by Rotstayn et al. (2007) who, by using simulations from a low-resolution coupled GCM, showed that including (excluding) anthropogenic aerosol increases in 20<sup>th</sup> century simulations gives increasing (decreasing) rainfall and cloudiness over Australia. Rotstayn et al. (2007) demonstrated that the pattern of increasing rainfall, with increasing aerosols, is strongest over NWA. This seems consistent with the observed trends.

In this chapter, available observations and reanalysis data were used to examine the dynamics of observed rainfall variability over NWA and circulation patterns associated with the observed increasing rainfall trend. We then benchmark the performance of the climate model used in the Rotstayn et al. (2007) study. Our focus is on whether the model reproduces the observed variability and circulation trend associated with the increased rainfall (section 3). Our analyses illustrate that the modeled rainfall change over NWA in the Rotstayn et al. (2007) study might be a by-product of a well-known model deficiency associated with an equatorial Pacific cold tongue, common in most climate models. The cold tongue extends into the EIO, inducing an unrealistic relationship between the EIO SST and Australian rainfall (section 4).

## **4.2 Specific details of data, methodology, and model experiments**

It is increasingly recognized that anthropogenic climate change can project onto existing natural variability modes of the climate system (Clarke et al., 2001). Thus it is important to understand the dynamics of rainfall variability over NWA. To this end we employ available observational data and reanalysis described in Section 2.1.1. Seasonal

anomalies are constructed for each season into DJF, MAM, JJA, and SON, referenced to the respective seasonal average over 1951-2000.

EOF spatial patterns and time amplitude functions (see Chapter 2) are calculated to assess the variability pattern of both SST and rainfall. We use a covariance EOF, and the variance of the time amplitude function of an EOF sums to unity, leaving the variance of an EOF to be recorded in the spatial pattern. The inter-relationship between various circulation patterns is obtained by regressing/correlating grid-point anomalies of a field onto an index of a given pattern, for example, the time amplitude function of an EOF, or Niño3.4 (170°W-120°W, 5°S-5°N, an index of ENSO).

The linear projection method, described in Chapter 2, is also used to investigate the evolution of a given circulation pattern  $G(x,y)$  and the extent to which climate change signals project onto the given pattern. As discussed in Chapter 2 and Shi et al. (2008b), for a circulation field  $A(x,y,t)$ , this is carried out in the following way: for each given instant  $t_n$ , we regress  $A(x,y, t_n)$  onto  $G(x,y)$  to yield a pattern regression coefficient. When this is done for all  $t$ , a time series  $f(t)$  of the pattern regression coefficient is generated.

An objective of the present analysis is to examine if the rainfall trend produced in the CSIRO Mk3a model (see Chapter 2) forced with all climate change forcing, including increasing aerosols, is generated by the same processes as in the observations. As detailed in Rotstayn et al. (2007) and Shi et al. (2008b), these sets of simulations are run with a comprehensive aerosol scheme and cover the period 1871 to 2000. Specific details are provided in Section 2.1.2.

A multicentury (300 years) control experiment (without climate change forcing) is used to examine if the model reproduces the rainfall teleconnection with large scale circulation fields. Outputs from the ALL ensemble onto modes of variability in the control experiment are projected in the same way as for the observed. The result shows that the process by which the modeled rainfall increase is generated is rather different from that in the observed.

### **4.3 Observed characteristics of NWA rainfall**

#### **4.3.1 Seasonality of trends and variability**

Most of the annual-total rainfall over the NWA region is recorded in warm months, and is strongly influenced by the Australian summer monsoon. As such, summer rainfall is about ten times greater than that in the winter season (Fig. 4.2, left column). Although the trend over NWA shows up in the annual mean map, it is primarily a summertime (DJF) phenomenon (Fig. 4.2e, right column). The percentage (figure not shown) of increase is also substantial, reaching about 50% over most of NWA for DJF over the past 50 years. By contrast, a reduction occurs over most of eastern Australia in DJF. In other seasons, the trend over NWA is small in absolute terms.

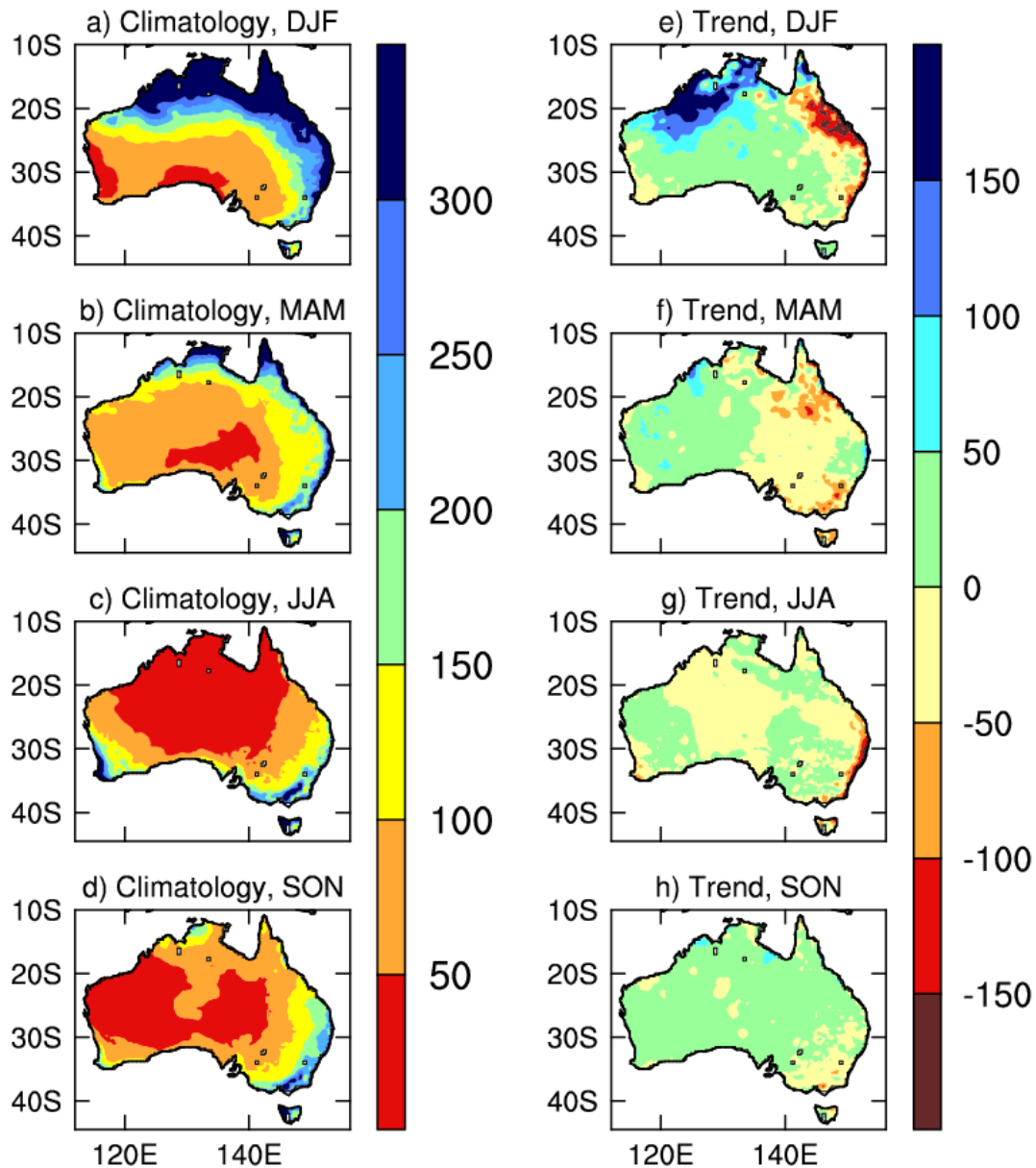
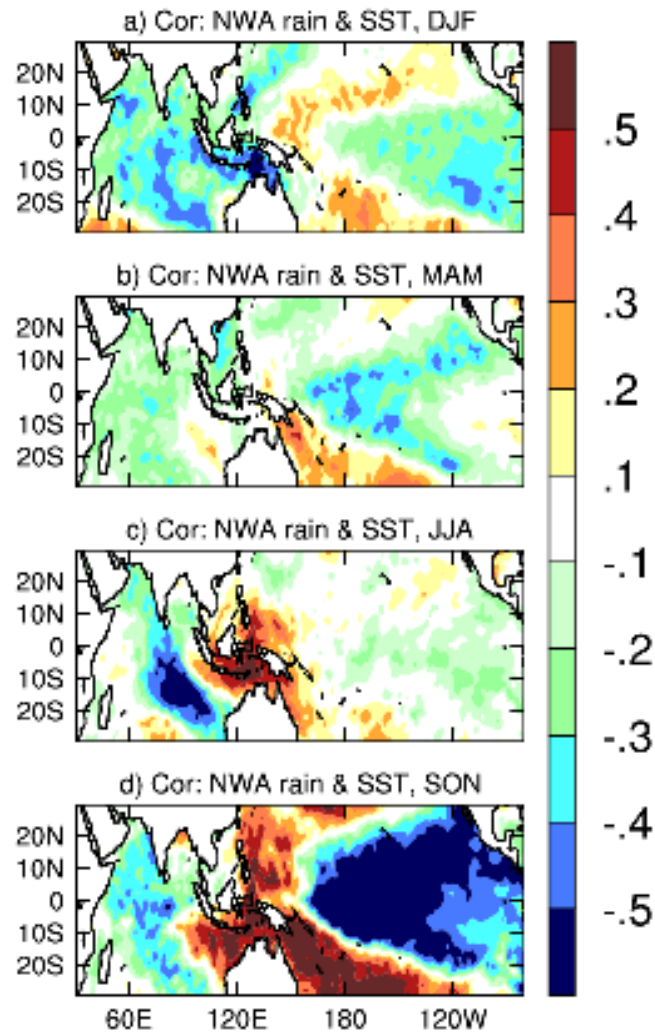


Figure 4.2: Observed climatology (left column) and trend (right column) of seasonal total rainfall (mm) over 1951-2000 (from Shi et al., 2008b). The data are stratified into December-January-February (DJF), March-April-May (MAM), June-July-August (JJA), and September-October-November (SON).

To understand the dynamics of the rainfall trend it is necessary to examine the forcing of rainfall variability as the response to a climate change forcing might project onto existing modes of variability. To this end we employ linearly detrended data. Rainfall variability over Australia is strongly region-specific as it can be predominately driven by one of the global-scale modes of variability, while simultaneously impacted by other modes. Further, the relative importance of these modes varies with seasons (Shi et al., 2008b).



*Figure 4.3: Map of correlation between NWA rainfall and grid-point SST (both linearly detrended) for each season using data for the 1951-2000 period (from Shi et al., 2008b). Correlation coefficients greater than 0.28 are significant at a 95% confidence level.*

Maps of correlation between the observed NWA rainfall (averaged over 110°E-135°E, 10°S-25°S – land points only) and grid-point global SST for each season are depicted in Fig. 4.3. In DJF (Fig. 4.3a), although the correlation pattern in the Pacific displays a La Niña-like pattern, most of the correlation coefficients have an absolute value of smaller than 0.27, a value required for a 95% level of confidence. Correlation of the NWA detrended rainfall time series with detrended Niño3.4 index records a coefficient of 0.29, marginally greater than the value for a 95% statistical significance level. The weak correlation is in agreement with the canonical Australian rainfall-ENSO relationship (e.g., Ropelewski and Halpert, 1987), which describes an influence mostly over eastern Australia. The correlation in the IO is generally greater than that in the Pacific. As already shown in Shi et al. (2008b), the overall pattern resembles that associated with a

La Niña phase. In particular, an east-west temperature gradient along 20°S is rather conspicuous with cooling occurring off the WA coast, and relative warming along the coast.

There is little significant correlation between NWA rainfall and SST (Fig. 4.3b) in MAM. The overall pattern shows a decaying La Niña in the Pacific, and westward propagating anomalies in the southern tropical IO. In JJA (Fig. 4.3c), the correlation strengthens with a well-defined correlation pattern similar to the map Nicholls (1989) obtained by correlating southeastern Australian rainfall with SST anomalies in the IO. Recent studies found that this pattern can evolve into an IOD – a coupled ocean-atmospheric phenomenon (Saji et al., 1999), which usually starts in JJA, peaks in SON, and end abruptly as December approaches. The IOD linkage to Australian cold season rainfall variations is found to consist of a broad band extending from the EIO to the northwest and southeast of the continent (e.g., Ashok et al., 2003, Cai et al., 2005d). This is simulated well by the model (Figs. 4.3c and 4.3d). Since 1950, some IOD events occur coherently with an ENSO event, as a result of their seasonal phase-locking properties (Yamagata et al., 2004), giving rise to the strong ENSO-like pattern in the Pacific (Fig. 4.3d), with the majority of correlations statistically significant at the 95% level.

The above analysis suggests a strong linkage of NWA JJA and SON rainfall with the IOD and ENSO, but the linkage is weak in DJF. In particular, warm IO SSTs in DJF are not associated with an increase in NWA rainfall (Fig. 4.3a). To further illustrate this, we correlate a time series of seasonal-mean Niño3.4 and EIO SST anomalies (averaged over 90°E-110°E, 5°S-15°S) with grid-point rainfall anomalies of the same season. The results are plotted in the left column of Fig. 4.4 (red colour indicating drier-than-normal conditions) for Niño3.4 and the right column for EIO SST.

In DJF (Fig. 4.4, left column) ENSO has a weak influence on NWA rainfall, with warmer SST in the equatorial eastern Pacific tending to reduce NWA rainfall. A sizable correlation exists in a strip extending from central northern Australia to the southeastern regions. In eastern Australia, a significant correlation is present; this is the well-known ENSO-eastern Australia rainfall teleconnection (McBride and Nicholls, 1983; Ropelewski and Halpert, 1987). In MAM, large correlations are seen in the central southern region. In JJA and SON, a positive Niño3.4 index is associated with decreasing rainfall over central eastern Australia.

EIO SST anomalies in DJF tend to affect rainfall over inland Australia (Fig. 4.4a, right column), warming EIO SSTs being associated with a decrease in rainfall; the pattern is reminiscent of that associated with Niño3.4, although the impact (Fig. 4.4a, left column) is not completely identical. The pattern which stretches from the central northern inland region to the southeastern inland regions re-emerges with stronger correlations. However, the impact over NWA is weak. If anything, an increase in the EIO SST trend is linked to a decrease in NWA rainfall.

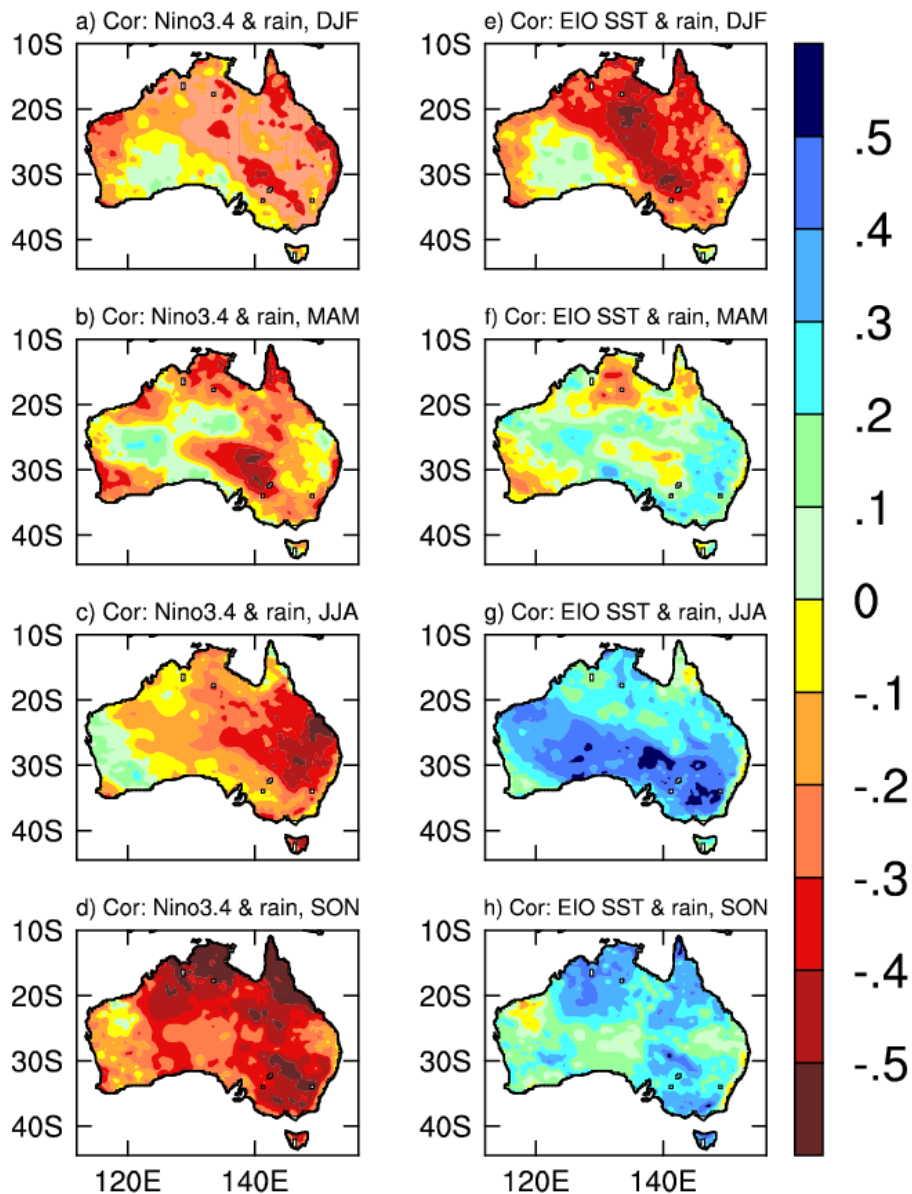


Figure 4.4: Maps of correlation of Australian rainfall with Niño3.4 (left column) and with EIO SST (right column) for each season using data for the 1951-2000 periods (from Shi et al., 2008b).

During the MAM season, the impact of the EIO SST on NWA rainfall tends to be opposite to that in DJF, but is rather weak. This is indicated by lower correlation coefficients. In the JJA and SON seasons (right column, Figs. 4.4g and 4.4h), increasing EIO SSTs are associated with rainfall increases in southern Australia (JJA) and parts of NWA (SON). Note that in SON the rainfall correlation pattern with EIO SSTs resembles

that associated with Niño3.4 but with opposing polarities in the correlation coefficients (Figs. 4.4d and 4.4h, left and right columns).

Thus, the significant correlation between NWA rainfall with known modes of global SST variability only occurs in the JJA and SON seasons, but in these two seasons, there is little rainfall trend. In DJF the correlation with either ENSO or IOD is weak.

### 4.3.2 Variability of DJF rainfall and Indo-Pacific SSTs

In this section, we focus on the DJF rainfall variability. To examine if there is a mode of DJF SST variability that dominates the NWA DJF rainfall, we carry out EOF analysis on detrended DJF SST anomalies in the tropical IO domain over the 1951-2000 periods. We conduct the analysis over this domain, as opposed to the whole Indo-Pacific region, because we are interested in the teleconnections influencing NWA rainfall through the tropical IO. As described in Shi et al. (2008b), the hypothesis of a forcing on NWA rainfall by increasing aerosols relies on an influence from the IO. The first mode (EOF1) accounts for 37.2% of the total variance and mainly describes variations associated with ENSO (Cai et al., 2005d), with warm anomalies occupying almost the entire IO basin. The correlation between the associated time series and Niño3.4 for the SST EOF1 in the tropical Indo-Pacific domain reaches as high as 0.89. The EOF1 is the well-known basin-scale pattern resulting from atmospheric teleconnection with the Pacific. For a comparison with the model ENSO in section 4, the anomaly patterns of wind and SST associated with El Niño are plotted in Fig. 4.5. An El Niño event generates easterly anomalies throughout much of the tropical (10°S -10°N) IO (Fig. 4.5), which superimpose on the climatological westerlies, giving rise to a warming and decreased evaporation. The opposite occurs during La Niña. The correlation between the EOF1 time series and rainfall resembles that associated with Niño3.4 (Fig. 4.4a, left column); an important point is that the correlation is rather weak over NWA.

The pattern of the second mode (EOF2), which accounts for 14.9% of the total variance, depicts positive anomalies extending northwest from the NWA coast into the IO. The map of correlation coefficients between the time series and Australian rainfall shows a general opposite polarity between east and west of 130°E, with correlations bordering on 95% statistical significance. We shall discuss the linkage of EOF2 with NWA rainfall later, when we describe NWA rainfall EOFs.

Thus there is no well-defined SST EOF mode that controls the NWA DJF rainfall variability, and the ENSO influence on NWA rainfall is weak. In any case, the trend of ENSO over 1951-2000 can not explain the observed DJF rainfall trend, because there is an upward trend in Niño3.4 over the 50-year period. According to the ENSO-NWA rainfall relationship shown in Fig. 4.4a (left column), i.e., an increase in rainfall is associated with a La Niña pattern; the upward trend in the Niño3.4 would mean a rainfall reduction rather than an increase. Indeed, removing the influence of ENSO results in an even stronger increasing rainfall trend. For these reasons we remove ENSO in our subsequent analysis. This is done by linearly regressing DJF rainfall anomalies onto Niño3.4. The associated anomalies are then removed.

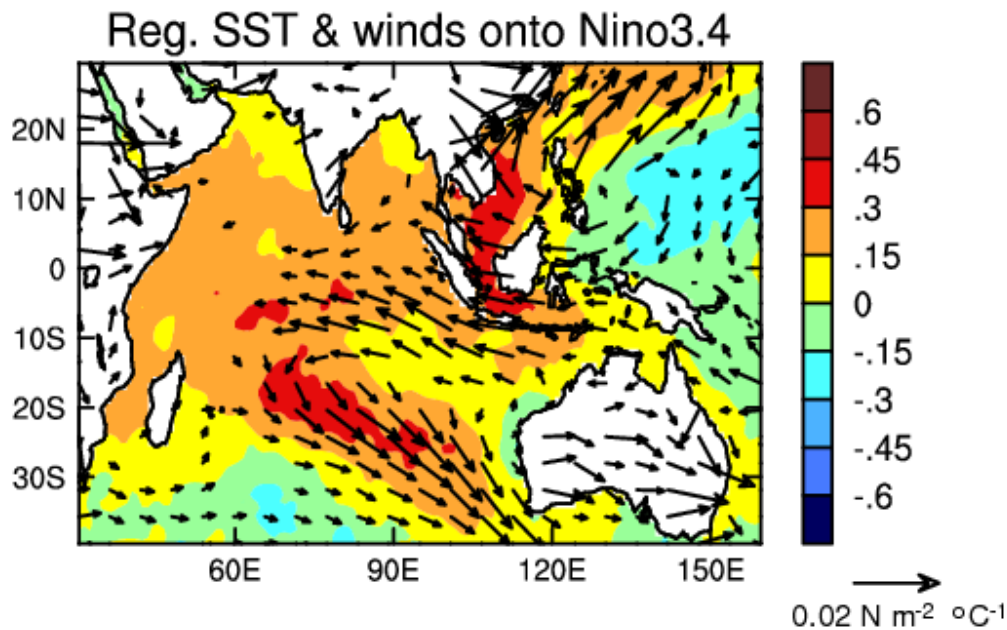


Figure 4.5: Patterns of SST (GISST, in  $^{\circ}\text{C } ^{\circ}\text{C}^{-1}$ ) and wind (NCEP, maximum vector  $0.02 \text{ N m}^{-2} ^{\circ}\text{C}^{-1}$ ) anomalies associated with ENSO. These are obtained by regressing linearly detrended SST and wind fields onto linearly detrended Niño3.4 (from Shi et al., 2008b).

An EOF analysis on the non-ENSO NWA rainfall anomalies in the domain of 110°E-135°E, 10°S-25°S is carried out. The EOF1 accounts for 47.2% of the total variance, and EOF2 accounts for 12.2% of the total variance (without ENSO). We focus on this limited region rather than Australia-wide because the trend is concentrated in this area. To find out the associated pan-Australia pattern, grid-point rainfall anomalies are regressed onto the associated time series, with the patterns depicted in Fig. 4.6. The EOF1 pattern reflects the northern-concentration of variance, with small anomalies south of 28°S. The EOF2 pattern (Fig. 4.6b) shows coherence between the regions east and west of 130°E, but of opposing polarities; to the east, anomalies are strongest north of 25°S, and to the west anomalies are largest in the area between 112°E-125°E, 18°S-26°S. As will be shown, the increasing rainfall trend over NWA is a result of the upward trends of these two modes. East of 130°E, the weights of EOF1 and EOF2 offset, giving rise to the spatial feature shown in Fig. 4.2e, as described in Shi et al. (2008b). When similar analysis is conducted with the presence of ENSO signals in rainfall, similar patterns emerge, supporting the small impact of ENSO on rainfall in the region. The correlation between the EOF1 time series and Niño3.4 is 0.28, and between the EOF2 time series and Niño3.4 is 0.02, virtually independent from ENSO.

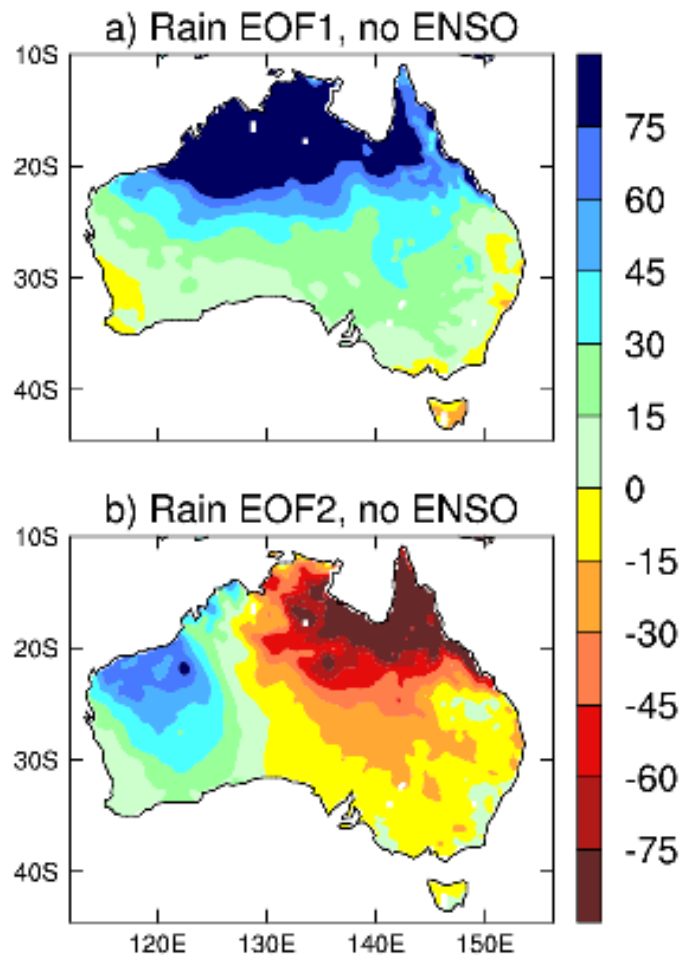


Figure 4.6: Patterns associated with detrended DJF rainfall EOF after removing variances associated with ENSO in the domain of  $110^{\circ}\text{E}$ - $135^{\circ}\text{E}$ ,  $10^{\circ}\text{S}$ - $25^{\circ}\text{S}$  (from Shi et al., 2008b). These patterns are obtained by regressing grid-point Australia rainfall anomalies onto the time series of the EOF1 and EOF2.

To obtain the SST pattern associated with the rainfall EOF without ENSO, grid-point SST anomalies are regressed onto the two EOF time series with the results shown in Fig. 4.7. The regression pattern for EOF1 (Fig. 4.7a) is somewhat similar to that associated with Niño3.4 (Fig. 4.5), taking into account of opposite signs. The associated anomalies are not spatially uniform, and encompass enhanced east-west gradients toward the NWA coast. Shi et al. (2008b) argue that it is the change of the SST gradient, not the SST *per se*, that generates NWA rainfall variability. Fig. 4.7a suggests that an increased zonal SST gradient toward the NWA coast is conducive to a rainfall increase over northern Australia. The SST pattern associated with EOF2 (Fig. 4.7b) indicates that warming anomalies off west and northwestern Australia promote rainfall over NWA west of  $130^{\circ}\text{E}$ , but are associated with a rainfall reduction east of this longitude.

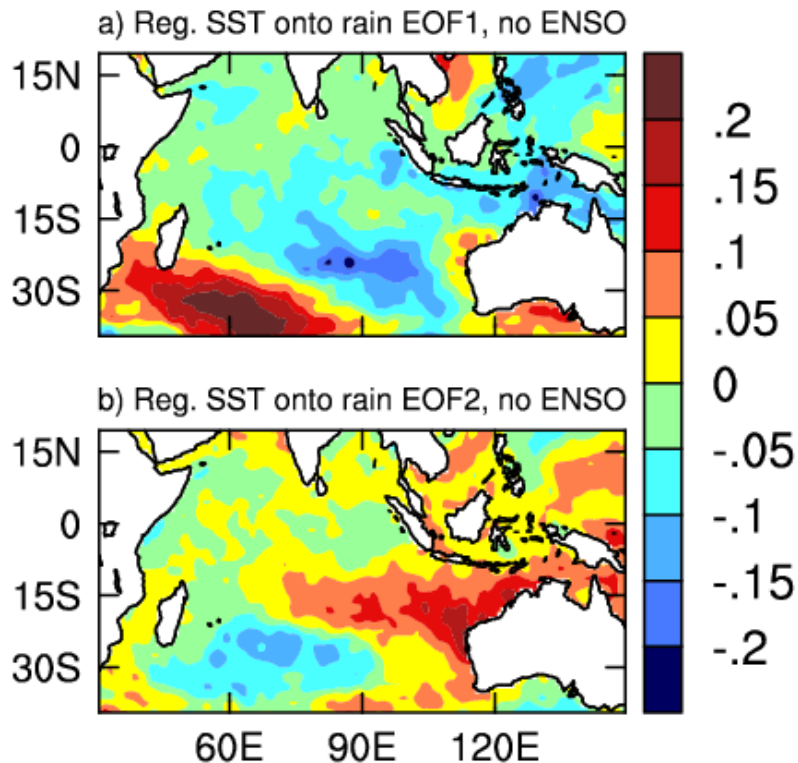


Figure 4.7: SST patterns associated with EOF1 and EOF2 shown in Fig. 6 (from Shi et al., 2008b). Shown are obtained by regressing SST anomalies onto the time series of the EOF1 and EOF2. Units are  $^{\circ}\text{C}$  per unit of the EOF time series.

The fact that the IO SST pattern associated with the rainfall EOF1 without ENSO resembles the pattern associated with ENSO, yet the associated rainfall is rather different (Fig. 4.4a vs. Fig. 4.6a) raises two important issues. First, patterns of SST variability independent of, but similar to that of ENSO can have a significant influence on NWA rainfall. Second, the influence on rainfall by this pattern is dependent on the equatorial Indo-Pacific SST anomaly structure. In the presence of a La Niña (Fig. 4.4a), the impact is vastly different from that without a La Niña (Fig. 4.6a). Further experiments using atmospheric models forced by prescribed SSTs are required to unravel the dynamics.

To further understand the dynamical processes of the two rainfall EOFs, NCEP MSLP, surface winds, and cloud cover anomalies are regressed onto the two rainfall EOF time series and plot the results in Figs. 4.8 and 4.9. Figure 4.8a indicates that the rainfall EOF1 is associated with a decreased MSLP bordering the northwest coast, with a cyclonic flow pattern consisting of northwesterlies blowing from the EIO ( $10^{\circ}\text{S}$ ) towards the NWA coast and northerlies toward northern Australia. These winds pick up the high moisture content from the tropical ocean, generating an increase in northern Australian rainfall. In association, cloud cover increases over NWA (Fig. 4.9a) and other northern Australia regions, consistent with the rainfall EOF1 pattern. In this season the climatological mean winds are westerlies, therefore the northwesterlies blowing from the

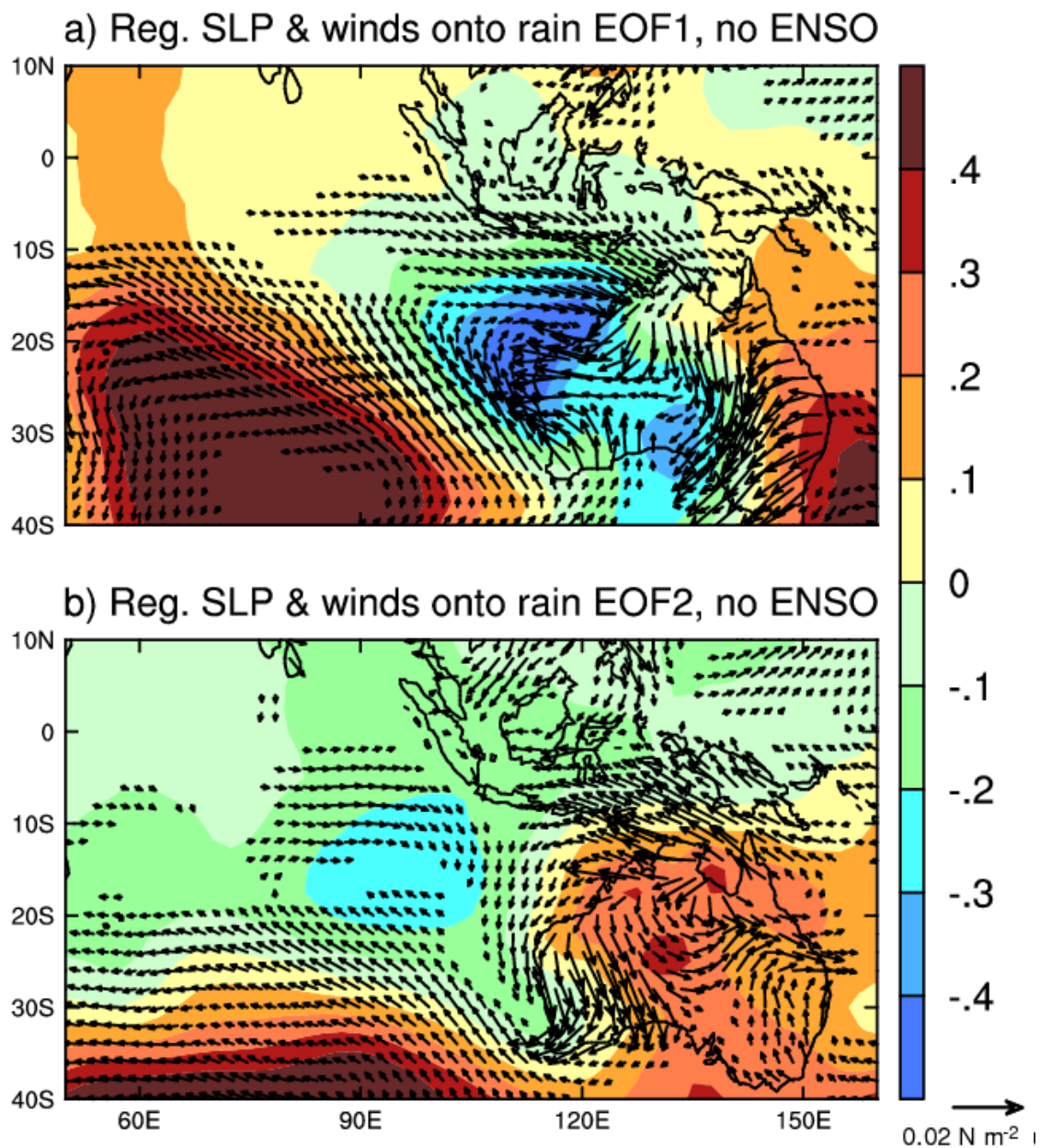


Figure 4.8: Anomaly patterns of MSLP (mb per unit of EOF time series) and winds ( $N m^{-2}$  per unit of EOF time series) associated with EOF1 and EOF2 shown in Fig.4.6 (from Shi et al., 2008b). Shown are obtained by regressing anomalies onto the rainfall time series of the EOF1 and EOF2. The regression coefficients of surface winds are plotted as vectors.

EIO at 10°S act to enhance the westerlies and evaporation (figure not shown), generating a cooling (Fig. 4.7a) in the tropical EIO. In this way, increasing rainfall over northern Australia is associated with anomalously low EIO SST. Other large scale features seen in Fig. 4.8a include strong southeasterly flows extending from the WA coast into the central southern subtropical IO, and the flows are supported by an anomalously high MSLP to

the west and near-coast low MSLP. As discussed previously, it is the gradient of SST that is important in moving tropical convection, rather than the absolute value of SST (indeed there are small anomalies along the NWA coast, Fig. 4.7a). The strong southeasterly flows in the subtropical IO are conducive to the cooling offshore seen in Fig. 4.7a; indirectly contributing to the enhancement of zonal SST gradients towards the NWA coast.

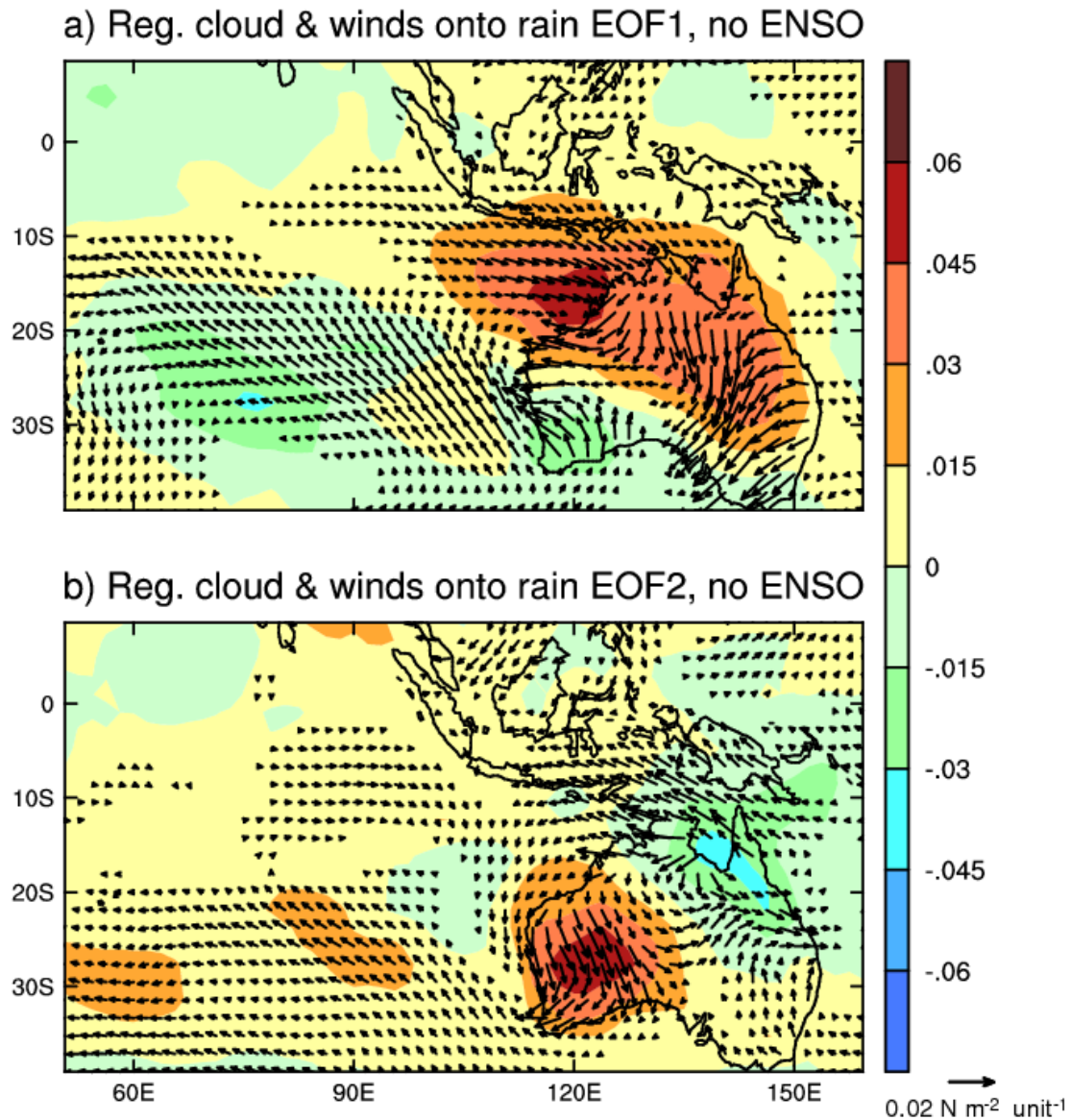


Figure 4.9: The same as Fig. 4.8, but for cloud cover (from Shi et al., 2008b).

The anomalous circulation associated with the rainfall EOF2, shown in Fig. 4.8b, is rather different. MSLP tends to be higher over the Australian continent. The associated flow pattern shows that, east of 130°E, northwesterly flows towards the tropical EIO are

generated, some veer eastward, and as part of an anticyclonic pattern, turn south along the WA coast, and pick up moisture over the ocean along the way. These high-moisture northerlies impinge on the NWA coast and contribute to the high rainfall west of the 130°E, whereas eastwards the flows are generally southwesterly over northeastern Australia. In this way, rainfall is high west of 130°E, and low to the east. The cloud cover pattern (Fig. 4.9b) shows an increase extending from subtropical EIO southeastwards to 130°E, however looking east decreased cloud cover is seen over northeastern Australia.

It will be shown in Section 4 that these two rainfall modes and the associated DJF circulation pattern are generally well reproduced by the CSIRO model. However, the model also generates an unrealistic circulation mode in this season.

### 4.3.3 Dynamics of the observed DJF rainfall changes

We have shown that the trend in ENSO over the past 50 years is unable to explain the DJF rainfall trend, and that there is no SST mode of variability in this season identifiable by the EOF analysis that dominates NWA rainfall variability. Can one understand the rainfall increase in terms of the two rainfall EOFs identified in section 3.2? To this end, we project DJF rainfall anomalies onto the EOF1 and EOF2 patterns following the procedure described in Section 2.2 (also Chapter 2 and Shi et al. (2008b)). Firstly, for each year, the raw DJF observed rainfall anomaly pattern is linearly regressed onto the DJF rain EOF1 pattern in the domain of 110°E-135°E, 10°S-25°S. This is conducted for 50 years from 1951-2000, and a time series of regression coefficients is generated, which shows an upward trend. Secondly, the total trend in the time series,  $\nabla f(t)$ , is calculated through linear trend analysis. Finally, the trend associated with EOF1 is obtained by multiplying the total trend in the time series  $\nabla f(t)$  with the EOF1 pattern (Fig. 4.6a). The result is plotted in Fig. 4.10a. A similar analysis is carried out for EOF2; the time series again displays an upward trend. The trend due to EOF2 is shown in Fig. 4.10b. The sum of EOF1 and EOF2 (Fig. 4.10c) produces an amplitude and a spatial shape of the trend that compares quite well with the total trend over NWA (Fig. 4.2e). The amplitude of the trend is larger than that shown in Fig. 4.2e in some places. Thus the DJF rainfall increase over NWA can be understood in terms of the upward trend of the two EOFs combined. This combination is significant because it generates the shape with a northeast-southwest orientation.

We have so far excluded the trend in ENSO. We now include this by regressing detrended rainfall onto the detrended Niño3.4 and then multiplying the regression pattern with the trend in the raw Niño3.4. When this is included, it does not change the overall trend pattern (Fig. 4.10d), consistent with the fact that the impact of ENSO is small. However, as the ENSO trend over the past 50-years serves to decrease NWA rainfall, the inclusion of the influence of an ENSO-like pattern further improves the agreement with the total trend (Fig. 4.2e). In fact, it is the ENSO-like pattern that is principally responsible for the decreasing rainfall trend over the coastal eastern Australia (Shi et al., 2008b).

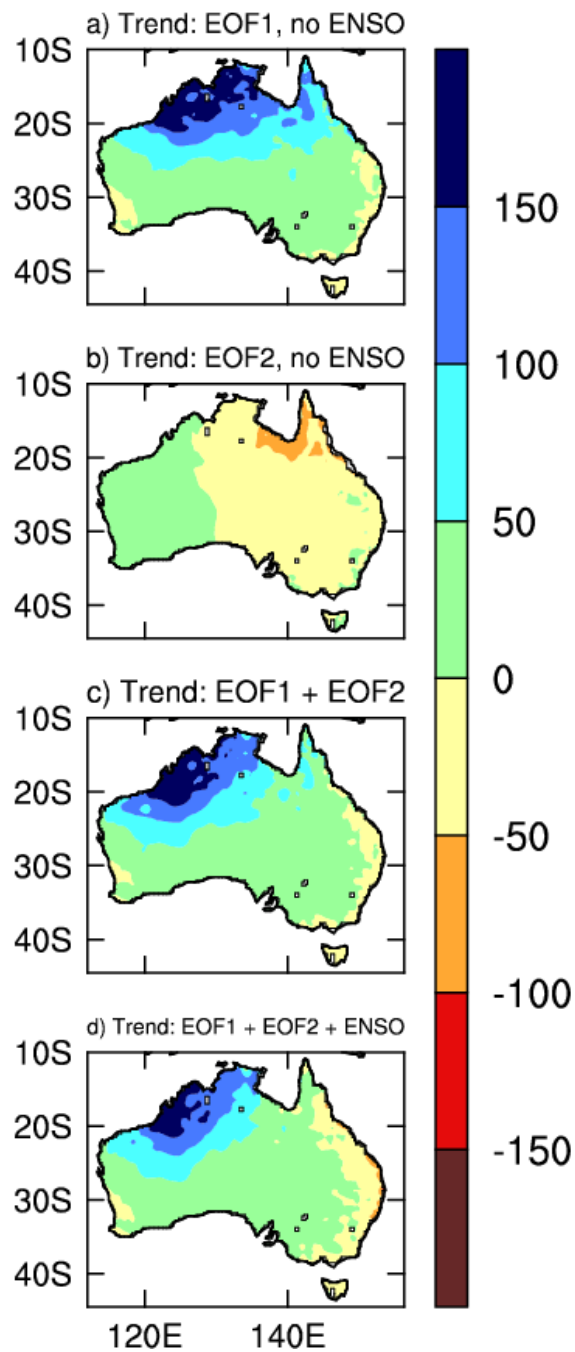


Figure 4.10: DJF total rainfall trends (mm) over 1951-2000 projected onto EOF1 (a) and EOF2 (b), and the sum of them (c) (from Shi et al., 2008b). Since these trends are obtained by projecting onto DJF rainfall with variance associated with ENSO removal, the ENSO-related trend is generated and added to (c) to yield (d).

A similar approach is deployed to calculate the trend in SST associated with the two rainfall EOFs. We regress undetrended SST anomalies onto the SST patterns shown in Fig. 4.7 for DJF of each year in the domain of 40°E-120°E, 40°S-40°N. A time series of the regression coefficient is obtained and the total trend is calculated. The trend maps for EOF1 and EOF2 are similar to those shown in Fig. 4.7. As in the rainfall trend, the associated SST trend is dominated by that associated with EOF1. The combined SST trend pattern is shown in Fig. 4.11a, and illustrates a strong zonal SST gradient toward the WA coast.

Thus over the past 50 years, ocean warming has projected onto the SST patterns associated with NWA rainfall variability encapsulated in the two rainfall EOFs (Shi et al., 2008b). This is further demonstrated by comparing the total trend obtained through linear regression of the raw SST anomalies (Fig. 4.11b). A pattern of greater warming along the WA coast, and hence a greater zonal SST gradient towards WA coast is produced. This gradient in Fig. 4.11a reaches about 0.4°C over 40° longitude (80°E to 120°E) and is comparable to that in the raw data (a spatially uniform value of 0.35°C is taken out in Fig. 4.11b). Sizable warming has occurred north of about 10°S, the dynamics of which is not clear, but in this season, this particular warming does not seem to contribute to a rainfall increase over NWA (Fig. 4.3a).

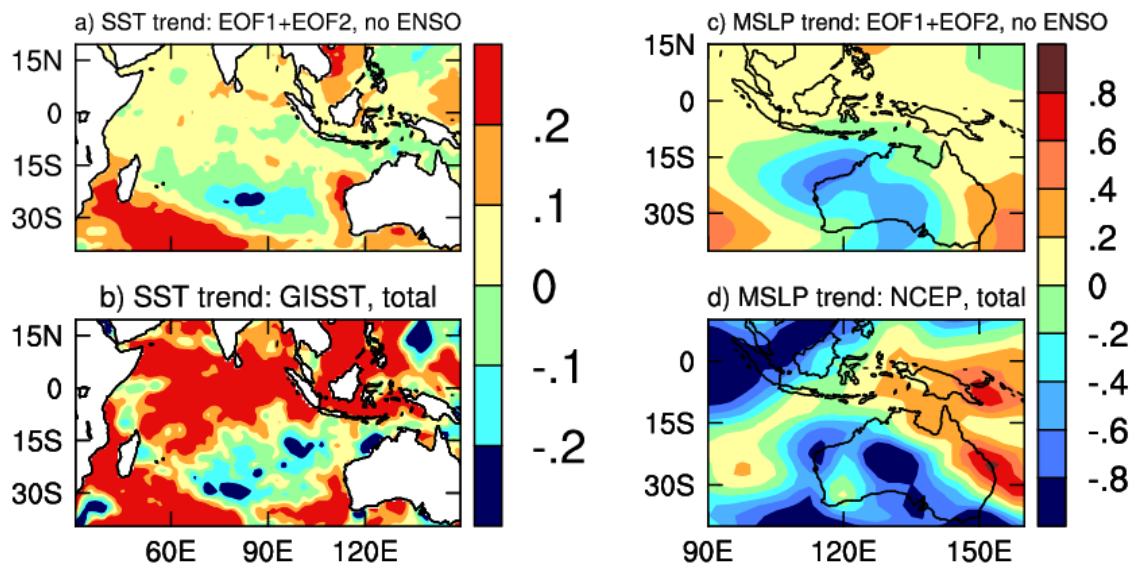


Figure 4.11: Panel a), SST trend ( $^{\circ}$ C) resulting from the sum of trends associated with DJF rainfall EOF1 and EOF2 of DJF rainfall shown in Fig.4.6. These trends are calculated by projecting raw DJF SST anomalies onto time series of the DJF rainfall EOFs (see text for details). Panel b), the total trend of raw SST. Panels c) and d), the same as a) and b) except for MSLP. A uniform value 0.35 $^{\circ}$ C is taken out from b) and a value of 1.4 mb is subtracted from d), respectively (from Shi et al., 2008b).

Similarly, we have projected MSLP anomalies on the MSLP patterns shown in Fig. 4.8. The total trend associated with the two rainfall EOFs is shown in Fig. 4.11c, to be compared with the total trend (Fig. 4.11d). Given that it is the pressure gradient that drives the wind, to facilitate a comparison, a uniform value 1.4 mb is subtracted everywhere. We see that these patterns are very similar supporting the notion that a climate change signal has projected onto existing modes of rainfall variability to generate the rainfall increasing trend.

Before we leave this section, a brief summary is in order. We have shown that in DJF there is no known SST variability mode that dominates the observed positive trend in NWA rainfall. Further, the El Niño-like trend pattern over the past 50-years acts to decrease the NWA rainfall, therefore it is unable to explain the observed increase. Instead we find that the rainfall increase is attributable to intensification in SST gradients towards the coast, west of 130°E. In what ensues, we examine the CSIRO climate model experiments described by Rotstayn et al. (2007) to see if the same process is responsible for an increase in NWA rainfall.

#### **4.4 Model rainfall variability and trend**

Before we proceed to discuss the model results, it is appropriate to note that the model is at a low-resolution and suffers from a common problem in the equatorial Pacific, which is too cold and extends too far into the western Pacific, and in this version of the model into the EIO (Shi et al., 2008b). In addition, the model ENSO is too weak; the standard deviation is about one third of the observed. The period is too long; the spectrum has the highest power on the 8-12 years, instead of the observed 3-7 years. We first described the trend averaged over the eight-experiments with all forcing including increasing aerosols (ALL, see Rotstayn et al., 2007). A 300-year long control experiment, i.e. without climate change forcing, is used to examine variability of NWA rainfall in ways similar to those conducted for the observed. Finally outputs from the ALL ensemble are used to examine if the rainfall trend is generated in the manner similar to that observed.

##### **4.4.1 Seasonality of trends and variability**

###### **4.4.1.1 Seasonal trends**

As in the observed, the model NWA rainfall mainly occurs in summer months with most of the annual total rain recorded in DJF; in fact, the DJF total rainfall is more than ten times as large as in the JJA total (Fig. 4.12, left column), and the climatological total compares well with the observed. In association, most of the rainfall increase takes place primarily in DJF (Fig. 4.12, right column). However the increase is much broader, including the eastern Australian region, inconsistent with the observed rainfall.

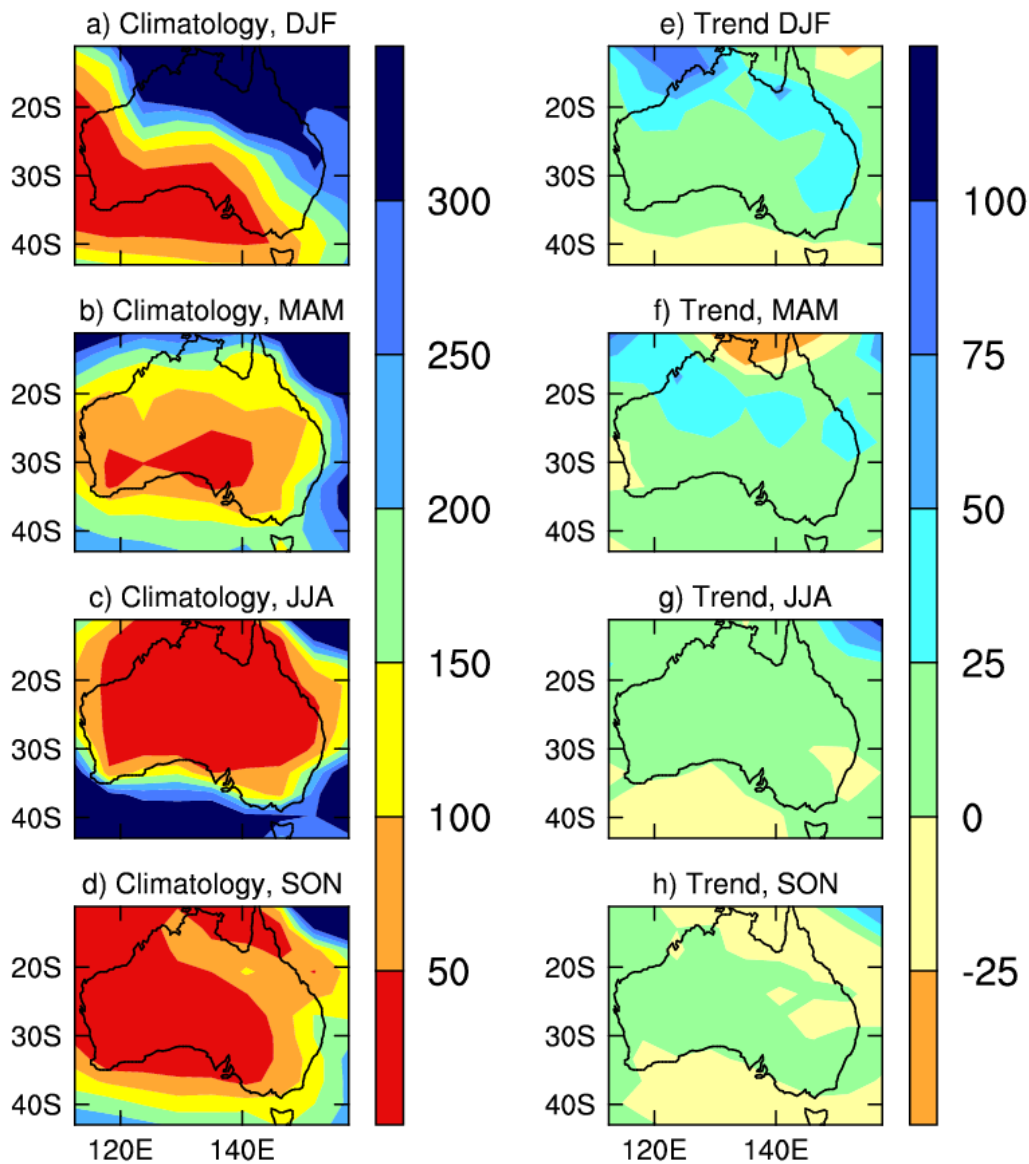


Figure 4.12: Model climatology (left column) from a 300-year control experiment of seasonal total rainfall (mm) and trend (right column) in seasonal total rainfall (mm) for 1951-2000. The data are stratified into December-January-February (DJF), March-April-May (MAM), June-July-August (JJA), and September-October-November (SON) (from Shi et al., 2008b).

We will try to understand the dynamics of rainfall variability using a multi-century control experiment. In this experiment there is virtually no trend, so detrending analysis is not required. The anomalies are constructed with reference to the mean over the 300 years.

#### 4.4.1.2 Seasonal correlation between NWA rainfall and global SST

Maps of correlations between model NWA rainfall and grid-point SST anomalies as in the observed (compared with Fig. 4.3 for the observed) are plotted in Fig. 3.13. For the DJF season (Fig. 4.13a), the correlation pattern in the Pacific shows a model La Niña-like pattern. Unlike the observed, most of the correlation coefficients have an absolute value greater than 0.12, a threshold required for a 95% level of statistical significance. In particular, the correlation with the eastern Pacific is high, generally greater than 0.4. The high correlation suggests that the model NWA rainfall is overly influenced by the model ENSO, a feature that is unrealistic. As discussed in Shi et al. (2008b), this is a consequence of the cold tongue problem, which extends into the equatorial EIO, where the correlation pattern shows a negative phase of an IOD-like pattern. The warm anomalies in the EIO then contribute to an anomalously high rainfall over NWA. Such an IOD-like pattern in DJF does not exist in the observations (Fig. 4.3a). The correlation pattern for MAM (Fig. 4.13b) is to that in DJF. Again the correlations with SST in the equatorial Pacific and the EIO are unrealistically too strong. In the JJA and SON seasons (Figs. 4.13c and 4.13d), the correlation patterns in the IO resemble the observed and reflect basically the IOD-like variation pattern.

Overall, several major differences between the model and the observed emerge. Firstly, in the observed, the IOD pattern only appears in JJA and SON, whereas in the model, an IOD pattern operates in all seasons. Secondly, in DJF the observed NWA rainfall is weakly correlated with ENSO, whereas in the model, correlation with ENSO is far greater. Finally, in SON, the correlation of NWA rainfall with equatorial Pacific SST is weaker than that in the observed.

The model IOD-like variability pattern in DJF and MAM (Figs. 4.13a and Fig. 4.13b) is rather unrealistic. In reality, development of the IOD (with cold anomalies off the Sumatra–Java coast) occurs only in JJA and SON (Rao et al., 2002). Because the climatological mean winds in the EIO are easterly south of the equator during JJA, the thermocline is located at a shallower depth. The El Niño-generated easterlies increase the wind speed and the latent and sensible heat fluxes. Increased upwelling and stronger latent and sensible heat fluxes overcome the increased shortwave radiation associated with reduced rainfall, leading to the development of a cold pool. The demise of the IOD typically takes place in December after the Australian summer monsoon commences, when the mean winds become westerly in the equatorial EIO, and the thermocline is deepened so that there is little thermocline-SST coupling. The induced easterly anomalies then reduce the wind speed. The associated reduced latent heat flux and increased surface shortwave radiation act together to warm the IO, yielding a basin-scale warm anomaly (e.g., Klein et al., 1999).

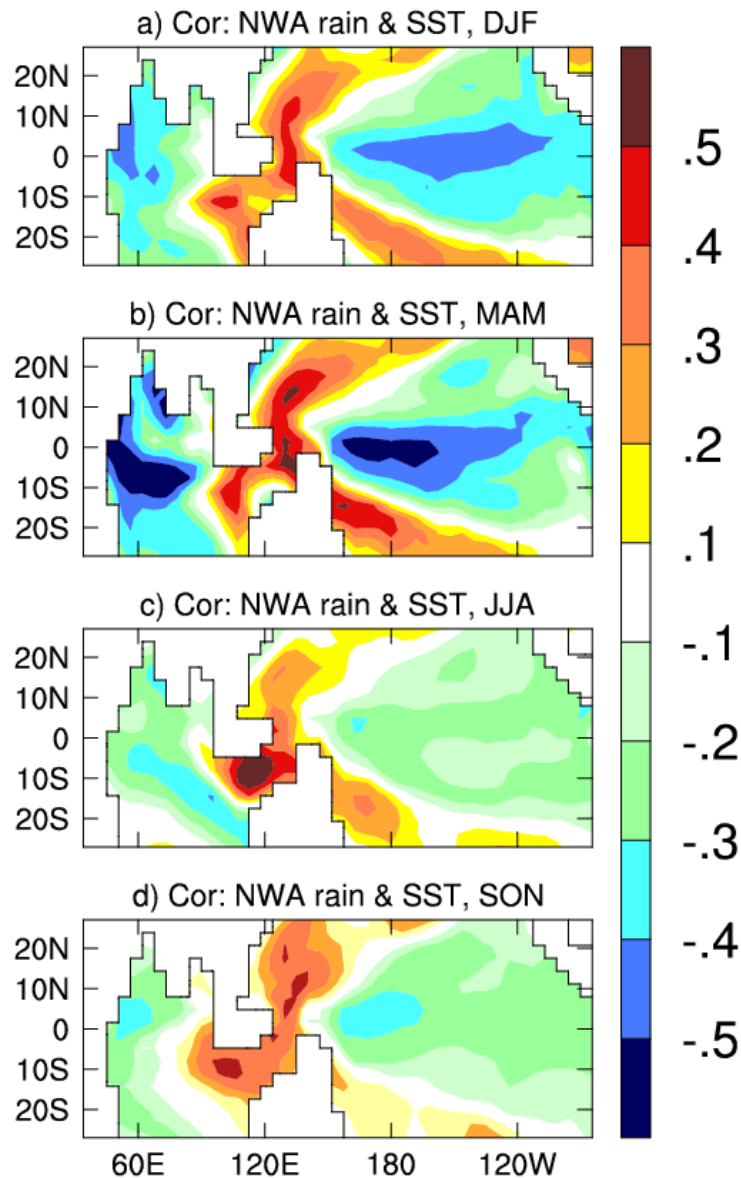


Figure 4.13: Map of correlation between modeled NWA rainfall and model grid-point SST (both linearly detrended) for each season using outputs from a 300-year control experiment. Correlation coefficients greater than 0.12 are significant at a 95% confidence level (Shi et al., 2008b).

It is apparent that the IOD-like variability pattern is a consequence of the model cold tongue that extends too far west, and in this version of the model, into the Sumatra-Java coast. As a consequence, the Sumatra-Java coast constitutes a part of the western Pacific warm pool and the climatological mean center of convection is situated too far west. This center moves eastward and westward with the model ENSO cycle. This is why the ENSO-Australian rainfall teleconnection has the strongest impact in NWA but not eastern Australia in the model (Fig. 4.13a) (Shi et al., 2008b); this is also why the IOD-

like pattern in the IO is strongest in DJF. Westward from the warm pool, easterlies superimpose on climatological westerlies to generate general warming as in the observed. Further, there is also a part of the east-west movement of the warm pool that occurs independent of ENSO, and this is reflected in a mode of IOD-like variability after removing the ENSO signals. The main point is that this unrealistic cold tongue structure creates a spurious relationship between SST in the EIO and NWA in DJF, in which an EIO SST increase is associated with an increase in NWA rainfall, a relationship not operating in the observed.

#### **4.4.1.3 Seasonal relationship of NWA rainfall with EIO SST and Niño3.4.**

The unrealistic feature seen above re-emerges in the ENSO-Australian rainfall relationship (Fig. 4.14, left column). The unrealistically strong ENSO influence over NWA rainfall is accompanied by a lack of an ENSO signal over eastern Australian rainfall (Fig. 4.14, left column). This is in agreement with the feature of a modeled Pacific warm pool being situated too far west and into the EIO. In MAM the correlation pattern with ENSO improves over the eastern and southeastern regions, however over NWA, it is far too strong. While the pattern in JJA resembles the observed; that in SON the model completely misses the teleconnection over northern Australia.

The EIO SST-Australian rainfall relationship (Fig. 4.14, right column) in DJF and MAM is virtually the mirror image of that associated with ENSO, suggesting a tight linkage between Niño3.4 and EIO SST in these two seasons, and again reflecting the feature that the EIO is a part of the Pacific warm pool. Similarly, the correlation pattern in JJA compares well with the observed, but in SON the EIO SST influence on northern Australia is underestimated. Most relevant to the present study is that in DJF, in which the model generates a rainfall increasing trend as in the observed, the model produces a spurious teleconnection in which NWA rainfall is unrealistically influenced by model ENSO. Therefore, an increasing EIO SST is associated with an increase in NWA rainfall in DJF, opposite to that seen in the observed (Figs. 4.4e and 4.14e).

### **4.4.2 Variability of DJF rainfall**

#### **4.4.2.1 EOF of DJF SST in the IO**

As discussed in section 3.2 and in Shi et al. (2008b), there is no observed mode of DJF SST variability in the IO that dominates the NWA DJF rainfall. By contrast, in the model, there is, i.e., the model ENSO and the associated SST in the EIO are a part of the unrealistic model warm pool (Fig. 4.13a). In fact, EOF analysis on IO SST anomalies in all seasons generates an IOD-like variability pattern, and in DJF the pole in the EIO has the largest variance. Correlation between the time series of the DJF SST EOF1 and Australian rainfall yields a pattern virtually identical to that shown in Fig. 4.14a. The second EOF of DJF SSTs resembles the observed second EOF with a pattern reminiscent of that shown in Fig. 4.7b. We will discuss this later.

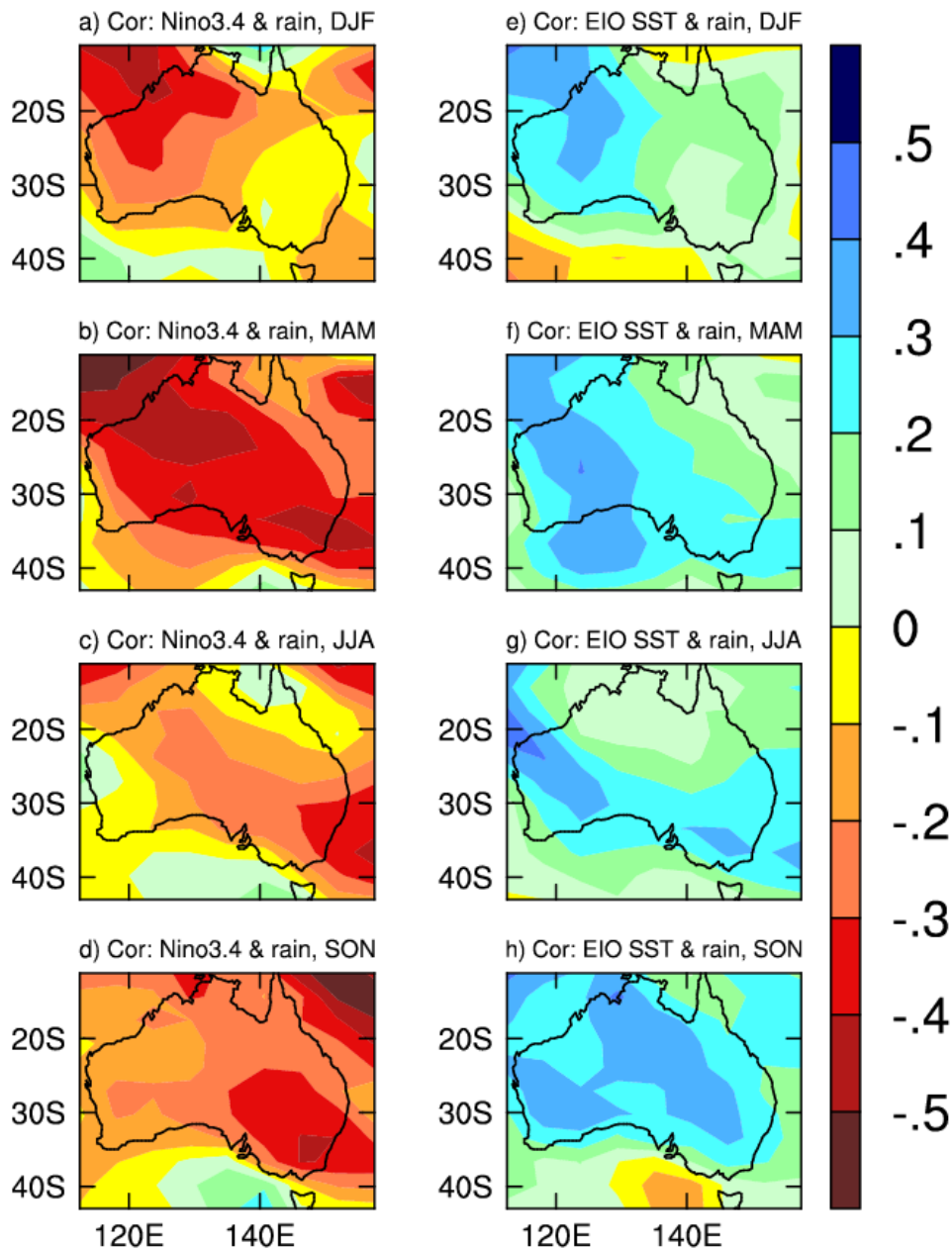


Figure 4.14: Maps of correlation of Australian rainfall with Niño3.4 (left column) and with EIO SST (right column) for each season using outputs from a 300-year control experiment model outputs (from Shi et al., 2008b).

To further highlight the unrealistic model ENSO feature, Fig. 4.15 plots the pattern obtained from regressing SST and surface wind onto a model Niño3.4 index. Compared with the observed (Fig. 4.5), there is an overall westward shift of the western Pacific anomalies in the model; the model easterlies extend too far into the western IO. In association, east of 110°E along the Sumatra-Java coast, the model shows westerlies that

extend to the western Pacific rather than the observed easterly anomalies. More importantly, there is strong cooling off the Sumatra-Java coast as the warm pool shifts eastward, and the variability pattern is IOD-like in the IO domain.

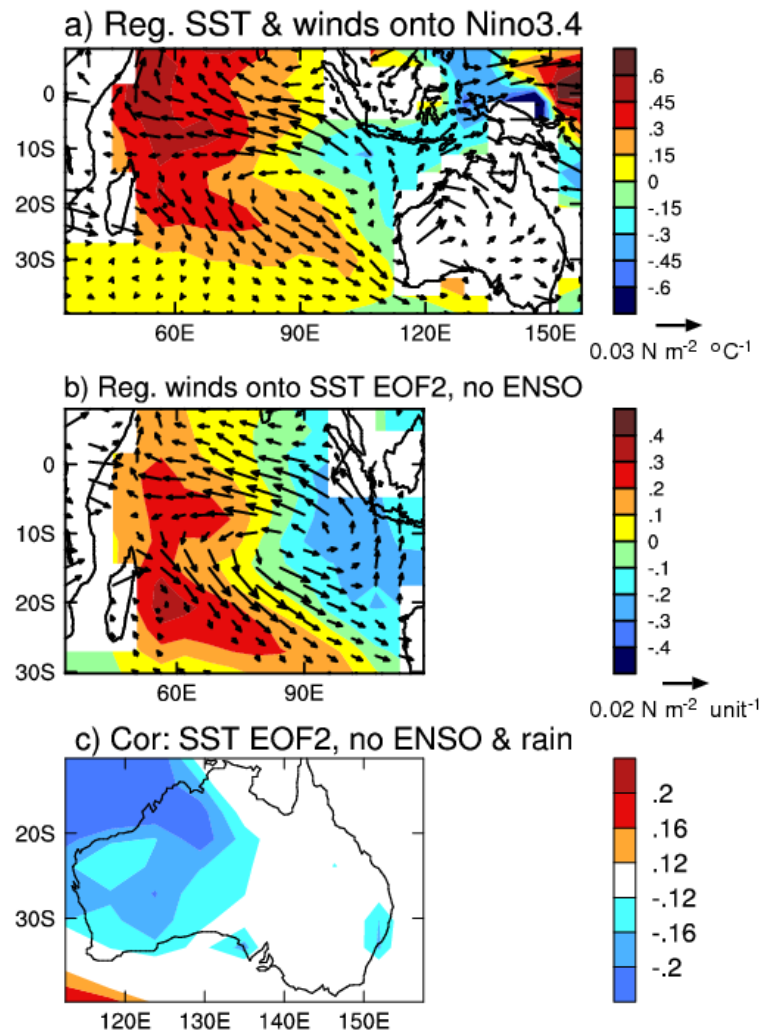


Figure 4.15: Panel a), pattern of model SST ( $^{\circ}\text{C } ^{\circ}\text{C}^{-1}$ , contour) and wind ( $\text{N m}^{-2} \text{ } ^{\circ}\text{C}^{-1}$ , vectors) anomalies associated with model ENSO-like variability (from Shi et al., 2008b). These are obtained by regressing model SST and wind anomalies onto the model Niño3.4 index in the 300-year control experiment. Panel b), EOF2 (16.8% of the remaining variance) of model SST and the associated model wind fields (vectors) after removing variance associated with ENSO-like variability, and c), correlation between time series of model EOF2 shown in b) and model rainfall.

It happens that after removing the model ENSO, there is an IOD-like mode that operates in DJF. This is realized by conducting EOF analysis on the residual after removing anomalies associated with model Niño3.4, in the tropical IO domain. This mode has an

anomaly pattern (Fig. 4.15b) that resembles what is shown in Fig. 4.15a for the IO. This is associated with the movements of the warm pool that is independent from ENSO. This is another unrealistic feature of the model. This mode also has a sizeable correlation with NWA rainfall in the DJF season (Fig. 4.15c). Indeed a strong correlation is achieved over NWA, significant at 95% confidence level.

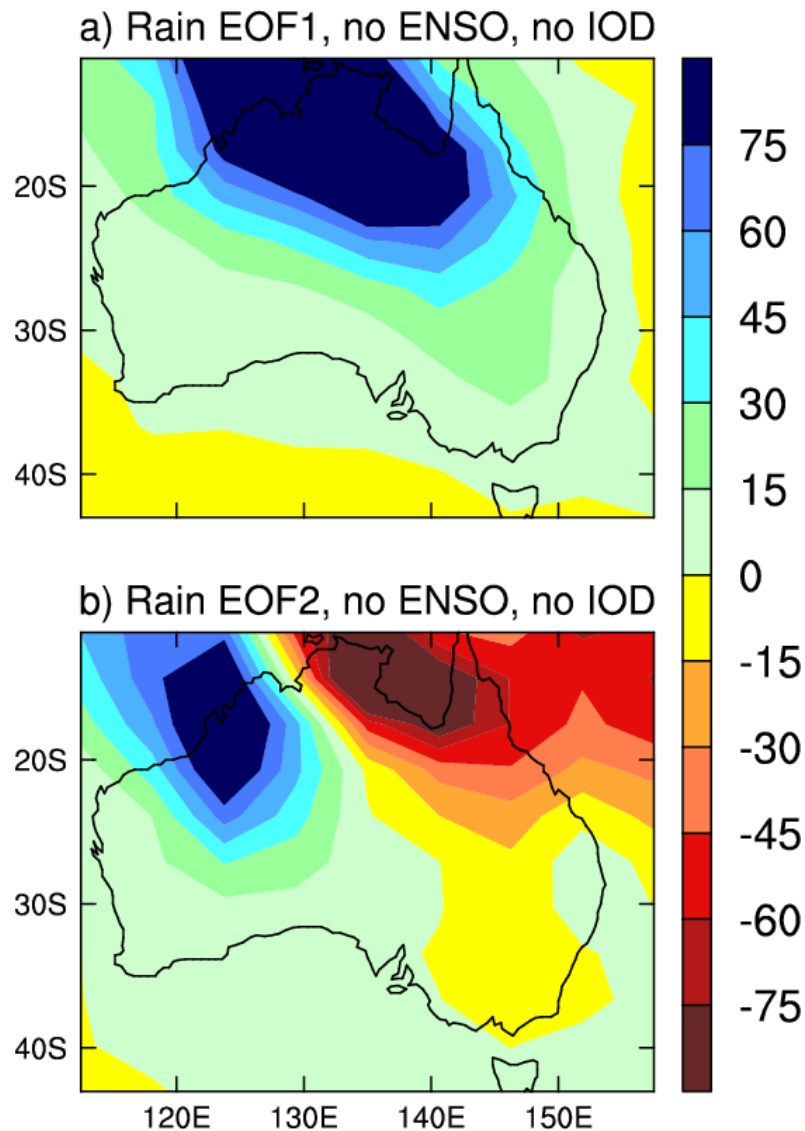


Figure 4.16: Patterns of model rainfall EOF after removing variances associated with ENSO and IOD (see text for details) (from Shi et al., 2008b). Patterns are obtained by regressing rainfall anomalies onto the time series of the model EOF1 and EOF2 in the domain of 110°E-135°E, 10°S-25°S. EOFs 1 and 2 account for 47.6% and 20.7% of the remaining variance.

#### 4.4.2.2 Rainfall EOF in DJF in the absence of ENSO and IOD

Given that only about one quarter of the NWA rainfall variance is explained by the model ENSO and that only a small portion (about 5%) is associated with IOD-like variability independent from ENSO, it is appropriate to examine the process that generates the remaining variation. To this end, we remove the variance associated with ENSO (Fig. 4.15a) and IOD (Fig. 4.15b) and apply EOF analysis to the residual rainfall following the procedure described in section 3.2. EOF1 (Fig. 4.16a), which accounts for 47.6% of the remaining variance, is similar to the observed EOF1 (Fig. 4.6a), and reflects a feature of a northern-concentration of variance, with little anomalies south of 28°S. EOF2 (Fig. 4.16b), which generally resembles the observed rainfall EOF2 (Fig. 4.6b), shows coherence between east and west of 130°E; the east has strong anomalies in the north, and the west shows strong anomalies between 112°E-125°E, 18°S-26°S. Thus even though the model produces several unrealistic features, it still captures important features of NWA rainfall variability.

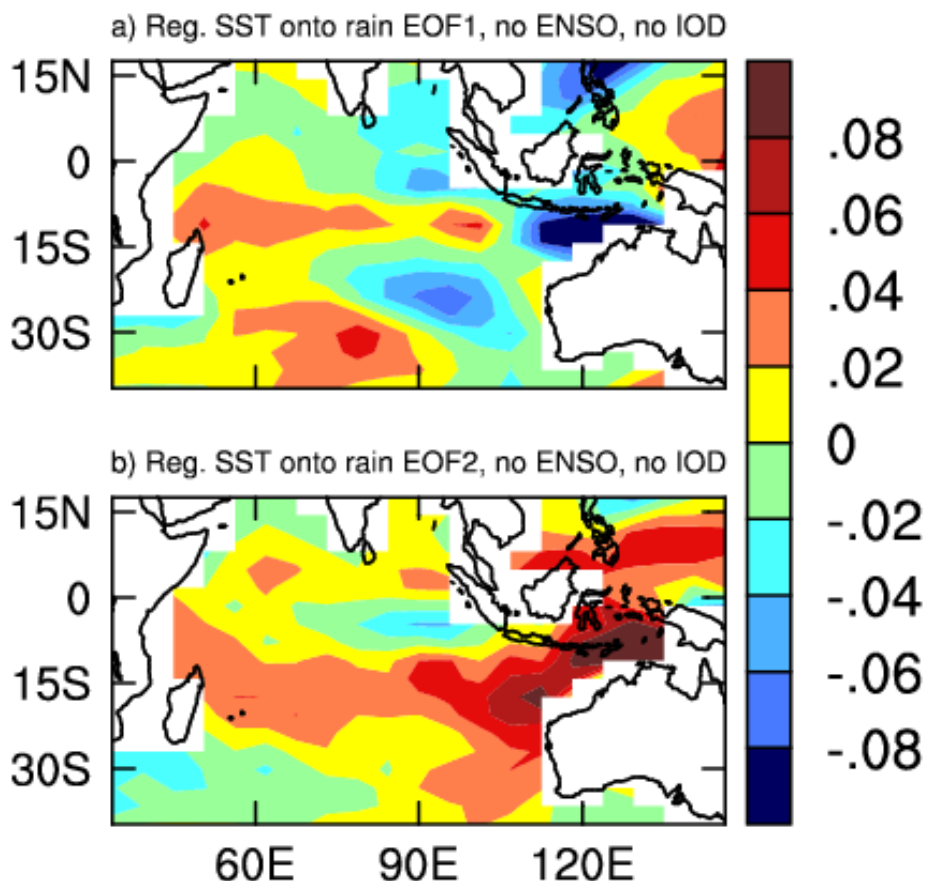


Figure 4.17: SST patterns associated with model rainfall EOF1 and EOF2 shown in Fig. 16. Patterns are obtained by regressing model SST anomalies onto the time series of the EOF1 and EOF2. (from Shi et al., 2008b).

#### **4.4.2.3 Circulation associated with DJF rainfall EOFs**

To obtain the SST pattern associated with the rainfall EOF shown in Fig. 4.16, we regress grid-point SST anomalies onto the two EOF time series (Fig. 4.17). The regression pattern for EOF1 (Fig. 4.17a) is generally similar to that associated with the observed rainfall EOF1 without ENSO (Fig. 4.7a) in terms of enhanced east-west SST gradients towards the WA coast, although the location of maximum anomalies is somewhat different. The SST anomaly pattern associated with EOF2 (Fig. 4.17b) is also similar to that shown in Fig. 4.7b with warming anomalies near NWA.

The circulation pattern in terms of MSLP, surface winds, and cloud cover are similarly obtained (Figs. 4.18a and 4.18b, and Figs. 4.19a and 4.19b). Despite the model's absence in the model of a strong subtropical high pressure anomaly center, which is rather prominent in the observed (Fig. 4.8a), the results generally support the notion that similar dynamical processes operate in the model. Associated with the rainfall EOF1 is a cyclonic flow pattern centered off NWA with northerlies advecting high moisture air mass to northern Australia (Fig. 4.18a), contributing to the high rainfall, with consistently higher cloud cover (Fig. 4.19a). By contrast, an anticyclonic pattern is associated with EOF2, with anomalously high MSLP over Australia with northwesterlies west of 130°E picking up moist air before impinging on the WA coast; east of 130°E, there are southerly anomalies to the north and decreased cloud. Thus it seems that, except for the unrealistic ENSO and IOD-like patterns and the associated unrealistic rainfall teleconnection, the model does realistically capture the dynamical mechanisms as revealed in the observations.

However, these two modes appear to be weaker than the observed. Comparing Figs. 4.18 and 4.19 with Figs 4.7 and 4.8, we see that the model anomalies are approximately half of observed; similarly, the model MSLP and wind stress anomalies are also much weaker.

#### **4.4.3 Dynamics of DJF model rainfall trend with increasing aerosols**

How much is the model DJF rainfall increase (Fig. 4.12a) projected onto the DJF rainfall EOFs 1 and 2 (Figs. 4.16a and 4.16b) and onto ENSO-like pattern (Fig. 4.15)? We project raw DJF rainfall outputs from the ALL ensemble onto the two EOF patterns for each year from 1951 to 2000. A time series of pattern regressions for each mode is obtained and the trend is calculated. Multiplying the total trend in the time series with the EOF patterns gives the trend associated with EOF1 and EOF2. We find that there is little trend embedded in the two EOFs; their sum accounts for less than 10% of the total trend.

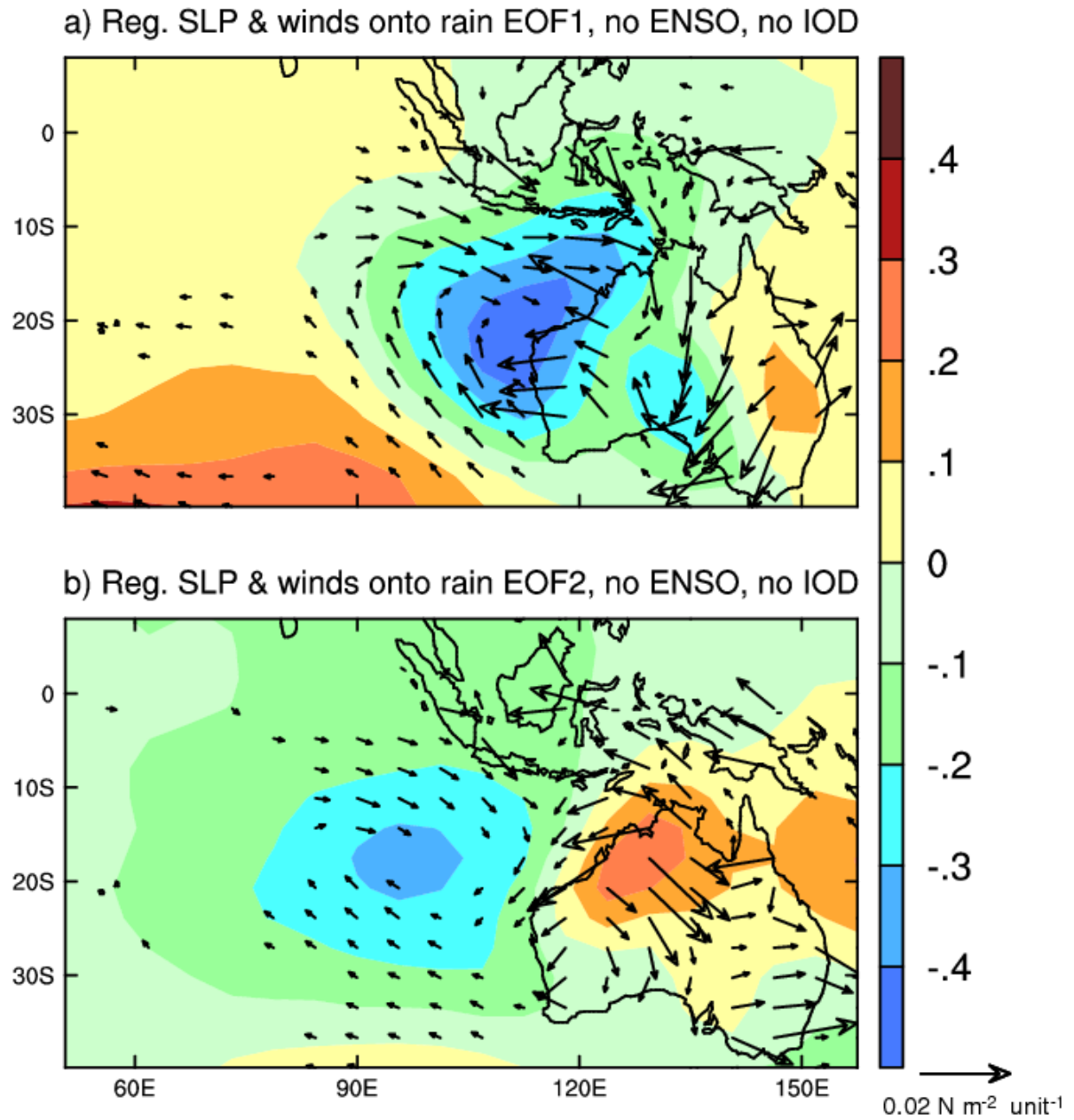


Figure 4.18: Anomaly patterns of MSLP (mb per unit of EOF time series) and winds ( $N m^{-2}$  per unit of EOF time series) associated with DJF rainfall EOF1 and EOF2 in the 300-year control experiment. Patterns are obtained by regressing model MSLP anomalies onto the time series of the rainfall EOFs (from Shi et al., 2008b).

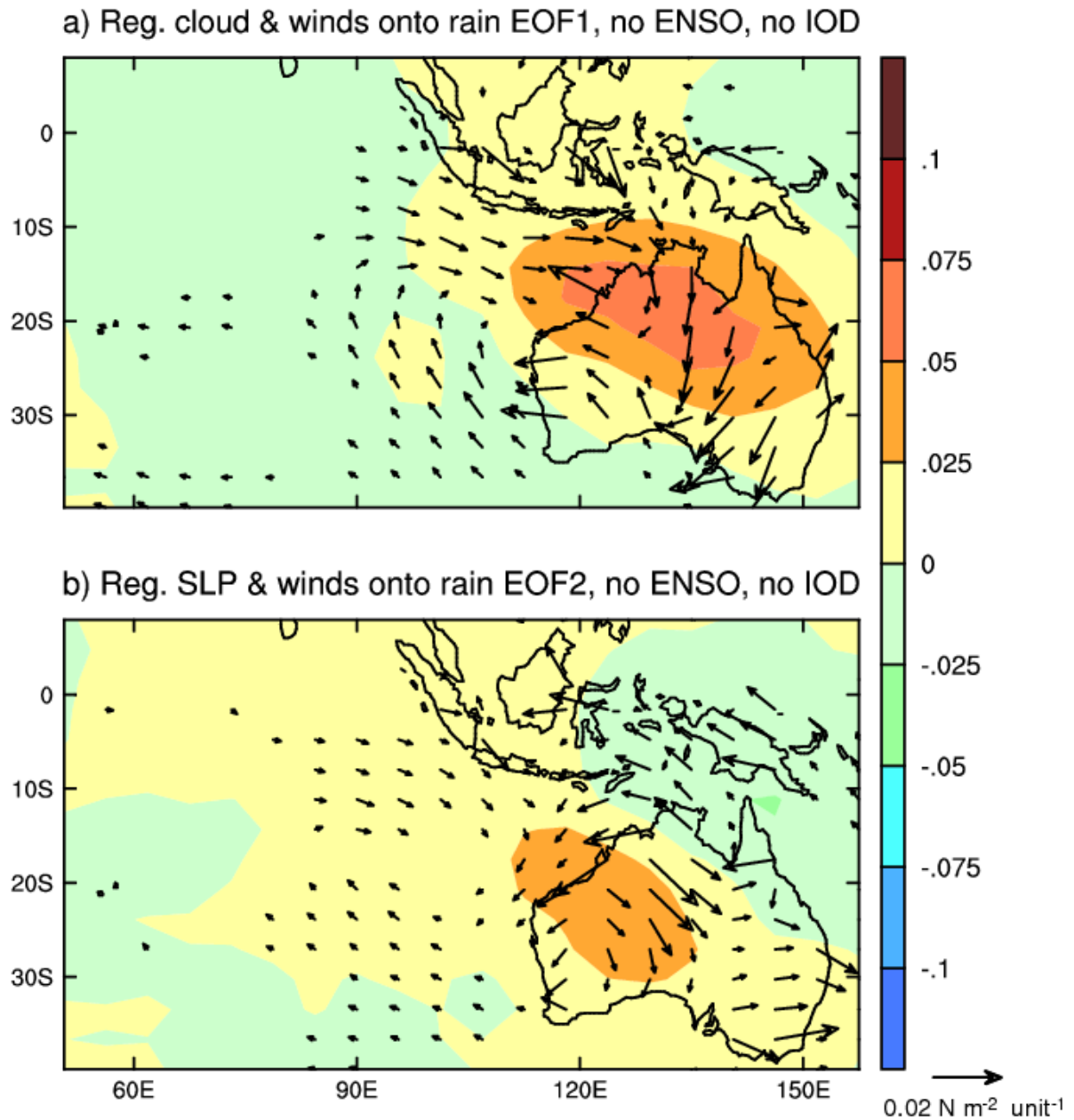


Figure 4.19: As in Figure 4.18, but for the cloud cover (from Shi et al., 2008b).

Similarly, we project SST outputs from the ALL ensemble onto the model ENSO pattern (Fig. 4.15) to obtain a time series of pattern regression coefficients, from which the total trend is obtained. Separately, we regress the control DJF rainfall onto the control Niño3.4 to obtain a regression pattern, which describes how rainfall varies with ENSO. The pattern is similar to that shown in Fig. 4.12a. Multiplying the total trend in the time series with the regression pattern gives the trend map associated with ENSO. We find that the increasing rainfall trend in this set of experiments is not associated with an ENSO-like trend pattern.

Most of the rainfall trend is attributable to the unrealistic teleconnection of NWA rainfall with the EIO SST in this season, embedded in the control run, as shown in Fig. 4.14e. Regressing grid-point DJF rainfall anomalies onto the time series of DJF SST in the EIO (90°E-110°E, 5°S-15°S) in the control run yields a map of a regression pattern,  $G(x,y)_{control}$ , similar to that shown in Fig. 4.14e describing the relationship between Australian rainfall and the EIO SST. In the presence of the aerosol forcing, there is an increase in the EIO SST incorporated in an IOD-like trend pattern (Fig. 4.20). There are indeed increased SST gradients toward WA, but they are weaker than the observed (Fig. 4.21). More importantly, the pattern is overwhelmed by the large increase in SST off the Sumatra-Java coast. The trend of a time series of DJF SST over the EIO box in the ALL ensemble,  $\nabla f(t)_{All}$ , is calculated, multiplying  $\nabla f(t)_{All}$  with the regression pattern  $G(x,y)_{control}$  generates a total trend that is due to the unrealistic model relationship of EIO SST with Australian rainfall (Fig. 4.20). Comparing with Fig. 4.12e, we see a good agreement, supporting that most of the DJF rainfall increasing trend in the ALL ensemble is caused by the unrealistic teleconnection in the model.

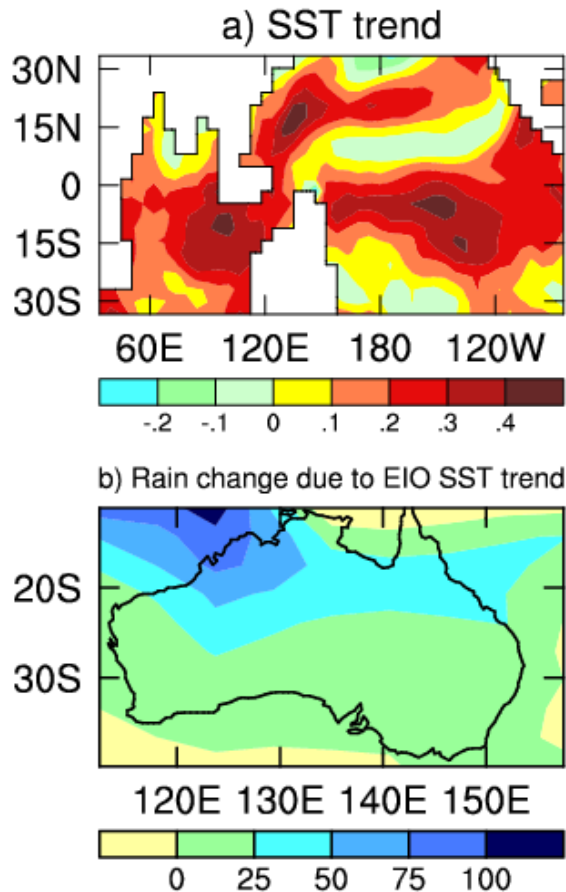


Figure 4.20: Panel a), Model DJF SST trend pattern ( $^{\circ}C$ ) with all forcing imposed (ALL ensemble). Panel b), total trend (mm) of the DJF rainfall estimated from the unrealistic relationship between EIO SST and Australian rainfall in the 300-year control experiment (from Shi et al., 2008b).

The process that leads to the increase in the EIO SST has been explored in Rotstayn et al. (2007). In brief, the north-south thermal gradient (cooler in the northern Hemisphere) cause changes in the surface winds, which tend to flow from the cooler equatorial to the southern tropical regions, but are deflected to the left such that along the Sumatra-Java coast trend of northwesterlies is generated, depressing the thermocline and generating the warming, accompanied by an increasing rainfall trend over the EIO, extending into the NWA.

#### 4.5 Discussion

Most Australian regions have experienced decreasing rainfall trends since 1950. NWA is a rare exception where a substantial increasing trend is observed. Using 20<sup>th</sup> century multi-member ensemble simulations in a global climate model forced with and without increasing anthropogenic aerosol forcing, a recent study by Rotstayn et al (2007) suggests that the increasing rainfall trend over NWA is attributable to the increasing Northern Hemispheric aerosols. The present study investigates the dynamics of the observed trend and compares with that seen in a climate model. We benchmark the model results in terms of drivers of NWA rainfall variability for each season, and examine the possibility that the increasing rainfall trend projects onto existing modes of variability.

It is found that the observed rainfall variability over NWA is weakly correlated with ENSO in all seasons, and features a weak decrease during an El Niño and a small increase during a La Niña event. In JJA and SON, NWA rainfall is influenced by IOD variability. An increase in NWA rainfall is normally linked to an increased SST in the EIO. In DJF, NWA rainfall tends to increase when a La Niña event generates basin-scaled cooling but with increased SST gradients towards the NWA coast. In this way, a decreased EIO SST in DJF is associated with an increased NWA rainfall. The reverse occurs during an El Niño event. The SST trend over the past 50 years shows an El Niño-like pattern in the Indo-Pacific system, unable to explain the increasing rainfall trend over NWA. Indeed, without the impact of the El Niño-like pattern, rainfall increase is greater.

The observed increase in rainfall occurs in the DJF season and is projected onto two modes of rain variability. The first mode is associated with an anomalously low MSLP off the NWA and WA coast instigated by the enhanced SST gradients towards the coast. The associated cyclonic flows bring high moisture air to northern Australia, thus leading to an increase in rainfall. The second mode is associated with anomalously high MSLP over much of the Australian continent; the anticyclonic circulation pattern with northwesterly flows west of 130°E and generally opposite flows in northeast Australia, determine that rainfall variability west and east of 130°E is of opposite polarity with anomalously high rainfall to the west and anomalously low rainfall to the east. The sum of the upward trend in these two modes generates the trend pattern with increasing NWA rainfall as shown in Fig. 4.1.

The total SST trend associated with the two EOFs resembles that of the raw SST in the sense that both show increased gradients towards the NWA coast. It is not clear what

drives the increased SST gradient along the coast. An enhanced Leeuwin Current with intensified onshore flows would be consistent with this change in the SST gradient. But the Leeuwin Current is strongest in the Southern Hemisphere winter and is highly correlated with ENSO, with a weakening current during an El Niño event. Over the past 50 years an El Niño-like warming pattern has occurred in the Pacific, which would mean a weakening Leeuwin Current, and is therefore not consistent with the dynamics presented here. A detailed study on the cause of the increased east-west gradients toward the coast is beyond the scope of the present study.

With increasing aerosols, the ensemble mean generates a realistic seasonal trend. As in the observed, the model rainfall increase occurs in the DJF season. Further, in the corresponding control experiment (no external forcing), modes of NWA rainfall variability are similar to the observed after removing the unrealistic features associated with model ENSO and variability over the IO. However, the model rainfall trend appears to be generated by processes that are not operating in the real climate system. As in other models, the model suffers from an equatorial cold-tongue bias: the tongue of anomalies associated with ENSO extends too far west into the western Pacific.

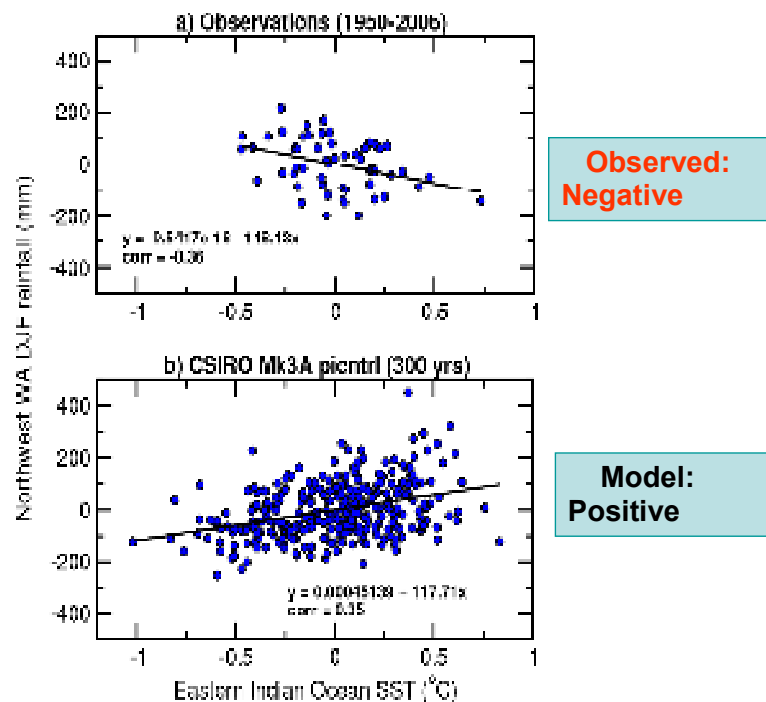


Figure 4.21: Panel a), Observed DJF SST anomalies ( $^{\circ}$ C) over EIO against NWA rainfall (mm). Panel b), the same as a) but from the 300-year control experiment.

Indeed the model anomaly tongue extends to the EIO with several ensuing consequences. Firstly, as the position of the warm pool moves in the zonal direction with the model

ENSO-like events, the strongest Australian rainfall-ENSO teleconnection lies in NWA, rather than the observed northeastern Australia (Shi et al., 2008a). Secondly, in all seasons, the IO has an IOD-like variability pattern; in DJF, apart from an IOD-like pattern that is linked with ENSO, there is also an IOD-like pattern that is independent from ENSO; neither is realistic as the observed IOD only operates in the JJA and SON seasons. This unrealistic presence of IOD-like variability in DJF induces an unrealistic EIO SST-NWA rainfall relationship, with an increasing SST in the EIO being associated with increasing NWA rainfall. In the observations an opposite relationship exists. The opposing relationship is highlighted in Fig. 4.21, which highlights the model problem: the relationship between EIO SSTs and NWA rainfall is a model artifact.

In the presence of increasing aerosols, a significant SST increase occurs in the tropical EIO with an overall pattern resembling the negative IOD phase. As a result, the modeled rainfall increase can be accounted for by the unrealistic relationship between model EIO SST and NWA rainfall that operates in the control experiment. This unrealistic relationship results from the model cold tongue problem. It is not clear if a model without such defects will produce the observed rainfall trend under forcing of increasing aerosols. Further modeling studies are therefore needed to properly evaluate the impact of aerosols on Australian rainfall.

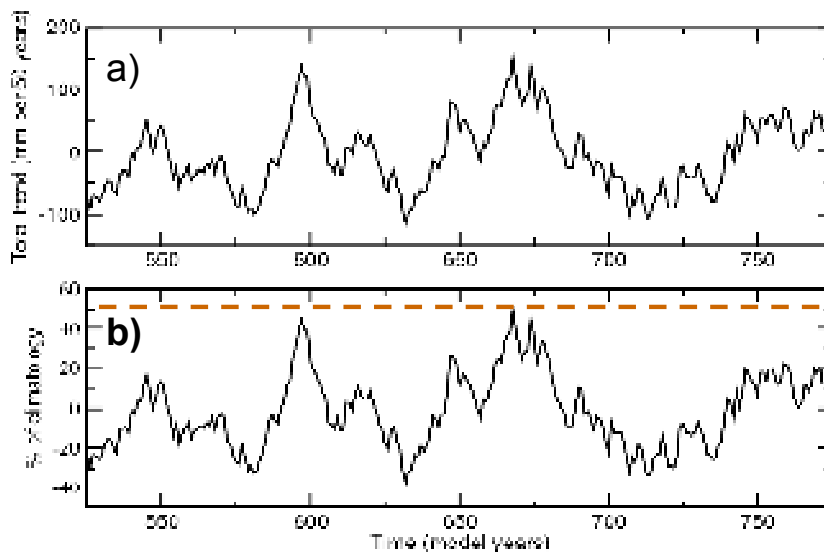


Figure 4.22: Time series of 50-year trends of NWA DJF rainfall obtained using a sliding window applied to the multi-century control experiment of Mk3.5 without climate change forcing, a) total 50-year trend, and b) percentage of climatology.

One possibility is that the observed rainfall increasing trend is driven by multidecadal variability. We have examined this by using outputs of a multi-century control experiment with the CSIRO Mk3.0 without any climate change forcing. In this version

of the model, the cold tongue bias is not as strong, and there is no IOD mode in DJF. It is found that over a 50-year period, positive trends comparable to the observed in terms of total rainfall amount (Fig. 4.22a) and percentage of climatology (Fig. 4.22b) is entirely possible without any needs of climate change forcing. However, since the rainfall teleconnection with climate drivers in this model is not realistically produced, the associated dynamics have not been examined further.

## Chapter 5: The future of Australian rainfall

Having addressed the importance of IO SSTs in the dynamics Australian rainfall variability and changes, we turn to the impacts of the Tasman Sea SSTs. Over the past decades, ocean warming off Maria Island (148.16°E, 42.36°S) near Tasmania, proceeded at a rate fastest that is fastest of the Southern Hemisphere (Pittock, 2003). The associated impacts include substantial changes in the boundaries of the South Pacific marine biodiversity. For example, the New South Wales native sea urchin, *Centrostephanus rodgersii*, off Australia's east coast, has been extending its range to the Tasmanian east coast since the late 1970s (Edgar, 1997), as has been the introduced shore crab, *Carcinus maenas*, from Victoria to Tasmania (Thresher et al., 2003). How does such large warming influence Australian rainfall?

This issue is particularly important as the majority of climate models forced by IPCC projections predict a continuation a large warming in the Tasman Sea. In this Chapter, we examine the influence of the Tasman Sea temperature anomalies, and interpret future Australian rainfall projections in terms of its rainfall teleconnection and that with other climate drivers. Main findings are:

- The fast Tasman Sea warming is generated by wind stress curls associated with an upward trend of the SAM, a common feature of models forced with IPCC projections.
- A positive SST anomaly over the Tasman Sea is conducive to a rainfall increase over the east coast, and understanding this impact is important for interpreting future Australian rainfall projections.
- A realistic simulation of the relative importance of the rainfall teleconnections with ENSO, the IOD, SAM, and the Tasman Sea temperature is essential for reducing the uncertainty of future rainfall projections.

This Chapter covers contents from the Cai et al. (2005b) and Shi et al. (2008a) papers. The candidate contributes to the Cai et al. (2005b) paper by conducting most of the analyses, particularly the part that links the changes in the wind stress curl with the SAM trend and with the changes in the EAC. The candidate initiates the original idea and carried out all the analyses presented in the Shi et al. (2008a), and receives help from co-authors who conducted the model experiments and helped organize the large amount of data and contributed vigorous discussions.

### 5.1 Background

The SAM has shown an upward trend over the past several decades (Thompson et al., 2000; Marshall, 2003; Marshall et al., 2004) with increasing MSLP in the midlatitudes. Observational (Thompson and Solomon, 2002) and modelling studies (Sexton, 2001; Gillett and Thompson, 2003) indicate that it is, or at least in part (Shindell and Schmidt, 2004), attributable to ozone depletion over the past decades. Under increasing atmospheric CO<sub>2</sub>, climate models produce increasing midlatitude MSLP incorporated in an upward trend of the SAM (Fyfe et al., 1999; Kushner et al., 2001; Cai et al., 2003a).

Based on all the IPCC models, Cai and Cowan (2007) suggest that most of observed SAM trend is induced by Antarctic Ozone depletion. As CO<sub>2</sub> continues to increase, a strengthening of the SAM trend is projected into the future, and this is one of the most robust and consistent responses of the global climate system to climate change.

To date, the focus has been on impacts of the projected SAM trend upon the climate from the stratosphere to Earth's surface, with little attention given to the consequential ocean circulation. Cai et al. (2005b) analyzed outputs of an ensemble of four climate change experiments with the CSIRO Mark 3.0 climate model forced by four different projections. The results show significant ocean circulation changes of pan-Southern Ocean scale.

Majority of models in the IPCC-AR4 predict a tendency for a future increase in summer (DJF) rainfall but a decrease in winter (JJA) rainfall in the SEA region (Fig. SPM7, Alley et al., 2007). As mentioned above, one of the most prominent features accompanying the rainfall changes is a warming rate off the Tasman Sea that is fastest of the SH. How will the fast Tasman Sea warming and the upward SAM trend affect Australian rainfall, particularly over the SEA region? Do their influences explain the seasonal difference in the SEA rainfall projection?

In Chapter 1, we have discussed dynamics of rainfall variability in the SEA region. It is affected by three “engines:” ENSO (Ropelewski and Halpert, 1987), the IOD (Ashok et al., 2003; Cai et al., 2005d) and the SAM (Cai and Cowan, 2006; Hendon et al., 2007). The impact of ENSO occurs mainly in summer with an anomalously low rainfall over SEA during an El Niño event; the IOD influences the spring and autumn rainfall such that when the SST in the eastern pole is anomalously low, rainfall over SEA decreases; and a positive SAM phase with an increasing MSLP in midlatitudes tends to increase SEA rainfall. The influence, however, is greatest in summer (discussed later), in sharp contrast to SWWA, where the SAM influences is strongest in winter and a positive phase in winter is associated with a winter rainfall decrease. In this Chapter, our focus will be on how the response of these engines, in addition to the Tasman Sea response, to climate change contributes to the seasonality of the rainfall change using outputs of CSIRO Mk3.0 climate model, which is one of the IPCC-AR4 model members. The model forced under a range of the IPCC emission scenarios produce the IPCC-AR4 median rainfall projection in both seasons.

Given that climate change signals tend to project onto existing modes of variability (Clark et al., 2001), it is appropriate to examine whether the projected rainfall change is consistent with what can be expected from teleconnections associated with the three engines in addition to the impact of the large Tasman Sea warming. It is found that although some model teleconnection patterns differ from those in the real world resulting from common model deficiencies, the seasonal stratification of the projected rainfall change is explainable by the super-imposing effects of the existing teleconnection patterns in the control experiment.

As discussed in Chapter 2, the “Mark 3.0” model (Gordon et al., 2002; Cai et al., 2003b) runs without flux adjustments. As in its previous version, when subject to climate change forcing (Cai et al., 2003a), the model SAM exhibits an upward trend. Here we focus on a control simulation, and four climate change experiments. The four climate change experiments following the A2 (two experiments), A1B, and B1 scenarios all incorporating CO<sub>2</sub> forcing, direct effect of sulfate aerosols, and ozone depletion. For more details about these projections, readers are referred to <http://www.grida.no/climate/ipcc/emission/089.htm>. Each of the four experiments starts from a different time of the control experiment, and together they provide an ensemble strategy. The ozone forcing incorporates a full recovery of the ozone content by 2048. Despite this, in all warming experiments the SAM shows an increasing trend. In what follows, we show changes of a 31-year mean over the period of 2055-2085 averaged over the four climate change experiments from a control climate. Although we show only the averaged pattern, each individual experiment produces a change pattern that is similar to the average, highlighting the robustness of the change.

## 5.2 Dynamics of the Tasman Sea warming

Strong zonal wind changes take place (Fig. 5.1a), with the maximum located at 60°S. Since it is the wind stress curl, not the wind stress itself, that primarily drives ocean circulation, we calculate the change of the wind stress curl, which is dominated by the meridional gradient of changes in zonal wind stress. An important feature is that although the location of the maximum change in zonal wind stress is at approximately 60°S (Thompson and Solomon, 2002; Gillett and Thompson, 2003), the maximum curl change is located at approximately 48°S (Fig. 5.1b). Spatially, large increases in the positive wind stress curl are observed south of the Tasman Sea and New Zealand.

Sverdrup balance implies a significant change to the wind driven circulation (Godfrey, 1989). At 36°S the zonal average of curl from the east to the west boundary is  $1.4 \times 10^{-8} \text{ N m}^{-3}$ . Sverdrup relationship produces an intensification of the basin interior transport, and an implied EAC transport increase at this latitude of approximately 10 Sv (1 Sv =  $10^6 \text{ m}^3 \text{ s}^{-1}$ ), or by some 20%. Changes in the modeled barotropic transport streamfunction (Fig. 5.1c) confirm a change of this magnitude. Moreover, the strengthening of the EAC is part of a larger scale circulation change: the entire southern midlatitude circulation intensifies with a large change in the South Atlantic Ocean.

To confirm that the wind stress changes are the major forcing of the circulation change, Godfrey’s Island Rule model (Godfrey, 1989) is used to obtain a depth-integrated transport streamfunction, using wind stress of the control and warming experiments. As Sverdrup circulation requires an eastern boundary (in this case, the South American coast), we carry out the calculation to the southern-most latitude 54°. The wind stress inputs are interpolated onto a 2x2 degree grid as in the original algorithm, with the Indonesian Throughflow Passage open (see section 2.2.4).

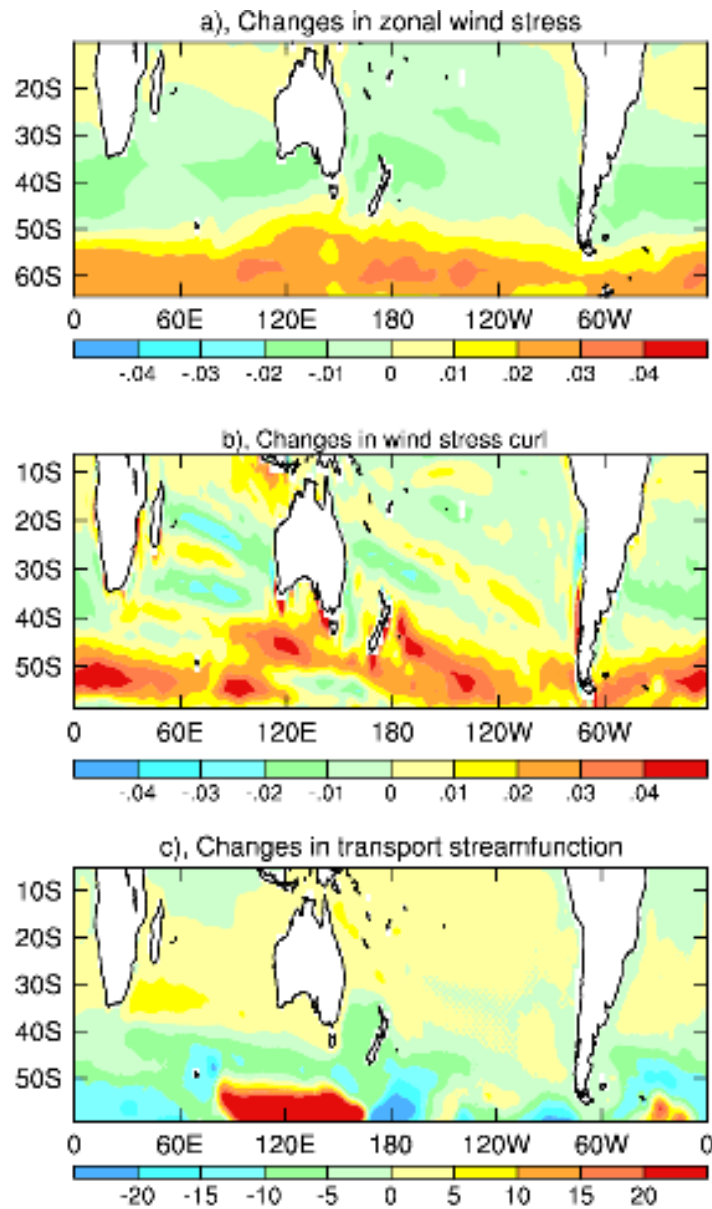


Figure 5.1: Ensemble-mean change averaged over the period of 2055-2085, a) zonal wind stress ( $N m^{-2}$ ), b) wind stress curl ( $N m^{-3}$  scaled by a factor of  $10^{-6}$ , and c) vertically integrated barotropic streamfunction ( $Sv$ ,  $1 Sv = 10^6 m^3 s^{-1}$ ). Note that compared to panels (b) and (c), panel (a) has a  $5^\circ$  southerly shift to show the maximum wind change is at  $60^\circ S$ . The pattern correlation coefficients between individual ensemble members are in the range of 0.95-0.98 for a), 0.87-0.95 for b), and 0.93-0.99 for c) (from Cai et al., 2005b).

The wind-driven EAC (Figs. 2.3a and 2.3b) bifurcates at approximately 20°S, as again shown in Figs. 5.2a and 5.2b. Part of the EAC separates from the coast at approximately 32°S, the majority passes through the Tasman Sea. The flow then veers northwest into the Great Australian Bight, IO, and to the Atlantic Ocean, before it retroflects, forming a southern midlatitude inter-basin “super-gyre,” linking the South Pacific, Indian and Atlantic Oceans (Cai, 2006; Ridgeway and Dunn, 2003; Tilburg et al., 2001). The central features are: first, the South Pacific subtropical gyre increases significantly. This is clearly seen in the difference plot (Fig. 5.3); second, the increase in the flow passing through the Tasman Sea is accompanied by stronger recirculations in the longitudes from east of New Zealand to the eastern boundary (the South American coast); finally, the Southern Ocean “super-gyre” strengthens and shifts southward (Fig. 5.3).

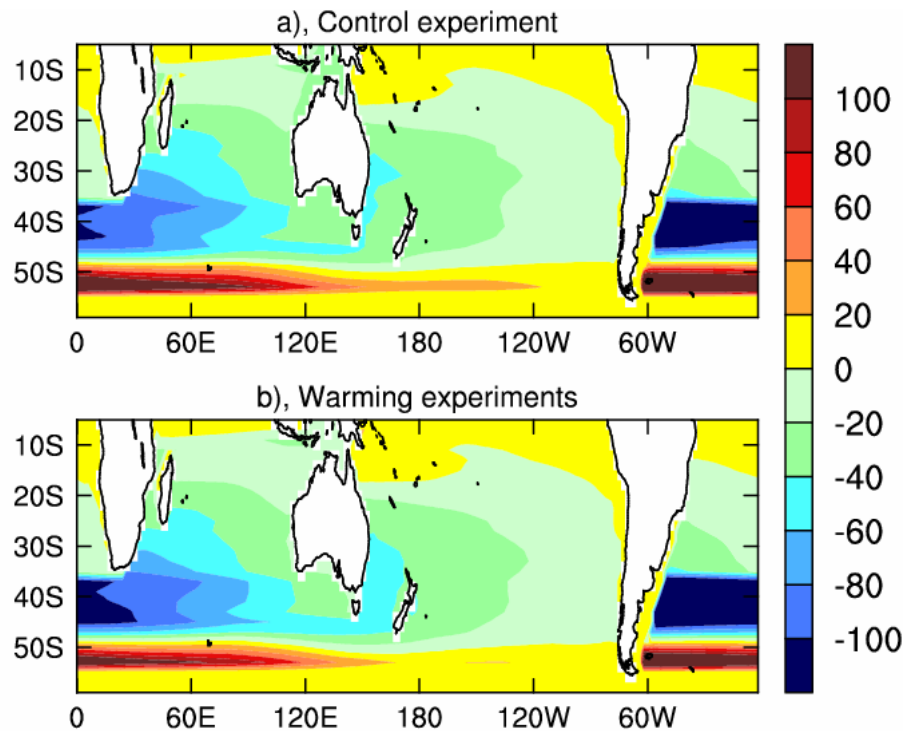


Figure 5.2: Transport streamfunction ( $Sv$ ) from Godfrey's Island Rule model forced by model winds from, a) control experiment, b) ensemble-mean of warming experiments averaged over 2055-2085. The pattern correlation coefficients between individual ensemble members are in the range of 0.95-0.98 for zonal wind stress change and 0.87-0.96 for meridional wind stress change (adapted from Cai et al., 2005b).

The strong resemblance between the wind-driven change (Fig. 5.3) and the total change from the model output (Fig. 5.1c) in the midlatitudes means that the midlatitude changes in the ocean circulation are primarily driven by the wind changes. Both the coupled

model and the Godfrey model predict an annual mean increase of about 10 Sv, or some 20% of the control experiment, in the EAC flow passing through the Tasman Sea. In the coupled model, the change is also forced by buoyancy forcing and its interactions with bottom topography. The positive change of the streamfunction in the longitude band of 90°E to 160°E (Fig. 5.1c), indicating a local change with a strengthening clockwise circulation, is probably due to these processes, as it is not present in the circulation change inferred from the wind (Fig. 5.3) (Cai et al., 2005b).

As discussed in Cai (2006), the reason that the EAC increases more markedly than other subtropical gyres is because the southern-most tip of the lateral boundaries of the South Pacific gyre are either close to or extend into the zonal strip of strong curl changes. As such, the South Pacific gyre is able to tap into the effect of the curl changes integrated from the South American coast, through New Zealand, to the East Australian coast. Thus, the resultant circulation changes is stronger, broad northward flows in the interior and off New Zealand's northeast coast, and swifter narrow southward EAC flows through the Tasman Sea as a result of Stommel's westward intensification.

A feature of the poleward shift in wind stress curl is that the EAC also migrates poleward. To illustrate this, the latitude where the EAC transport is maximum is identified, for one experiment. This is plotted in Fig. 5.4. The southward extension of the EAC is very clear. In all other experiments, a similar feature is produced. Thus, the response to climate change forcing of the Southern Ocean includes a strengthening of the EAC flow through the Tasman Sea generating a warming rate in the Tasman Sea that is the largest of the entire SH. Below we examine the impact of Tasman Sea warming and the response of other climate drivers in determining Australian future rainfall changes.

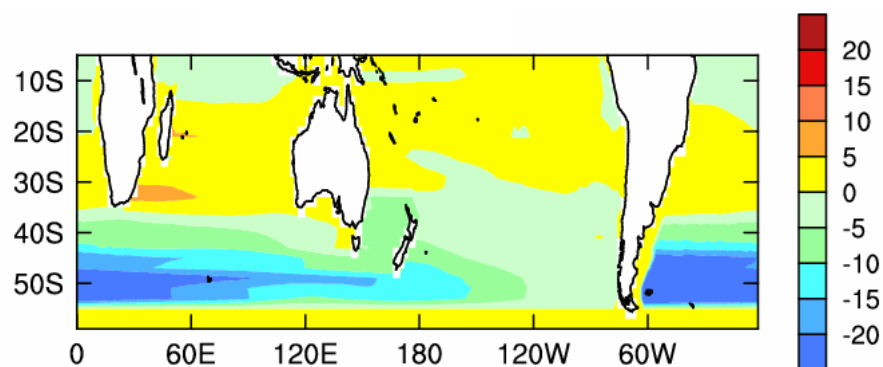


Figure 5.3: Change in transport streamfunction (Sv) from Godfrey's Island Rule model forced by model winds as the difference between the control experiment and ensemble-mean of warming experiments averaged over 2055-2085 (adapted from Cai et al., 2005b).

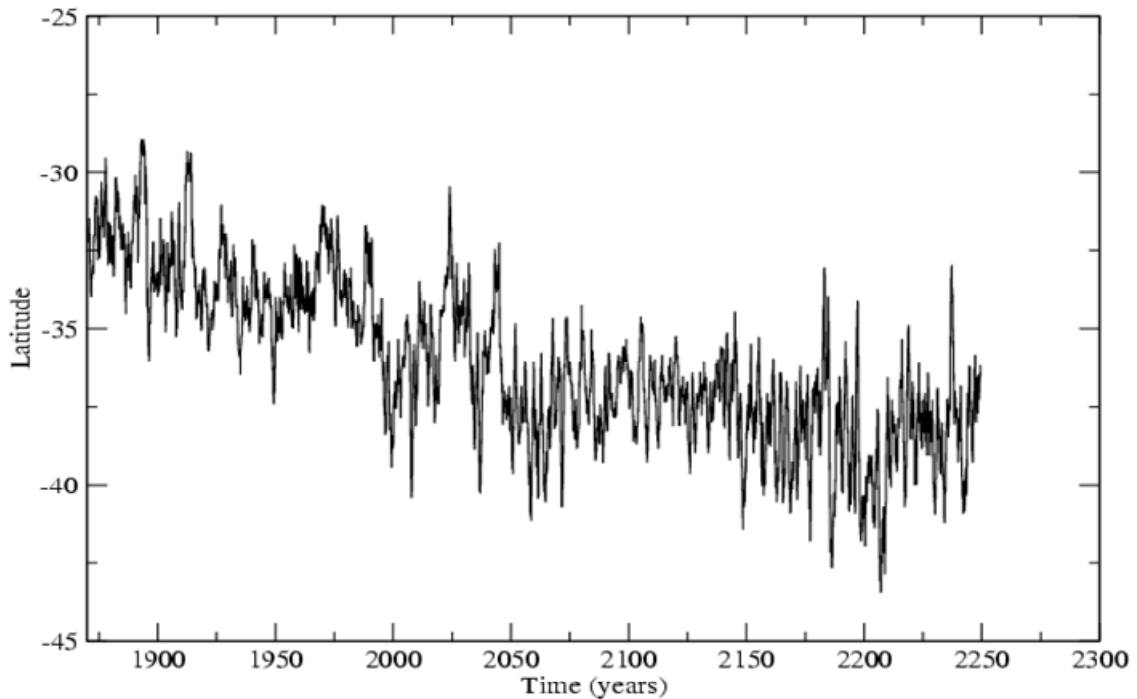


Figure 5.4: Time series of latitude in which the model EAC reaches a maximum.

### 5.3 Dynamics of SEA rainfall variability and change

We focus on a control simulation, and four climate change experiments using the CSIRO Mk3.0 model. The control simulation is used to examine the relationship of Australian rainfall with the three engines of the Australia climate and with the Tasman Sea temperature. For this purpose anomalies are obtained referenced to the mean averaged over the full 300 years. Previous studies have described the simulation of ENSO and the IOD in this version of the model (Cai et al., 2003b; Cai et al., 2005d). The four climate change experiments follow the IPCC A2 (two experiments), A1B, and B1 scenarios that all incorporate CO<sub>2</sub> forcing, the direct effect of sulfate aerosols, and stratospheric ozone depletion. Each of the four experiments starts from a different time of the control experiment, and together they provide an ensemble strategy. More experimental details are provided in Cai et al. (2005b). In what follows, we present changes of a 31-year mean over the period of 2055-2085 averaged over the four climate change experiments from a control climate. Although we show only the ensemble averaged pattern, each individual experiment produces a change pattern that is similar to the average, highlighting the robustness of the change.

#### 5.3.1 Changes in summer and winter rainfall in the CSIRO model

Changes in SEA rainfall by the year 2070 in the Mk3 show a clear seasonal stratification. In summer, an increase with maximum changes along the eastern coast (left column, Fig. 5.5a), translates to some 10-20% increase (right column, Fig. 5.5b). The large-scale pattern shows that there is a band of rainfall decrease centered at about 45°S. By

contrast, in winter (right column of Figs. 5.5a and Fig. 5.5b ), rainfall change shows a weak decrease over SEA, and a zonal strip of decline with maximum reduction over the southern-most part of Australia and SWWA. Throughout SEA, the decrease translates into a reduction of some 0-10% (right column, Figs. 5.5a and 5.5b).

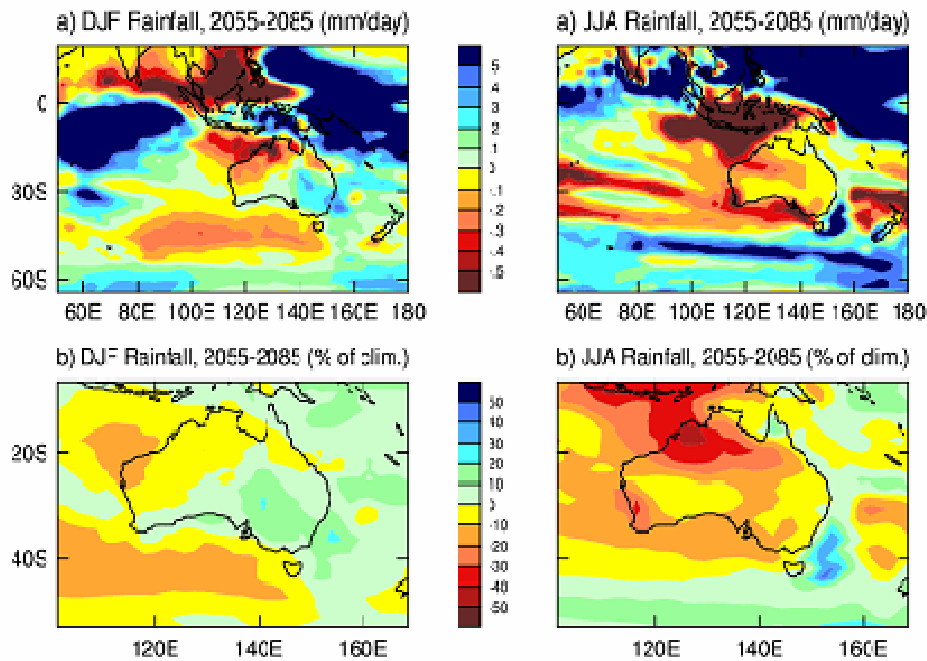


Figure 5.5: Rainfall changes (a) in  $\text{mm day}^{-1}$  and (b) in percentage of control climatological values. Left column is for summer (December – February, DJF) and right column is for winter (June – August, JJA) (from Shi et al., 2008a).

The zonal strip of rainfall decrease is punctuated by a rainfall increase over the Tasman Sea, particular in winter. As will be examined in section 4 and in Shi et al. (2008a), the fast Tasman Sea warming rate promotes convection and rainfall. However, despite this effect, winter rainfall shows a reduction over SEA, in contrast to summer rainfall. The strongest contrast is seen near the coast. These patterns resemble those presented in the IPCC-AR4 (Fig. SPM7, Alley et al., 2007). Other features include a rainfall reduction in both seasons over NWA, where there is little consensus from IPCC-AR4 models. We will briefly discuss the cause of the decrease in the Mk3 model.

Below we examine the teleconnection of Australian rainfall with the three climate engines and with variability of the Tasman Sea temperature using outputs of the 300-year control experiment. The purpose is to examine if one can interpret rainfall changes in terms of teleconnections between Australian rainfall and modes of variability in the present-day climate system (the control experiment).

### 5.3.2 Australian rainfall teleconnections in the control climate

Given that the largest difference between summer and winter rainfall changes occurs along the east coast, we examine the relationship between east coast rainfall and the circulation fields in the control experiment. Correlation between time series of rainfall averaged over an east coast box (150°E:155°E, 33°S:38°S) with grid-point circulation anomaly fields is conducted. As east coast rainfall increases, rainfall over SEA and the Tasman Sea increases in both summer (left column, Fig. 5.6a) and winter (right column, Fig. 5.6a). In both seasons, the imprints of the influence from the three engines are evident. A weak La Niña-like pattern in both seasons (Fig. 5.6b), a negative phase of the IOD with a warm pole in the EIO in the winter season (right column, Fig. 5.6b), and a SAM-like pattern in summer (left column, Fig. 5.6c) only, are all conducive to a rainfall increase. In particular, during both seasons, an increase in east coast rainfall is associated with anomalous on-shore flows that bring moist air to SEA (Fig. 5.6c). These flows are, in principle, geotropically balanced by the MSLP anomalies shown in Fig. 5.6c. In both seasons stronger SEA rainfall is associated with anomalously high the temperature (Fig. 5.6b).

However, there are several significant differences. Firstly, the influence by the EIO SST is weak in summer with far smaller correlations there (left column, Fig. 5.6b), when compared with correlations for winter (right column, Fig. 5.6b), in which a negative phase IOD pattern emerges. This is not surprising given IOD episodes occur only in the winter season in the observed (Saji et al., 1999) and as simulated by the present model (Cai et al., 2005d). Such a winter influence by the IOD with increasing SEA rainfall associated with a warmer SST off the Sumatra-Java coast has also been examined (Ashok et al., 2003). Secondly, in summer the influence from the Tasman Sea temperature is stronger than in winter; the correlation in winter the far weaker and more localized (right column, Fig. 5.6b) with a lower level of zonal symmetry. However only in winter does the SST anomaly “hug” the coast; in summer, there are little SST anomalies immediately off the SEA coast. Finally, as will be discussed later, the summer MSLP anomaly pattern (left column, Fig. 5.6c) strongly resembles the summer SAM pattern (left column, Fig. 5.6c) with the midlatitude anomaly center located at some 45°S; such is not the case in winter, when the MSLP anomaly pattern (right panel, Fig. 5.6c) has the maximum correlation located at 50°S, far further to the south than the winter SAM pattern.

As discussed in Shi et al. (2008a), these differences reflect the varying importance with seasons of the three engines and variations of the Tasman Sea temperature in controlling SEA rainfall. In summer, it appears that the SAM and the Tasman Sea SST are important, although the two factors may be linked; in winter, the IOD and the Tasman Sea temperature appear to be significant, but the influence of ENSO and the SAM is less clear. In what follows, we will explore in more details how each engine affects rainfall in SEA.

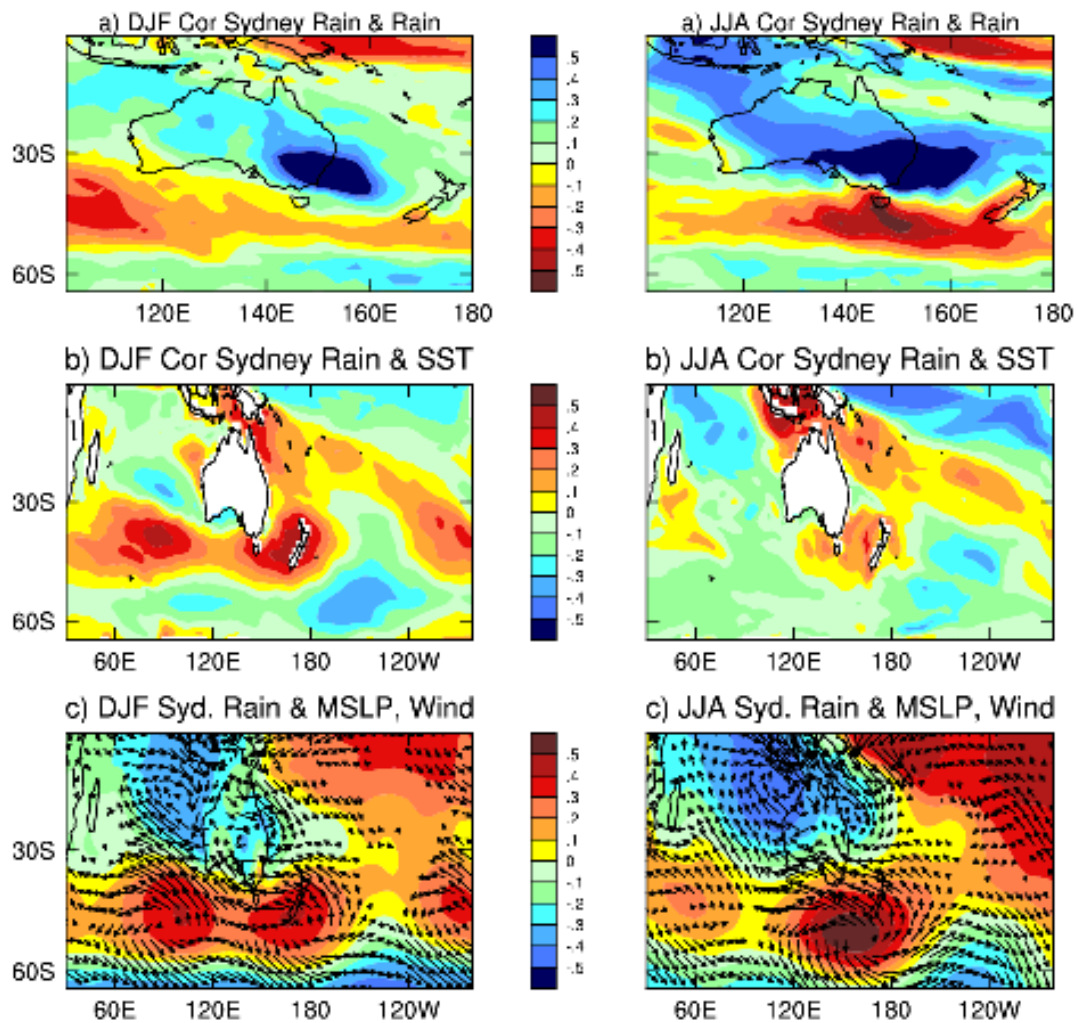


Figure 5.6: Correlation between time series of east coast rainfall (averaged over  $150^{\circ}\text{E}:155^{\circ}\text{E}$ ,  $33^{\circ}\text{S}:38^{\circ}\text{S}$ ) and rainfall everywhere (a), SST (b), and MSLP and wind vectors (c). Left column is for summer and right column is for winter. An absolute value greater than 0.115 is statistically significant at a 95% confidence level. Maximum vector represents a value of 1.4 (from Shi et al., 2008a). In (c), maximum vector indicate and correlation coefficient of 1.

### 5.3.2.1 The Tasman Sea temperature anomalies and Australian rainfall.

The analysis is in part motivated by an investigation of the impact of the large Tasman Sea warming, but the left column of Fig. 5.6b shows that in the summer season there is

little relationship with SST immediately off the coast. It turns out that the strongest influence on rainfall by SST variability immediately off the east coast resides outside the box where the rainfall time series is taken. Figure 5.7 plots correlation between a time series of SST anomaly averaged over a box immediately off the east coast ( $150^{\circ}\text{E}$ - $155^{\circ}\text{E}$ ,  $32^{\circ}\text{S}$ - $38^{\circ}\text{S}$ ) with rainfall fields (Fig. 5.7a). In summer, an anomalously high SST “hugging” the coast (left column, Fig. 5.7b) is associated with a rainfall increase over southern-most SEA, and the impact extends from the coast to the inland; in winter the impact is generally weaker and more confined to area along the coast (right column, Fig. 5.7b). This aerial difference is associated with the fact that in summer the subtropical ridge is farthest to the south, and SEA is able to be impacted by episodic easterlies events; whereas in winter, the stronger westerlies over SEA ensure that the impact is mainly downstream and weaker. An examination reveals that a higher SST along the coast promotes convection, cloud formation, and rainfall. The high SST has a tendency to increase evaporation, however, the associated decreasing midlatitude westerlies tend to offset this effect, giving rise to a net small signal in evaporation. Overall, Fig. 5.7 shows that a warm anomaly immediately off east coast is conducive to rainfall in southern SEA in summer and along the coast in winter.

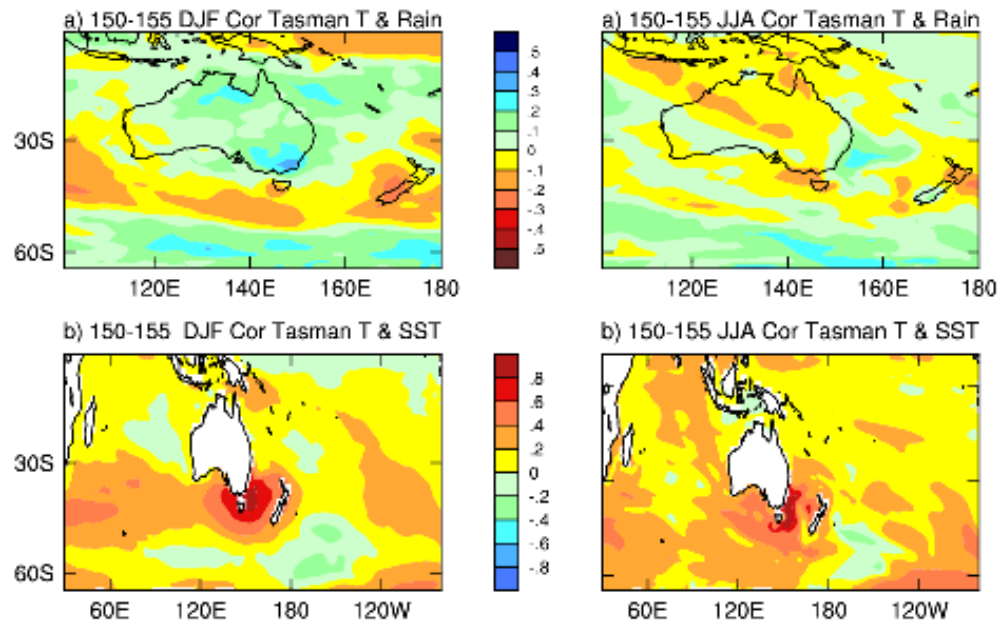


Figure 5.7: Correlation between time series of east coast SST (averaged over  $150^{\circ}\text{E}$ : $155^{\circ}\text{E}$ ,  $33^{\circ}\text{S}$ : $38^{\circ}\text{S}$ ) and grid-point rainfall (a) and SST (b). Left column is for summer and right column is for winter.

### 5.3.2.2 The impact of ENSO

The impact of ENSO is realized by correlating the model NINO3.4 index (SST anomalies averaged over 170°W-120°W and 5°S-5°N) with rainfall (Fig. 5.8a). As in many other models, Mk3 suffers from a common deficiency in the simulation of the equatorial Pacific SST structure (see Cai et al., 2003b for a detailed description). The mean state in each season features a cold tongue that extends too far west, and a western Pacific warming pool and the associated rising branch of the Walker circulation that are “pushed” too far into the Western Pacific. Further, the cold tongue is too narrow and too equatorially confined. As a consequence, ENSO anomalies along the equatorial Pacific extend too far west and are too equatorially confined as well (Fig. 5.8b), leading to an unrealistic relationship between ENSO and NWA rainfall: during a La Niña summer (left column, Fig. 5.8a) the western Pacific convection center moves westward, increasing rainfall over NWA as well as northeast Australia, and vice-versa during an El Niño. In reality, ENSO mainly affects the eastern Australia, particularly in the northeast (McBride and Nicholls, 1983; Ropelewski and Halpert, 1987). Thus there is an unrealistic relationship between NWA rainfall and ENSO in the model. Further, linked to the equatorial confinement of the anomaly, the influence in SEA is weak.

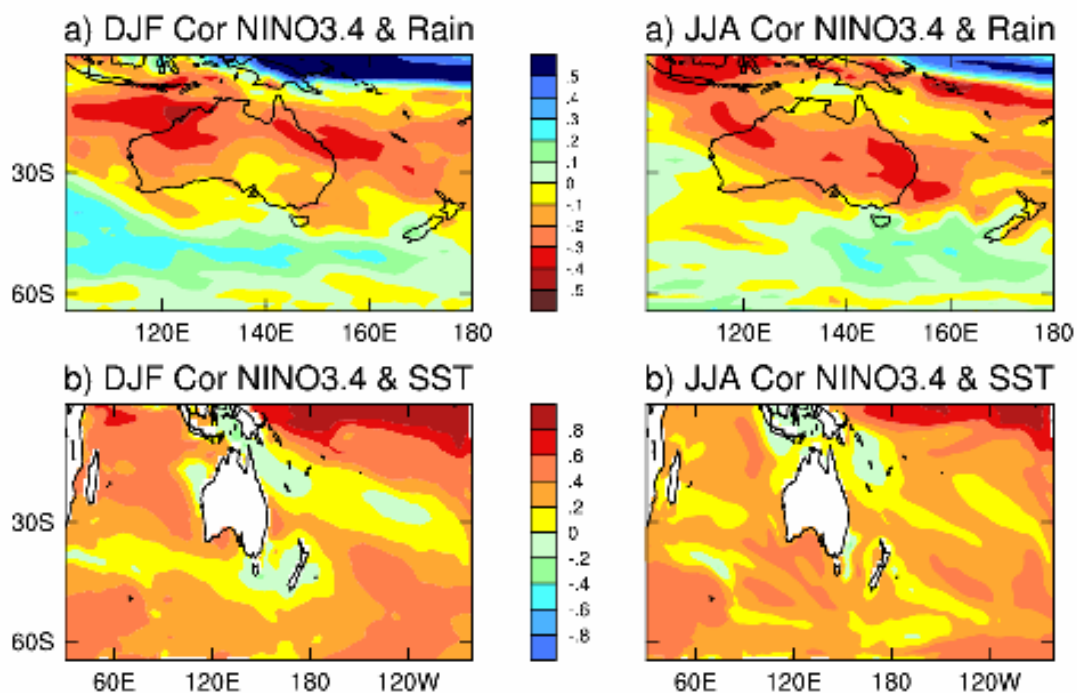


Figure 5.8: The same as in Fig. 5.7, but between NINO3.4 grid-point rainfall (a) and SST (b) (adapted from Shi et al., 2008a).

In winter, however, ENSO's influence on SEA rainfall is rather strong (right column, Fig. 5.8a). The influence is achieved through a strong linkage between the model ENSO and the model IOD. As discussed in Cai et al. (2005d), in the present version of the model, the majority of the IOD events commence their development in the year when an El Niño reaches a matured phase (showing only weak negative SST anomalies over Sumatra-Java coast in the right column of Fig. 5.8b), but peak in the ensuing winter and spring seasons; and there is virtually no independent IOD events. As a result, the ENSO-rainfall relationship in part arises from this unrealistically strong linkage between model ENSO and the model IOD. Regardless of the timing of the model IOD, when the EIO is anomalously low, SEA rainfall decreases, with less northwest cloud band events reaching SEA (Nicholls, 1989). As will be clear, the weak influence on SEA rainfall from ENSO in summer and the strong impact from the IOD in winter (see section 4.3) significantly contribute to the seasonal difference in SEA rainfall projection.

### **5.3.2.3 The impact of IOD**

To gain further insight on the influence of SST variability in the EIO, we conduct an empirical orthogonal function (EOF) analysis on SST anomalies in an IO domain (20°S-20°N, 30°E-120°E). The EOF1 time series is then correlated with grid point rainfall and SST anomalies as shown Figs. 5.9a and 5.9b. As in previous figures we show correlation maps rather than the EOF patterns to facilitate comparisons. In summer, IO variability is by and large driven by easterly anomalies associated with ENSO: as the Australian summer monsoon commences in December, the mean winds become westerly in the equatorial EIO. The induced easterly anomalies then act to reduce the wind speed. The reduced latent heat flux, along with increased surface shortwave radiation, warms the EIO, yielding a basin-scale warm anomaly. This basin-scale anomaly has been traditionally described as the response of the IO to ENSO (e.g., Klein et al., 1999; Chambers et al., 1999). In association, the rainfall correlation pattern with IO EOF1 (left column, Fig. 5.9a) is somewhat similar to that associated with ENSO featuring an unrealistically weak teleconnection with SEA rainfall and an unrealistically strong correlation with NWA rainfall.

For the winter season, the EOF1 reflects the matured phase of the IOD, that is, 6 months after an El Niño peaks and the equatorial Pacific is in a neutral phase or is entering an early La Niña phase (right column, Fig. 5.9b), a strong band of rainfall teleconnection extending from the EIO is seen when the EIO SST is anomalously low, and SEA rainfall decreases (right column, Fig. 5.9a).

### **5.3.2.4 The impact of the SAM**

To further highlight the role of the SAM on SEA rainfall variability, we conduct correlations between the model SAM (MSLP EOF1) time series and circulation fields (Figs. 5.10a and 5.10b). Again to facilitate comparison with what is shown in Fig. 5.6, the SAM pattern is shown as maps of correlation between the EOF1 time series and MSLP anomalies (Fig. 5.10c). On interannual time scales, the SAM reflects variations of the

subtropical ridge (Cai and Cowan, 2006), which is located furthest to the south in summer but furthest to the north in winter. As a consequence, the center of variability in the summer SAM is located further south than the winter SAM (Cai and Cowan, 2006).

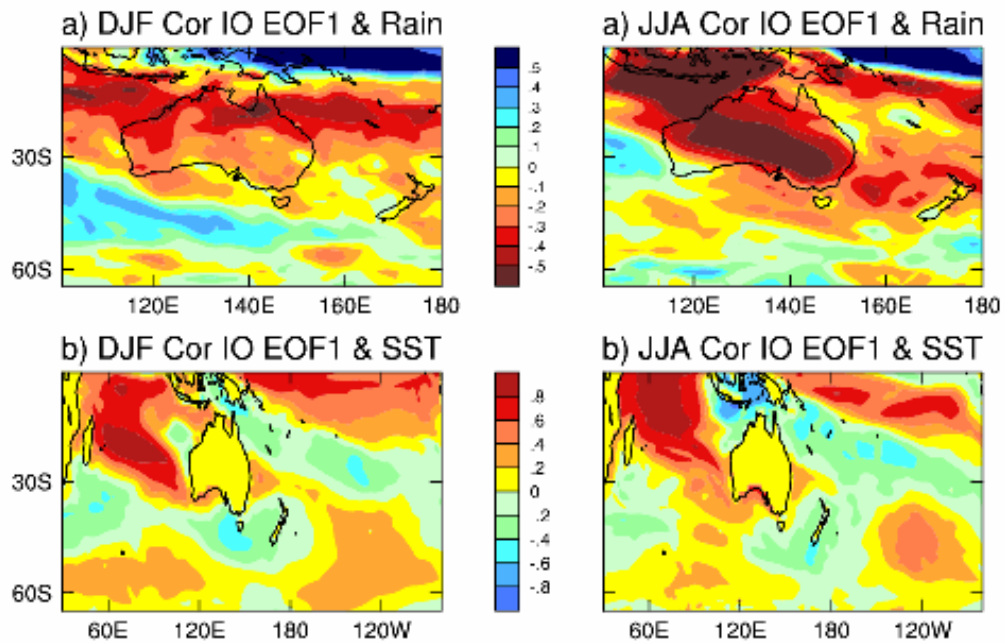


Figure 5.9: The same as in Fig. 5.7, but between IO SST EOF1 and grid-point rainfall (a) and SST (b) (from Shi et al., 2008a).

In summer a positive SAM phase is conducive for SEA rainfall, particularly along the east coast, where anomalously high rainfall is seen to cover most of the Tasman Sea (left column, Fig. 5.10a). The associated SST anomaly pattern resembles that shown in Fig. 5.6b (left column), that is, a positive SAM phase is associated with a positive SST anomaly in the Tasman Sea. The associated circulation pattern, with on-shore flows bringing moist air towards the coast, is also similar (left column, Figs. 5.10c and 5.6c). The strong resemblance highlights the significant impact of the SAM in driving SEA rainfall variations. Although an upward trend of the SAM over a long time generates a stronger EAC advecting more warm water south (Cai et al., 2005b), the time scale involved is for Rossby waves to transverse the Pacific from the eastern boundary (Pacific side of the South American coast), which is of the order of some 20 years at 45°S (Qiu and Chen, 2006, Shi et al., 2008a). The correlation shown in the left column of Fig. 5.10b does not reflect this, because if this process is occurring, strongest anomalies should be found immediately off the coast. This is not the case. Instead, it represents variations on much shorter time scales associated with local variations of a high wave-number built in the SAM pattern: a high MSLP reduces cloud cover, and increases radiation into the ocean, generating warming anomalies (Cai and Watterson, 2002).

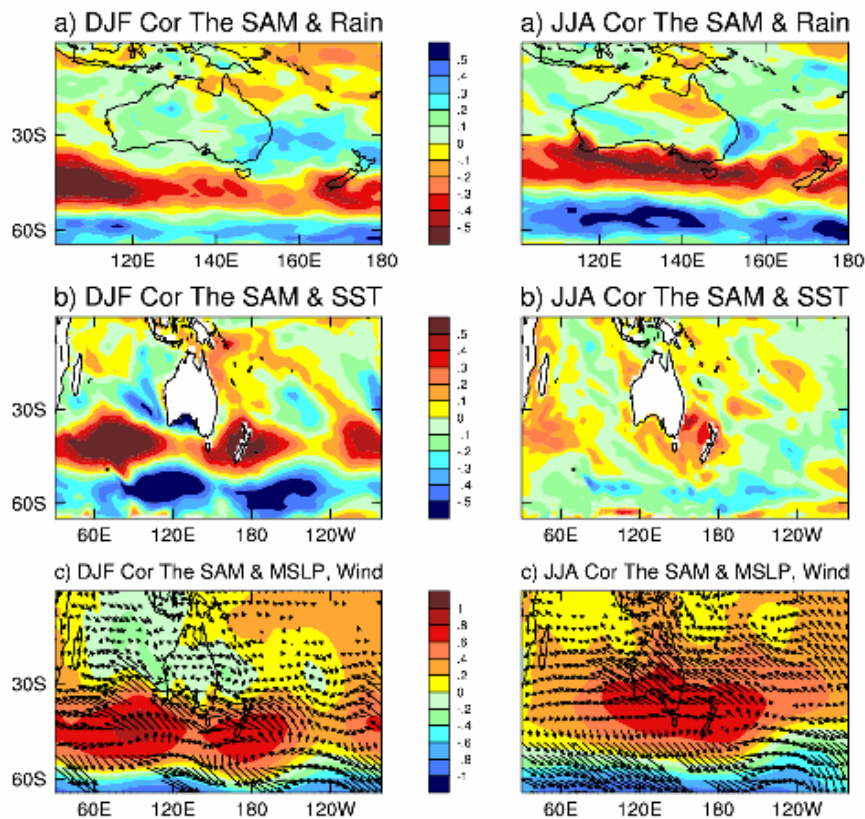


Figure 5.10: The same as in Fig. 5.6, but between MSLP EOF1 (the SAM) time series and circulation fields (Shi et al., 2008a). In (c), maximum vector indicate and correlation coefficient of 1.

In winter, in association with a positive SAM phase, rainfall increases along the east coast, both off shore and inland, but reduces over the southern-most Australia and SWWA. The SST anomalies associated with the SAM (right column, Fig. 5.10b) are rather weak, and are located further to the north in comparison to the summer season (left column, Fig. 5.10b); the maximum correlation situates along the coast. The associated flows are conducive for rainfall increase along the coast. Comparing the flow and MSLP patterns shown in the right column of Fig. 5.6c with the corresponding patterns associated with the SAM (right column, Fig. 5.10c), we see that maximum MSLP and flow anomalies associated with the SAM are located further north. Thus a positive SAM does not provide the most favorable condition for rainfall along the east coast. However, a positive SAM is conducive for a rainfall increase along the coast (Shi et al., 2008a).

## 5.4 Interpretation of rainfall changes

A description is given of the change in circulation fields, which are plotted in Fig. 5.11 for MSLP, and Fig. 5.12 for SST and other fields. The relationship between rainfall and climate engines in the control experiment is then invoked to explain the rainfall changes.

Immediately clear from Figs. 5.11a is that the change in MSLP is SAM-like. To highlight this point, the EOF1 of the 300-year MSLP anomalies of the control experiment is plotted in Fig. 5.11b. We see that in both seasons the changes in MSLP are mainly projected onto the EOF1 pattern as already discussed by many studies (Fyfe et al., 1999; Kushner et al., 2001; Cai et al., 2003a). As discussed in section 3 and Shi et al. (2008a), the largest difference in the summer and winter rainfall projection lies in the latitudinal distribution of a band of rainfall reduction: in winter, the band situates over southern Australia, whereas in summer the band located to the south (Fig. 5.5a). The dynamics for this latitudinal differentiation in summer and winter reduction is the seasonal difference in the MSLP changes (Figs. 5.11a and 5.11b). The maximum positive change in summer is situated to the south of that in winter such that no significant positive MSLP trend in summer is located over SEA. The seasonal difference in the MSLP changes is in turn consistent with seasonal difference in the SAM variability centers. Overall, the SAM-like change means that the subtropical ridge is experiencing a poleward shift in both seasons.

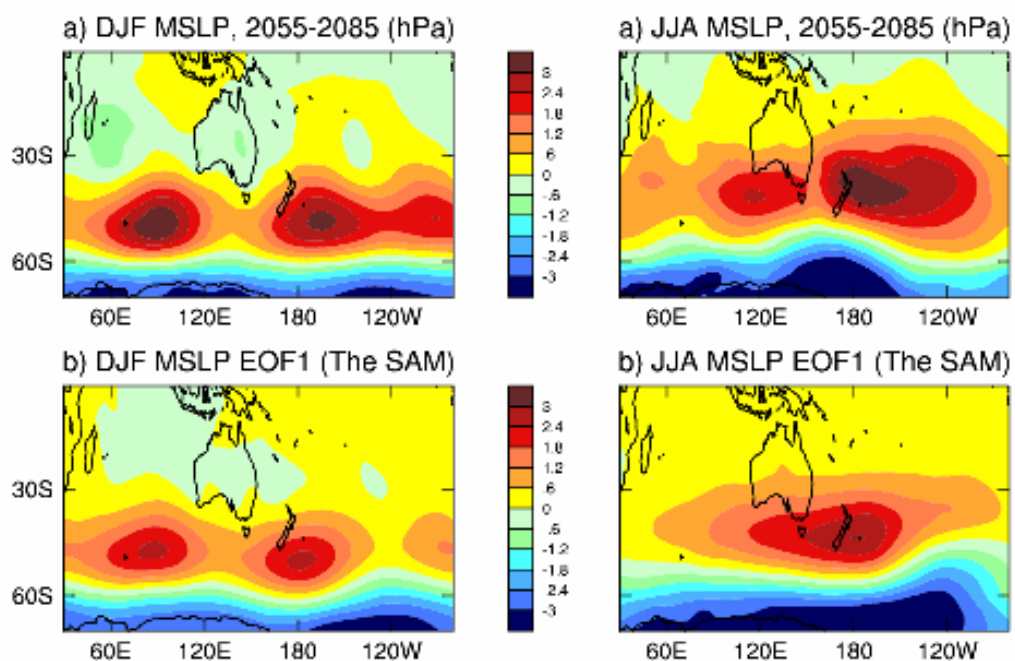


Figure 5.11: Changes of MSLP (hPa) in the warming experiments from the control climate averaged over a 31-year period between 2055 and 2085 (a), and pattern of MSLP EOF1 in the control experiment.

As already discussed in Cai et al. (2005b), the strong SAM-like trend is associated with decreasing mid-latitude westerlies and increasing high-latitude westerlies. The wind changes translate into an increase in positive wind stress curl. As a consequence, the EAC intensifies and shifts poleward, generating a great warming rate in the Tasman Sea in both seasons. In the Indo-Pacific, the pattern is El Niño-like in summer (comparing left column of Figs. 5.12a and 5.12b) and in winter (comparing right column of Figs. 5.12a and 5.12b) in terms of zonal SST gradients, particularly over the EIO and western Pacific regions, it is consistent with previous results (e.g., Meehl and Washington, 1995; Cai and Whetton, 2001).

#### **5.4.1 Summer rainfall change**

According to the relationship detailed in section 5.3.2, the SAM-like change and the Tasman Sea warming are conducive for a rainfall increase over the Tasman Sea and SEA, whereas an El Niño-like warming pattern in the equatorial Indo-Pacific contributes to a reduction in rainfall. The net effect of these three factors is a rainfall increase, because the effect of the El Niño-like warming pattern is far weaker than the combined impact from the SAM and the Tasman Sea warming. This is further illustrated by changes in the longwave radiation at the top of the atmosphere, which indicates enhanced convection (left column, Fig. 5.12b) and by the reduced surface shortwave radiation (left column, Fig. 5.12c) over SEA.

Over NWA, the El Niño-like warming pattern contributes to the rainfall decrease, consistent with the unrealistic model relationship between ENSO and NWA rainfall. In association, outgoing longwave radiation at the top of the atmosphere decreases (positive value in the left column Fig. 5.12a), and incoming shortwave radiation at the surface increases (left column, Fig. 5.12b). However, these changes over NWA result from the unrealistic teleconnection between the model ENSO and the model NWA rainfall. It is not clear whether in the absence of such an unrealistic relationship, such a rainfall decrease will be generated.

A recent study using a model with a comprehensive interactive aerosol scheme (Rotstayn et al., 2007) shows that over the past 50 years the increasing level of Asian aerosols is responsible for the summer rainfall increase over NWA. In the present version of the model, the interactive aerosol scheme is not included, and an ensemble of 4 experiments of the 20<sup>th</sup> century does not produce the observed NWA rainfall increase. Thus, the projected rainfall decrease over NWA in this version of the model is not due to a decreasing level of aerosols going into the future.

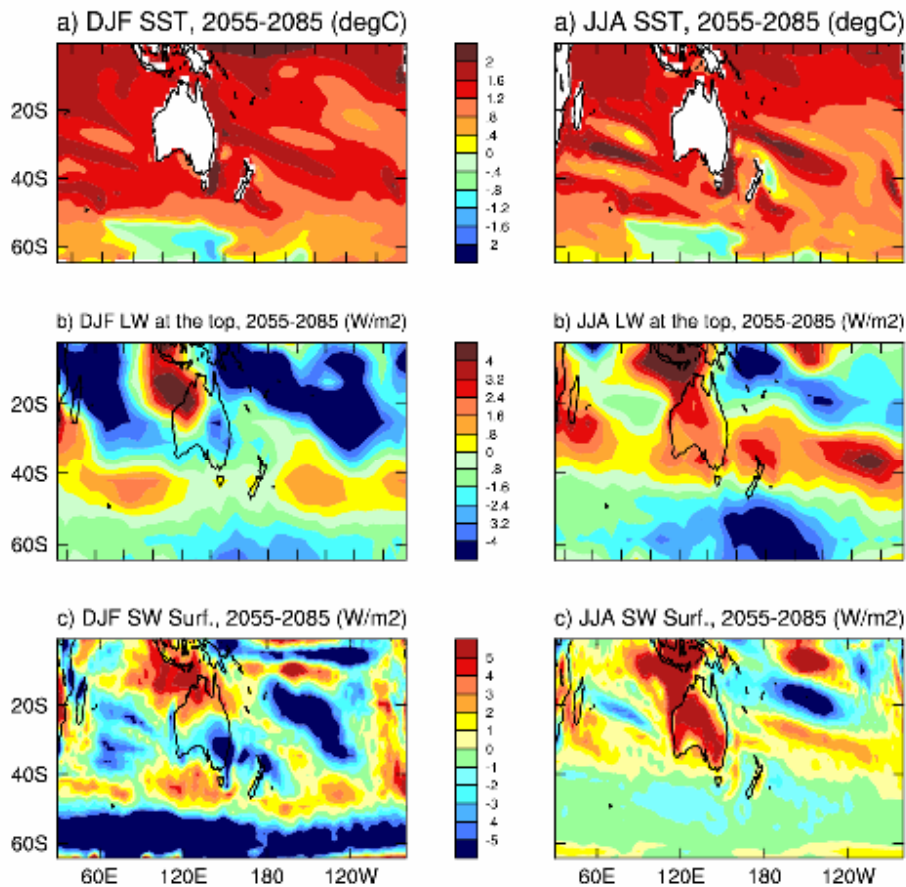


Figure 5.12: Changes averaged over a 31-year period between 2055-2085 of (a) SST ( $^{\circ}\text{C}$ ), (b) longwave radiation at the top of the atmosphere ( $\text{W m}^{-2}$ ), and (c) surface shortwave radiation ( $\text{W m}^{-2}$ ). Left column is for summer and right column is for winter.

#### 5.4.2 Winter rainfall change

In a lower-resolution version of the CSIRO model, Cai et al. (2003a) showed that the rainfall decrease over SWWA is linked with an upward SAM trend induced by increasing  $\text{CO}_2$ . In the present model, according to Fig. 5.10 (right column), an upward trend of the SAM should lead to the winter rainfall reduction over southern Australia. This is indeed the case, and is rather consistent in the IPCC-AR4 models (Fig. SPM7 of Alley et al., 2007).

For SEA, both an upward SAM trend (right column, Fig. 5.11a) and the Tasman Sea warming (right column, Fig. 5.12a) should each contribute to a rainfall increase at least along the east Australia coast (though weaker than that in summer), according to what is shown in the right column of Figs. 5.7a and 5.10a. Off the east coast a strong rainfall

increase is generated due to the large Tasman Sea warming. However, inland from the coast winter rainfall actually decreases. This is because of a strong tropical impact, where warming in the far western Pacific and the EIO is less than that in the western IO or the eastern Pacific (right column, Fig. 5.12a). This gives rise to a pattern of change reminiscent of a positive phase of an IOD and El Niño in terms of impacts on SEA rainfall. Figs. 5.8 and 5.9 (right column) shows that an El Niño and/or a positive IOD will weaken SEA rainfall. Indeed, the effect from the positive IOD-like change is so strong that it leads to a net rainfall reduction over most of SEA. This is reinforced by a consistent decrease in outgoing longwave radiation (right column, Fig. 5.12b) at the top of the atmosphere and an increase in surface shortwave radiation (right column, Fig. 5.12c) stretching from the EIO to SEA.

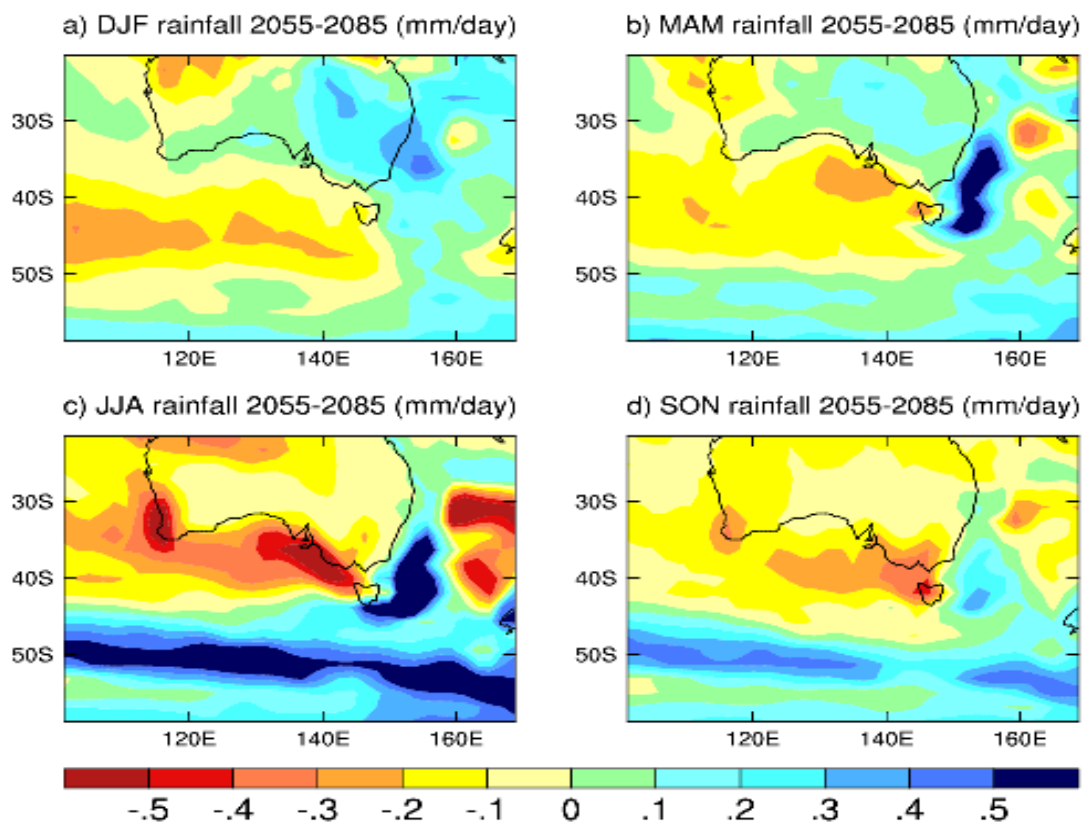


Figure 5.13: Rainfall changes (in  $\text{mm day}^{-1}$ ) for all seasons, (a) DJF, (b) MAM, (c) JJA, and (d) SON.

Thus the IO warming pattern plays an important role in driving the winter rainfall change throughout SEA. An examination reveals that as in many other models, the Asian monsoons increase under a warming climate. The stronger monsoon drives more powerful winds across the IO, contributing to weaker warming in the EIO, which in turn leads to a decrease over SEA rainfall, similar to a positive IOD.

It is interesting to note that the strengthening monsoon takes place despite the feature of an El Niño-like pattern. Historically the influence in the EIO sector from ENSO and Asian monsoon tend to oppose each other, with El Niño conditions generally associated with weaker monsoons. However, there is evidence indicating that this coupling of the Asian monsoon and ENSO systems has begun to break down over recent decades (Kumar et al., 1999). The weakening of this relationship can be induced by systematic changes in the pattern of Pacific SST anomalies during El Niño events (Kumar et al., 1999), but in our model is by a greater transient greenhouse warming of the Eurasian landmass than that over the ocean, which has enabled ENSO-independent strengthening of the Asian monsoon, as shown in other models (Ashrit et al., 2001; Hu et al., 2000; Shi et al., 2008a). This is a feature during the transient period while CO<sub>2</sub> is increasing; after CO<sub>2</sub> stabilises the ocean warming will gradually catch up. Thus, until CO<sub>2</sub> stabilization is achieved, the Asian monsoon will strengthen further, and maintain an IOD-like zonal SST gradient.

Although we have focused on winter and summer seasons, the change and the dynamics in MAM and SON are rather similar to those in DJF and JJA respectively. This is partially illustrated in Fig. 5.13.

## 5.5 Summary and discussion

The majority of the IPCC-AR4 global climate models projects a future rainfall increase in summer but a reduction in winter over the SEA region. In this study, we examine the governing dynamics using the CSIRO Mk3.0 climate model, which participates in the IPCC-AR4 projection and produces the seasonal contrast of rainfall change. We find that the summer rainfall increase is caused by the large Tasman Sea warming promoting convection and an upward SAM trend with easterly anomalous flows towards the SEA coast, which are all conducive to rainfall. The rainfall increase resulting from these two processes dominate a rainfall-decreasing effect resulting from an El Niño-like warming pattern in the equatorial Pacific Ocean. In winter, the Tasman Sea warming and an upward SAM trend both have an impact for a rainfall increase along the coast, but the effect of a warming pattern in the Indo-Pacific dominates, with a change in zonal SST gradients in the southern tropical IO resembling that of an IOD suppressing rainfall over SEA; the resultant impact is a net reduction in SEA rainfall, but over the Tasman Sea, a huge rainfall increase is generated as a consequence of the large Tasman Sea warming.

Our result highlights the importance of realistically simulating the teleconnection between Australian rainfall and major climate drivers. Although the model rainfall teleconnection with the SAM and the IOD is realistic, the model suffers from a Pacific cold tongue bias with the warm pool that is too far west and is too equatorially confined. We show that this generates an unrealistic relationship between NWA summer rainfall and ENSO, with a decrease in NWA summer rainfall during El Niño events. As a consequence, an El Niño-like warming pattern is associated with a projected summer rainfall increase over NWA. It is not clear whether the NWA rainfall decrease will be generated without the model bias. Over the eastern Australia, the model ENSO-rainfall teleconnection is too weak, particularly over the south eastern regions. This means that a

summer rainfall reduction due to the El Niño-like warming pattern is weaker than otherwise expected. Thus, without this model bias, the projected summer rainfall increases over SEA might not be as large.

Thus our work underscores the importance of resolving the long lasting issue of the Pacific cold tongue bias in projecting future climate. Only through a realistic simulation of ENSO, with its telenconnection with Australia rainfall, can the relative importance of ENSO in driving climate variability and therefore climate change be represented. As highlighted by Shi et al. (2008a, 2008b), this needs to be treated as a priority area as it is crucial for reducing the uncertainty of future Australia rainfall projection.

## Chapter 6: Conclusions

The present study is motivated by the need to understand dynamics of Australian rainfall trends over the past 50 years. In most regions, rainfall has been declining. These regions include SEA, south-eastern Queensland, and SWWA. Apart from SWWA, the reduction appears to be more severe since 1980s. If these trends continue, it would have significant implications for the nation's water resources. The water shortage across Australia has aroused a surge of research interests and investments with strong regional focus. For example, the IO Climate Initiative was set up to explore the dynamics of SWWA rainfall decline, and the South East Australian Climate Initiative was established to examine the impact of climate change on the region's changing climate baseline. One exception is the NWA, where rainfall has been increasing, which may represent an opportunity, if it persists, therefore the dynamics must be investigated.

Upon a careful and comprehensive literature review, three key areas have been identified in which a contribution can be made, and in which progress will provide an Australia-wide assessment:

- Does the oceanic connection between variability in the Pacific Ocean and in the IO also precondition the IOD and hence is linked to the severe rainfall downturn since 1980s?
- What are the dynamics governing variability and trends of rainfall over NWA?
- What is the future of Australian rainfall, taking into account of possible changes in climate drivers and in the ocean-atmosphere circulation?

### 6.1 Indo-Pacific oceanic teleconnection

Previous studies have shown that through atmospheric teleconnection, the Pacific El Niño-like condition since 1980 have a strong influence on IOD, making the occurrence more frequent and the intense, which in turn influence Australian rainfall. The teleconnection is conducted through wind anomalies associated with the longer and more protracted El Niño events, raising the thermocline so that it is more conducive to development of IOD events. The focus is on the oceanic teleconnection. Although the ENSO discharge/recharge signals have long been known to transmit into the IO, the involvement of the NP is not clear. We reveal a previously un-noticed subtropical NP pathway. NP Rossby waves associated with ENSO impinge on the western boundary and move equatorward along the "ray-path" of Kelvin-Munk waves, and reflect as equatorial Kelvin waves. En-route to the equator, the waves is reinforced by wind stress anomalies associated with ENSO. The reflected equatorial Kelvin waves impinge on the Australasian continent and move poleward along the northern WA coast as coastally-trapped waves, radiating Rossby waves into the south IO. The robustness of the amount of energy that leaves the Pacific via each of the pathway is then examined using the SODA-POP reanalysis and a multi-century coupled model control experiment. We find that in the pre-1980 period, little ENSO signal is transmitted to the IO and does not involve the subtropical NP pathway. Such multidecadal variability is periodically produced by the climate model. Examinations reveal that when ENSO is weak as

determined by Niño3.4, their meridional extent is narrow; the associated discharge-recharge does not involve the subtropical NP pathway.

The longer and more protracted El Niño events since 1980 means that more upwelling Rossby waves transmit to the IO, lifting the thermocline, and contributing to changing IOD properties. We have also shown that this feature is essential for explaining the temperature trend of the IO over the forty years.

## **6.2 Dynamics of NWA rainfall variability and trend**

As mentioned above, there has been an increase in rainfall over NWA since 1950, occurring mainly during the SH summer season. In an environment where decadal-scale droughts have plagued most of the country, continued upward trends in NWA rainfall may provide a source of future water resources. There have been few studies on NWA rainfall. A recent study using 20th century multi-member ensemble simulations in a global climate model forced with and without increasing anthropogenic aerosols suggests that the rainfall increase is attributable to increasing northern Hemisphere aerosols. One implication is that as aerosols decrease, the trend will diminish. Our analysis investigates the dynamics of the observed trend toward increased rainfall and compares the dynamics of the observed trend with that in the model.

We find that the observed positive trend in rainfall is projected onto two modes of variability. The first mode is associated with an anomalously low MSLP off NWA instigated by the enhanced SST gradients towards the coast. The associated cyclonic flows bring high moisture air to northern Australia, leading to an increase in rainfall. The second mode is associated with an anomalously high MSLP over much of the Australian continent; the anticyclonic circulation pattern with northwesterly flows west of 130°E and generally opposite flows in northeastern Australia, determine that when rainfall is anomalously high, west of 130°E, rainfall is anomalously low east of this longitude. The sum of the upward trends in these two modes compares well to the observed increasing trend pattern.

The modeled rainfall trend, however, is generated by a different process. The model suffers from an equatorial cold-tongue bias: the tongue of anomalies associated with ENSO extends too far west into the EIO. Consequently, there is an unrealistic relationship in the SH summer between Australian rainfall and EIO SST: the rise in SST is associated with an increasing rainfall over NWA. In the presence of increasing aerosols, a significant SST increase occurs in the eastern tropical IO. As a result, the modeled rainfall increase in the presence of aerosol forcing is accounted for by these unrealistic relationships. It is not clear whether, in a model without such defects, the observed trend can be generated by increasing aerosols. Thus, the impact of aerosols on Australian rainfall remains an open question, and can only be assessed with the model deficiencies overcome.

### **6.3 Australian rainfall under a changing climate**

The course of work coincides with the IPCC AR4 process. The majority of climate models in the IPCC AR4 project a future rainfall increase in summer but a reduction in SEA. The model dynamics governing these changes have not been explored. This is examined using outputs of a participating model, the CSIRO Mk3 model.

One associated common feature in the IPCC AR4 is the warming rate in the Tasman Sea that is fastest of the Southern Hemisphere. Therefore, a focus is placed on the dynamics and impact of the fast warming rate. We find that an upward trend of the SAM in response to increasing atmospheric CO<sub>2</sub> concentration, the associated trends of surface winds and the curl cause a spin-up of entire southern midlatitude ocean circulation including a southward strengthening of the EAC. The intensified EAC advects more warm water poleward, generating a warming rate in the Tasman Sea that is greatest in the SH. The fast Tasman Sea warming is conducive to a rainfall increase along the east coast.

The summer rainfall increase is consistent with a large Tasman Sea warming promoting convection, and with an upward trend of the SAM promoting flows towards the SEA coast. The rainfall increase resulting from these two processes dominate a weak rainfall decrease resulting from an El Niño-like warming pattern in the equatorial Pacific Ocean. In winter, the effect of a Tasman Sea warming and an upward SAM trend lead to an increase in SEA rainfall, however, the impact of the Indo-Pacific warming pattern dominates: in the IO the warming pattern resembles an IOD in terms of SST gradients, leading to a net reduction in SEA rainfall. Rainfall over NWA is projected to decrease, as a result of an unrealistic relationship between ENSO, and the El Niño-like warming pattern in the equatorial Indo-Pacific. The importance of resolving the model Pacific cold tongue bias in reducing the uncertainty is highlighted.

Thus our work underscores the importance of resolving the long lasting issue of the Pacific cold tongue bias in projecting future climate. Only through a realistic simulation of ENSO, with its teleconnection with Australia rainfall, can the relative importance of ENSO in driving climate variability and therefore climate change be represented. This must be treated as a priority area as it is crucial for reducing the uncertainty of future Australia rainfall projection.

### **6.4 Future directions**

There are many avenues whereby the present study can be extended. Some of these have been outlined at the end of each chapter. For example, improvement of Indo-Pacific dynamical representations in climate models for realistic simulation of Australian rainfall teleconnection. One which is most relevant is a diagnosis of the behaviour IOD in a warming climate in models that realistically reproduce IOD variability. Climate models seem to converge on a positive IOD-like warming pattern as global warming continues. Since the mean state is the average of interannual variability, it would mean that positive

IOD events are becoming more frequent and/or more intense. Thus, it is necessary to understand the dynamics behind such a change and subsequent impacts Australian rainfall. The highly relevant context was the 2006 and 2007 cases. As this study is at the writing stage, we realised that we had two consecutive positive IOD events, one in 2006 and one in 2007, and the 2007 episode occurred in an arguably unprecedented setting, i.e., in conjunction with a La Niña event. Is it a manifestation of global warming?

## References

Allan R., Chambers, D., Drosowsky, W., Hendon, H., Latif, M., Nicholls, N., Smith, I., Stone, R., & Tourre, Y. (September 2001). Is there an Indian Ocean dipole, and is it independent of the El Niño - Southern Oscillation? *CLIVAR Exchanges Newsletter*.

Alley, R., et al (2007), *Climate change 2007: The physical science basis, summary for policymakers*, 18 pp., World Meteorol. Organ., Geneva, Switzerland.

Alory, G., Wijffels, S. & Meyers G. (2007). Observed temperature trends in the Indian Ocean over 1960-1999 and associated mechanisms, *Geophys. Res. Lett.*, 34, L02606, doi:10.1029/2006GL028044.

Annamalai, H., Potemra, J., Murtugudde, R., & McCreary J.P. (2005). Effect of preconditioning on the extreme climate events in the tropical Indian Ocean. *J. Climate*, 18, 3450–3469

Ansell T. J., Reason, C. J. C., Smith, I.N. (2000). Evidence for decadal variability in southern Australian rainfall and relationships with regional pressure and sea surface temperature, *International Journal of Climatology*, 20, 1113-1129.

Ashok, K., Behera, S. K., Rao, S. A., Weng, H. & Yamagata T. (2007a). El Niño Modoki and its possible teleconnection, *J. Geophys. Res.*, 112, C11007, doi:10.1029/2006JC003798

———, Nakamura, H., & Yamagata, T. (2007b). Impacts of ENSO and Indian Ocean Dipole events on the southern hemisphere storm track activity during austral winter, *J. Climate*, 20(13), 3147–3163.

———, Guan, Z., & Yamagata, T. (2003). Influence of the Indian Ocean Dipole on the Australian winter rainfall, *Geophys. Res. Lett.*, 30, 1821, doi:10.1029/2003GL017926.

Ashrit, R. G., Kumar, K. R., & Kumar, K. K. (2001). ENSO-monsoon relationships in a greenhouse warming scenario. *Geophys. Res. Lett.* 28, 1727–1730.

Baldwin, M. P. (2001). Annular Modes in Global Daily Surface Pressure. *Geophys. Res. Lett.*, 28, 4115-4118

Barnett, T. P. (1983). Interaction of the Monsoon and Pacific trade wind system at interannual time scales. Part I ). The equatorial zone. *Month. Weath. Rev.* 111(4), 756-773.

Cadet D., (1985). The Southern Oscillation over the Indian Ocean. *J. Climatol*, 5, 189–210

- Cai, W., & Cowan T., (2007). Trends in Southern Hemisphere circulation in IPCC AR4 models over 1950-1999: Ozone-depletion vs. greenhouse forcing. *J. Climate*, 20 (4), 681-693
- , Cowan, T., Dix, M., Ribbe, R., Rotstayn, L., Shi, G. & Wijffels, S. (2007), Anthropogenic aerosol forcing and the structure of temperature trends in the southern Indian Ocean, *Geophys. Res. Lett.*, 34, L14611, doi:10.1029/2007GL030380
- , & Cowan T., (2006). SAM and regional rainfall in IPCC AR4 models: Can anthropogenic forcing account for southwest western Australian winter rainfall reduction? *Geophys. Res. Lett.*, 33, L24708, doi:10.1029/2006GL028037.
- , (2006). Antarctic ozone depletion causes an intensification of the southern ocean super-gyre circulation. *Geophys. Res. Lett.*, 33 (3): L03712, 10.1029/2005GL024911.
- , Bi, D., Church, J., Cowan T., Dix M., and Rotstayn L. (2006). Pan-oceanic response to increasing anthropogenic aerosols: impacts on the Southern Hemisphere oceanic circulation. *Geophys. Res. Lett.*, 33, L21707, doi:10.1029/2006GL027513.
- Shi G., and Li, Y. (2005a) Multidecadal fluctuations of winter rainfall over southwest Western Australia simulated in the CSIRO Mark 3 coupled model, *Geophys. Res. Lett.*, 32, L12701, doi: 10.1029/2005GL022712.
- , Shi, G., Cowan, T., Bi, D., & Ribbe, J. (2005b). The response of the Southern Annular Mode, the East Australian Current, and the southern mid-latitude ocean circulation to global warming. *Geophys. Res. Lett.*, 32 (23): L23706, doi:10.1029/2005GL024701.
- , Meyers, G., Shi, G. (2005c). Transmission of ENSO signal to the Indian Ocean. *Geophys. Res. Lett.*, 32, L05616
- , Hendon, H. H., & Meyers G. (2005d). An Indian Ocean Dipole in the CSIRO coupled climate model. *J. Climate*, 18, 1449--1468.
- , McPhaden, J. M. & Collier M.A. (2004). Multidecadal fluctuations in the relationship between equatorial Pacific heat content anomalies and ENSO amplitude. *Geophys. Res. Lett.*, 31, L01201, doi:10.1029/2003GL018714.
- , Whetton, P. H., & Karoly D. J. (2003a). The response of the Antarctic Oscillation to increasing and stabilized atmospheric CO<sub>2</sub>. *J. Climate*, 16 (10): 1525-1538.
- , Collier, M. A., Gordon, H. B., & Waterman, L. J. (2003b). Strong ENSO variability and a Super-ENSO pair in the CSIRO mark 3 coupled climate model. *Mon. Wea. Rev.*, 131 (7): 1189-1210.

———, & Watterson, I.G. (2002). Modes of interannual variability of the Southern Hemisphere circulation simulated by the CSIRO climate model. *J. Climate*, 5:1159-1174

———, & Whetton P.H. (2001), A time-varying greenhouse warming pattern and the tropical-extratropical circulation linkage in the Pacific Ocean, *J. Clim*, 14, 3337–3355

———, Whetton, P. H., Pittock A. B. (2000). Fluctuations of the relationship between ENSO and northeast Australia rainfall. *Clim. Dynamics*.17, 421-432.

Carton, J. A., & Giese S. B. (2007), SODA: A Reanalysis of Ocean Climate. *Mon. Wea. Rev.*, accepted.

Chambers, D. P., Tapley, B. D., & Stewart, R. H. (1999). Anomalous warming in the Indian Ocean coincident with El Niño. *J. Geophys. Res.*, 104, 3035-3047.

Chelton, D. B., & Schlax M.G. (1996). Global Observations of Oceanic Rossby Waves. *Science*, 272, 234-238.

Cipollini, P., Cromwell D., Challenor P. G. & Raffaglio S. (2001). Rossby waves detected in global ocean colour data. *Geophys. Res. Lett.*, 28, 323-326.

Clarke, A. J. & Liu X. (1994). Interannual sea level in the northern and eastern Indian Ocean. *J. Phys. Oceanogr.* 24, 1224-1235.

———, (1991), On the reflection and transmission of low-frequency energy at the irregular western Pacific Ocean boundary. *J. Geophys. Res.*, 96, 3289--3305.

Clarke, G. K. C., Treut H. L., Lindzen R. S., Meleshko V. P., Mugara R. K., Palmer T. N., Pierrehumbert R. T., Sellers P. J., & Trenberth K. E. (2001) *Physical climate processes and feedbacks, in Climate Change 2001: The Scientific Basis. Contribution of Working Group I to the Third Assessment Report of the Intergovernmental Panel on Climate Change (IPCC)*, edited by J. T. Houghton, Y. Ding, D. J. Griggs, M. Noguer, P. J. van der Linden, X. Dai, K. Maskell, & C. A. Johnson, Cambridge Univ. Press, Cambridge, United Kingdom, 417–470.

Cubasch, U., Meehl G. A., Boer G. J., Stouffer R. J., Dix M., Noda A., Senior C. A., Raper S., & Yap K.S. (2001). Projections of future climate change. In: Houghton, J.T., Ding, Y., Griggs, D.J., Noguer, M., van der Linden, P., Dai, X., Maskell, K. & Johnson, C.I. (Eds.). *Climate Change 2001: The Scientific Basis. Contribution of Working Group I to the 3rd Assessment Report of the Intergovernmental Panel on Climate Change*. Cambridge University Press, Cambridge, UK, pp. 525-582.

Davis, R. E. (1976), Predictability of sea surface temperature and sea level pressure anomalies over the North Pacific Ocean, *J. Phys. Oceanogr.*, 6, 249– 266.

Duffy, P. B., Eltgroth, P., Bourgeois, A. J., & Caldeira K. (1995), Improved representation of vertical profiles of temperature and bomb radiocarbon in GFDL ocean general circulation, *Geophys. Res. Lett.*, 22, 1065–1068.

Edgar G. J. (1997). Australian Marine Life. Reed Books, Sydney.

England, M. H., Ummenhofer, C. C., & Santoso, A. S., (2006) Interannual rainfall extremes over Southwest Western Australia linked to Indian Ocean climate variability, *J. Climate*, 19, 1948–1969, DOI: 10.1175/JCLI3700.1.

Enfield, D. B., & Mestas-Nun˜ez, A.M. (1999). Multiscale variabilities in global sea surface temperatures and their relationships with tropospheric climate patterns. *J. Climate*, 12, 2719–2733.

Feng, M., & Meyers G. (2003). Interannual variability in the tropical Indian Ocean: A two-year time scale of Indian Ocean Dipole. *Deep-Sea Res.*, 50, 2263–2284.

Fyfe, J. C., Boer G. J. & Flato G. M. (1999). The Arctic and Antarctic Oscillations and their projected changes under global warming. *Geophys. Res. Lett.*, 26, 1601–1604.

Gent, P. R. & McWilliams, J. C. (1990), Isopycnal mixing in ocean circulation models. *J. Phys. Oceanogr.*, 20, 150–155.

Gille, S. T. (2002). Warming of the Southern Ocean since the 1950s. *Science*, 295, 1275–1277.

Gillet, N. P., & Thompson, D. W. J. (2003). Simulation of recent Southern Hemisphere climate change, *Science*, 302, 273–275.

Godfrey, J. S. (1989). A Sverdrup model of the depth-integrated flow for the world ocean allowing for island circulations, *Geophys. Astrophys. Fluid Dyn.*, 45, 89–112.

———, (1975). On ocean spindown I: A linear experiment. *J. Phys. Oceanogr.*, 5, 399–409.

Gong, D., & Wang S. (1999). Definition of Antarctic Oscillation index. *Geophys. Res. Lett.*, 26, 459–462

Gordon, H.B., Rotstayn, L.D, McGregor, J.L., Dix, M.R., Kowalczyk, E.A., O'Farrell, S.P., Waterman, L.J., Hirst, A.C., Wilson, S.G., Collier, M.A., Watterson, I.G., & Elliott, T.I. (2002). *The CSIRO Mk3 Climate System Model, CSIRO Division of Atmospheric Research technical paper No. 60*. 130pp.

Gregory, D., & Rowntree, P. R. (1990). A mass flux convection scheme with presentation of cloud ensemble characteristics and stability dependent closure. *Mon. Wea. Rev.*, 118, 1483–1506.

Griffies, S. M. (1998). The Gent–McWilliams skew flux. *J. Phys. Oceanogr.*, 28, 831–841.

———, Gnanadesikan, A., Pacanowski, R. C., Larichev, V. D., Dukowicz, J. K., & Smith, R. D. (1998). Isonutral diffusion in az-coordinate ocean model. *J. Phys. Oceanogr.*, 28, 805–830.

Hall, A. & Visbeck, M. (2002). Synchronous Variability in the Southern Hemisphere Atmosphere, Sea Ice, and Ocean Resulting from the Annular Mode. *J. Climate*, 15, 3043–3057

Hartmann, D. L. & Lo F. (1998). Wave-driven zonal flow vacillation in the Southern Hemisphere, *J. Atmos. Sci.*, 55, 1303–1315.

Harrison, D. E., & Vecchi G. A. (1999). On the termination of El Niño, *Geophys. Res. Lett.*, 26, 1593–1596

———, Larkin, N. K. (1998). El Niño–Southern Oscillation sea surface temperature and wind anomalies, 1946–1993. *Rev. Geophys.*, 36, 353–399.

Harris, G., Davies P., Nunez M., & Meyers G. (1988). Interannual variability in climate and fisheries in Tasmania. *Nature*, 333, 754–757

Hastenrath, S., Nicklis, A., & Greischar, L. (1993): Atmospheric hydropheric mechanisms of climate anomalies in the western equatorial Indian Ocean. *J. Geophys. Res.*, 98(C11), 20, 219–20,235.

Hartmann, D. L. (1994). *Global Physical Climatology*. San Diego, CA, Academic Press.

Hendon, H. H., Thompson D. W. J., & Wheeler M. C. (2007). Australian rainfall and surface temperature variations associated with the Southern Hemisphere Annular Mode. *J. Climate* 20, 2452–2467.

Hendon, H.H. (2003). Indonesian rainfall variability: impact of ENSO and local air-sea interaction. *J. Climate* 16, 1775–1790

Hu, Z.-Z., Latif, M., Roeckner, E., & Bengtsson, L. (2000). Intensified Asian summer monsoon and its variability in a coupled model forced by increasing greenhouse gas concentrations. *Geophys. Res. Lett.* 27, 2681–2684.

Hurrell, J.W., & H. van Loon (1994). A modulation of the atmospheric annual cycle in the Southern Hemisphere. *Tellus*, 46A, 325–338

——, & Trenberth, K.E. (1996). Satellite versus surface estimates of air temperature since 1979. *J. Climate*, 9, 2222-2232.

IOCI (2002). *Climate variability and change in south west Western Australia*. Indian Ocean Climate Initiative Panel, 34pp

IPCC (2007) Summary for Policymakers. In, *Climate Change 2007: The Physical Science Basis*. Contribution of Working Group I to the Fourth Assessment Report of the Intergovernmental Panel on Climate Change [Solomon, S., D. Qin, M. Manning, Z. Chen, M. Marquis, K. B. Averyt, M. Tignor, & H. L. Miller (eds.)]. Cambridge University Press, Cambridge, UK and New York, NY, USA.

Jin, F.-F. (2001). Low-frequency modes of tropical ocean dynamics. *J. Climate*, 14, 3874–3880.

—— (1997a). An equatorial ocean recharge paradigm for ENSO. Part I: Conceptual model. *J. Atmos. Sci.*, 54, 811–829.

—— (1997b). An equatorial ocean recharge paradigm for ENSO. Part II). Stripped-down coupled model. *J. Atmos. Sci.*, 54, 830–847.

Kalnay E., Kanamitsu M., Kistler R., Collins W., Deaven D., Gandin L., Iredell M., Saha S., White G., Woolen J., Zhu Y., Chelliah M, Ebisuzaki W, Higgins W., Janowiak, K. C. Mo, C. Ropelewski, J. Wang, A. Leetma, R. Reynolds, R. Jenne, & Joseph, J. D. (1996). The NMC/NCAR 40-year reanalysis project, *Bull. Amer. Met. Soc.*, 77 (3), 437–471

Karoly, D. J. (1990). The role of transient eddies in low-frequency zonal variations of the Southern Hemisphere circulation. *Tellus*, 42A, 41–50.

Kawamura, R. (1994). A rotated EOF analysis of global sea surface temperature variability with interannual and interdecadal scales. *J. Phys. Oceanogr.*, 24, 707–715.

Kessler, W.S. (2002): Mean three-dimensional circulation in the northeast tropical Pacific. *J. Phys. Oceanogr.*, 32, 2457-2471

Kidson, J.W. (1999). Principal modes of Southern Hemisphere low-frequency variability obtained from NCEP-NCAR reanalyses. *J. Climate* 12(9)). 2808–2830

——, (1988a). Indices of the Southern Hemisphere zonal wind. *J. Climate*, 1, 183–194.

——, (1988b). Interannual variations in the Southern Hemisphere circulation. *J. Climate*, 1, 1177–1198.

Kiladis, G. N., & Diaz, H. F. (1989). ‘Global climatic anomalies associated with extremes extremes in the Southern Oscillation’, *J. Climate*, 12, 1854-1992.

Klein, S. A., Soden B. J., & N.-C. Lau (1999) Evidence for a tropical atmospheric bridge. *J. Climate*, 12, 917–932.

Koslow A & Thresher R. E. (1999). *Climate and Fisheries on the south-east Australian continental shelf and slope*. Tech. Rep. FRDC Project Number 96/111, CSIRO Marine Research, Hobart.

Kowalczyk, E. A., Garratt, J. R., & Krummel, P. B. (1991). *A soil-canopy scheme for use in a numerical model of the atmosphere: 1D stand alone model*. CSIRO Division of Atmospheric Research Tech. Paper 23, 60 pp.

———, ———, & ——— (1994). *Implementation of a soil-canopy scheme into the CSIRO GCM: Regional aspects of the model response*. CSIRO Division of Atmospheric Research Tech. Paper 32, 59 pp

Kumar, K. K., Rajagopalan, B., & Cane, M. A. (1999). On the weakening relationship between the Indian Monsoon and ENSO. *Science*, 284, 2156–2159.

Kushner, P. J., Held, I. M., & Delworth, T. L. (2001). Southern Hemisphere atmospheric circulation response to global warming. *J. Climate.*, 14, 2238-2249.

Lanzante, J. R. (1996). Lag relationships involving tropical sea surface temperatures. *J. Climate*, 9, 2568–2578.

Larkin, N. K., & Harrison, D. E. (2001). Tropical Pacific ENSO Cold Events, 1946-95: SST, SLP and Surface Wind Composite Anomalies, *J. Climate*, 14(10), 3904-3930.

Limpasuvan, V. & Hartmann D. L. (1999). Eddies and the annular modes of climate variability, *Geophys. Res. Lett.*, 26, 3133-3136

Marshall, G.J., Stott, P.A., Turner, J., Connolley, W. M., King, J.C., & Lachlan-Cope, T.A. (2004). Causes of exceptional atmospheric circulation changes in the Southern Hemisphere. *Geophys. Res. Letters*, 31, doi: 10.1029/2004GL019952.

———, (2003). Trends in the Southern Annular Mode from Observational and Reanalyses. *J. Climate*, 16, 4134.

Masumoto, Y., & Meyers G. (1998). Forced Rossby waves in the southern tropical Indian Ocean. *J. Geophys. Res.*, 103, 27589--27602.

McBride, J.L. & Nicholls N. (1983). Seasonal relationships between Australian rainfall and the Southern Oscillation. *Mon. Wea. Rev.*, 111, 1998-2004.

McCreary J. P. Jr., (1983). A model of tropical ocean-atmosphere interaction. *Mon. Wea. Rev.*, 111, 370-387.

McGregor, J. L. (1993). Economical determination of departure points for semi-lagrangian models. *Mon. Wea. Rev.*, 121, 221–230.

McPhaden, M. J., Busalacchi A. J., Cheney R., Donguy J. R., Gage K.S., Halpern D., Ji M., Julian P., Meyers G., Mitchum G.T., Niiler P.P., Picaut J., Reynolds R.W., Smith N., & Takeuchi K. (1998). The Tropical Ocean-Global Atmosphere (TOGA) observing system: A decade of progress, *J. Geophys. Res.*, 103, 14,169-14,240.

McPhaden, M.J. & Zhang, D. (2002). Slowdown of the meridional overturning circulation in the upper Pacific Ocean. *Nature*, 415, 603-608.

Meehl, G. A., & Washington W. M. (1995). Cloud albedo feedback and the super greenhouse effect, *Clim. Dyn.*, 11, 399–411.

Meinen C. S. & McPhaden M. J. (2000). Observations of warm water volume changes in the equatorial Pacific and their relationship to El Niño and La Niña. *J. Climate*, 13, 3551-3559.

Mestas-Nuñez, A. M., & Enfield D. B.(2001). Eastern equatorial Pacific SST variability: ENSO and non-ENSO components and their climatic associations. *J. Climate* 14, 391-402.

Meyers, G. (1996). Variation of the Indonesian throughflow and the El Niño Southern Oscillation, *J. Geophys. Res.*, 101, 12,255–12,263.

———, Phillips, H., Smith, N. R., & Sprintall, J., (1991). Space and time scales for optimum interpolation of temperature-tropical Pacific Ocean. *Progress in Oceanography*, 28, Pergamon, 189—218.

Mitchell, J. F. B., Davis, R. A., Ingram, W. J. & Senior, C. A. (1995). On surface temperature, greenhouse gases, and aerosols: Models and observations. *J. Climate*, 8, 2364–2386.

Murphy, J. M., & Mitchell, J. F. B. (1995). Transient Response of the Hadley Centre Coupled Ocean-Atmosphere Model to Increasing Carbon Dioxide. Part II: Spatial and Temporal Structure of Response. *J. Climate*, 8, 57–80.

Nicholls, N. (1989) Sea surface temperature and Australian winter rainfall. *J. Climate*, 2, 965-973.

———, & Woodcock, F.(1981). Verification of an empirical longrange weather forecasting technique. *Q J Q Meteorol Soc*, (111). 973-976

Nicholson, S. E. (1997). An analysis of the ENSO signal in the tropical Atlantic and western Indian Oceans. *Int. J. Climatol.*, 17, 345–375.

North, G. R., Bell T. L., Cahalan R. F. & Moeng F. J. (1982). Sampling errors in the estimation of empirical orthogonal functions. *Monthly Weather Review*, 110, 699-706.

Pan, Y. H., & Oort, A.H. (1983). Global climate variations connected with sea surface temperature anomalies in the eastern equatorial Pacific Ocean for the 1958–73 period. *Mon. Wea. Rev.*, 111, 1244–1258.

——, & ——, (1990). Correlation analyses between sea surface temperature anomalies in the eastern equatorial Pacific and the world ocean. *Climate Dyn.*, 4, 191–205.

Papoulis, A. (1965). *Probability, Random Variable and Stochastic Processes*. McGraw-Hill, New York

Peixoto, J. P. & Oort A.H. (1992) *Physics of Climate*. American Institute of Physics.

Pitman, A. J., Narisma, G. T. , Pielke, R. A., & Holbrook, N. J. (2004). Impact of land cover change on the climate of southwest Western Australia, *J. Geophys. Res.*, 109, D18109, doi: 10.1029/2003JD004347

Pittock B. (1975). Climate change and patterns of variation in Australian rainfall. *Search*, 6, 498-504.

Pittock B, Ed. (2003). *Climate Change: An Australian Guide to the Science and Potential Impacts*. Australian Greenhouse Office, Canberra.

Philander, S. G. H. (1990). *El Niño, La Niña, and the Southern Oscillation*. International Geophysics Series, No. 46, Academic Press.

——, & W. J. Hurlin (1988). The heat budget of the tropical Pacific Ocean in a simulation of the 1982–83 El Niño. *J. Phys. Oceanogr.*, 18, 926–931.

——, T. Yamagata, & R. C. Pacanowski (1984). Unstable air–sea interactions in the Tropics. *J. Atmos. Sci.*, 41, 603–613.

Potemra, J.T, Hautala, S.L., & Sprintall, J. (2002). Interaction between the Indonesian seas and the Indian Ocean in observations and numerical models. *J. Phys. Oceanogr.*, 32 (6), 1838–1854.

——, (2001). Contribution of equatorial Pacific winds to southern tropical Indian Ocean Rossby waves. *J. Geophys. Res.*, 106, 2407-2422.

Qiu, B., & Chen, S. (2006). Decadal variability in the formation of the North Pacific Subtropical Mode Water: Oceanic versus atmospheric control. *J. Phys. Oceanogr.*, 36,

Rao, S., A., Behera S. K., Masumoto Y. & Yamagata T. (2002). Interannual variability in the subsurface Indian Ocean with special emphasis on the Indian Ocean Dipole. *Deep Sea Res.-II*, 49, 1549-1572.

Rashid, H., & Simmonds A. I. (2004). Ebby-zonal flow interactions associations with the Southern Hemisphere annular mode. Results from NCEP-DOE reanalysis and a quasi-linear model. *J. Atmos. Sci.*, 61, 873-888.

Rayner, N. A., Horton, E. B., Parker, D. E., Folland, C. K., & Hackett, R. B. (1996). Version 2.2 of the Global sea-Ice and Sea Surface Temperature dataset, 1903–1994. *Climate Research Tech. Note CRTN74*, Hadley Centre, Met Office, Bracknell, Berkshire, United Kingdom, 25 pp.

Reason, C. J. C., Allan, R. J., Lindesay, J. A., & Ansell, T. J. (2000). ENSO and climatic signals across the Indian Ocean basin in the global context: Part I: Interannual composite patterns. *International Journal of Climatology*, 20, 1285-1327.

Ridgway, K. R., & Dunn, J. R. (2003). Mesoscale structure of the mean East Australian Current system and its relationship with topography, *Prog. Oceanogr.*, 56, 189–222.

Ropelewski, C. F., & Halpert, M. (1989). Precipitation patterns associated with the high index phase of the Southern Oscillation, *J. Climate*, 2, 268–284.

———, & —— (1987). Global and regional scale precipitation patterns associated with the El Niño/Southern Oscillation, *Mon. Wea. Rev.*, 115, 1606–1626.

Rotstayn, L.D., Cai, W., Dix, M.R. Farquhar, G.D., Feng, Y., Ginoux, P., Herzog, M., A. Ito, Penner J.E., Roderick, M.L., & Wang, M. (2007). Have Australian rainfall and cloudiness increased due to the remote effects of Asian anthropogenic aerosols? *J. Geophys. Res.*, 112, D09202, doi:10.1029/2006JD007712

———, Ryan, B. F., & Katzfey, J. J. (2000). A scheme for calculation of the liquid fraction in mixed-phase stratiform clouds in large-scale models. *Mon. Wea. Rev.*, 128, 1070–1088

Saji, N.H., Goswami, B.N., Vinayachandran, P.N., & Yamagata, T. (1999). A dipole mode in the tropical Indian Ocean. *Nature*, 401, 360–363.

———, & Yamagata, T. (2003). Possible impacts of Indian Ocean dipole mode events on global climate. *Climate Res.*, 25, 151-169.

Samuel J. M., Verdon, D. C., Sivapalan, M., Franks, S. W. (2006). Influence of Indian Ocean sea surface temperature variability on southwest Western Australian winter rainfall, *Water Resour. Res.*, 42, W08402, doi:10.1029/2005WR004672.

Sexton, D.M.H. (2001). The effect of stratospheric ozone depletion on the phase of the Antarctic Oscillation. *Geophys. Res. Lett.*, 28, 3697–3700

Shi, G., Ribbe, J., Cai, W. J., & Cowan T. (2008a), An interpretation of Australian summer and winter rainfall projection. *Geophys. Res. Lett.*, 35, L02702, doi:10.1029/2007GL032436.

——, Cai, W. J., Cowan, T., Ribbe, J., Rotstayn, L., & Dix, M. (2008b), Variability and trend of the northwest Western Australia Rainfall: observations and coupled climate modeling. *J. Climate*, 21, 2938–2959.

——, Ribbe, J., Cai, W. J., & Cowan T. (2007), Multidecadal variability in the transmission of ENSO signals to the Indian Ocean, *Geophys. Res. Lett.*, 34, L09706, doi:10.1029/2007GL029528.

Shindell, D. T., & Schmidt, G. A. (2004). Southern Hemisphere climate response to ozone changes and greenhouse gas increases, *Geophys. Res. Lett.*, 31, L18209, doi:10.1029/2004GL020724.

Shiotani, M. (1990). Low-frequency variations of the zonal mean state of the Southern Hemisphere troposphere. *J. Meteor. Soc. Japan*, 68, 461–471.

Smith, I. N. (2004). An assessment of recent trends in Australian rainfall, *Aust. Meteorol. Mag.*, 53, 163–173.

——, (1993). Indian Ocean sea-surface temperature patterns and Australian winter rainfall. *International Journal of Climatology*, 14, 287-305.

——, McIntosh, P., Ansell, T. J., Reason C.J.C., & McInnes, K. (2000). South-west Western Australian winter rainfall and its association with Indian Ocean climate variability, *International Journal of Climatology*, 20, 1913-1930.

Smith, N. R. (1995a), The BMRC ocean thermal analysis system. *Aust. Meteor. Mag.*, 44, 93--100.

—— (1995b). An improved system for tropical ocean sub-surface temperature analyses. *J. Atmos. Oceanic Technol.*, 12, 850--870.

——, (1993). Ocean modeling in a global ocean observing system, *Rev. Geophys.*, 31(3), 281–318.

Speich, S., Blanke, B., & Cai W. (2007). Atlantic meridional overturning circulation and the Southern Hemisphere super-gyre, *Geophys. Res. Lett.*, doi:10.1029/2007GL031583.

Stouffer, R. J., Manabe, S. & Bryan, K. (1989). Interhemispheric asymmetry in climate response to a gradual increase of CO<sub>2</sub>. *Nature*, 342, 660-662.

Suarez, M. J. & Schopf P.S. (1988). A delayed action oscillator for ENSO. *J. Atmospheric Sciences*, 45, 3283-3287.

Sverdrup, H.U. (1947). Winddriven currents in a baroclinic ocean with application to the equatorial currents in the eastern Pacific. *Proceedings of the National Academy of Sciences USA* 33, 318–326.

Swift, J. H. (1995). Comparing WOCE and historical temperatures in the deep southeast Pacific, *Int. WOCE Newsl.*, 18, 15– 17.

Thompson, D. W. J., & Solomon S. (2002). Interpretation of recent Southern Hemisphere climate change. *Science*, 296, 895-899.

———, & Wallace J. M. (2000). Annular Modes in the Extratropical Circulation. Part I: Month-to-month variability. *J. Climate*, 13, 1000-1016.

———, Wallace J. M., & Hegerl G. C. (2000). Annular modes in the extratropical circulation. Part II: Trends. *J. Climate*, 13, 1018-1036.

Thresher R E, Proctor C, Ruiz G, Gurney R, MacKinnon C, Walton W, Rodruiguez L & Bax N (2003). Invasion dynamics of the European shore crab, *Carcinus maenas*. *Australia. Marine Biology* 142, 867–876

Tilburg, C. E., Hurlburt, H. E., O'Brien, J.J., & Shriver J. F. (2001), The dynamics of the East Australia Current system: The Tasman Front, the East Auckland Current, and the East Cape Current, *J. Phys. Oceanogr.*, 13, 1018– 1036.

Toggweiler, J. R., Dixon, K., & Bryan K. (1989). Simulation of radiocarbon in coarse-resolution World Ocean model. Part I: steady state prebomb distributions, *J. Geophys. Res.*, 94, 8217–8242.

Tourre, Y. M., White, W.B. (1995). ENSO signals in global upperocean temperature. *J. Phys. Oceanogr.*, 25, 1317–1332.

Uppala, S. M., Kallberg, P.W., Simmons, A. J., Andrae, U., Bechtold, V.D, Fiorino, M., Gibson, J.K., Haseler, J., Hernandez, A., Kelly, G.A., Li, X., Onogi, K., Saarinen, S., Sokka, N., Allan, R.P., Andersson, E., Arpe, K., Balmaseda, M.A., Beljaars, A.C.M., Van De Berg, L., Bidlot, J., Bormann, N., Caires, S., Chevallier, F., Dethof, A., Dragosavac, M., Fisher, M., Fuentes, M., Hagemann, S., Holm, E., Hoskins, J., Isaksen, L., Janssen, P.A.E.M., Jenne, R., McNally, A.P., Mahfouf, J.F., Morcrette, J.J., Rayner, N.A., Saunders, R.W., Simon, P., Sterl, A., Trenberth, K.E., Untch, A., Vasiljevic, D., Viterbo,

P., & Woollen, J. (2005). *The ERA-40 re-analysis*. *Q. J. R. Meteorol. Soc.*, 131, 2961-3012

Verdon D. C., Franks, S. W. (2005). Indian Ocean sea surface temperature variability and winter rainfall: Eastern Australia, *Water Resour. Res.*, 41, W09413, doi: 10.1029/2004WR003845.

von Storch, H. & Zwiers F.W. (1999). *Statistical analysis in climate research*. Cambridge University Press, 484 pp.

Wallace, J. M., Rasmusson E. M., Mitchell T. P., Kousky T. V., Sarachik E. S., & von Storch H. (1998). On the structure and evolution of ENSO-related climate variability in the tropical Pacific: lessons from TOGA. *J. Geophys. Res.*, 103, 14241—14259

Wang, C. (2001). A unified oscillator model for the El Niño–Southern Oscillation, *J. Climate*, 14, 98–114

———, & An S. I. (2001), Why the properties of El Niño changed during the late 1970s. *Geophys. Res. Lett.*, 28, 3709--3712.

———, R. H. Weisberg, & J. I. Virmani (1999). Western Pacific interannual variability associated with the El Niño–Southern Oscillation. *J. Geophys. Res.*, 104, 5131–5149.

———, (1995), Interdecadal Changes in El Niño Onset in the Last Four Decades. *J. Climate*, 8, 267--285.

Wardle, R., & Smith, I. N. (2004). Modeled response of the Australian monsoon to changes in land surface temperatures. *Geophys. Res. Lett.*, 31, L16205, doi:10.1029/2004GL020157

Webster, P. J., Moore, A., Loschnigg, J. P., & Leben, R. R. (1999). Coupled oceanic–atmospheric dynamics in the Indian Ocean during 1997–1998. *Nature*, 401, 356–360.

Weisberg, R. H., & C. Wang (1997). A western Pacific oscillator paradigm for the El Niño–Southern Oscillation. *Geophys. Res. Lett.*, 24, 779–782.

Whetton, P. H., England, M. H., O’Farrell, S. P., Watterson, I. G. & Pittock, A. B. (1996). Global comparison of the regional rainfall results of enhanced greenhouse coupled and mixed layer ocean experiments: Implications for climate change scenario development, *Climatic Change*, 33, 497–519.

Wijffels, S., & Meyers G. (2004). An Intersection of oceanic wave guides: Variability in the Indonesian throughflow region. *J. Phys. Oceanogr.*, 34,1,232–1,253.

Wyrtki, K. (1987). Indonesian throughflow and the associated pressure gradient. *J. Geophys. Res.*, 92(C12), 12941-12946.

———, (1985). Water displacements in the Pacific and the genesis of El Niño cycles. *J. Geophys. Res.*, 90, 7129-7132.

———, (1975). El Niño—The dynamic response of the equatorial Pacific ocean to atmospheric forcing. *J. Phys. Oceanogr.*, 5, 572–584.

Yamagata, Behera, T., S. K., Luo, J.J., Masson, S. Jury, M. R., & Rao, S. A. (2004). *Coupled Ocean-Atmosphere variability in the Tropical Indian Ocean, Earth's climate: The Ocean-Atmosphere Interaction Geophysical Monograph Series*. 147, doi:10.1029/147GM12, Eds. by Wang, C., S.-P. Xie, and J.A. Carton.

# List of Figures

Figure 1.1: Cerberus (three-headed dog) of the Australian Climate: one head is ENSO (higher temperature in the equatorial Pacific), the second head is the IOD (higher temperature in the west and lower in the east of the Indian Ocean), and the third head is the SAM (oscillating SLP between high and midlatitudes). The ENSO anomaly pattern is obtained by regressing SST anomalies using Globe Sea Ice and Sea Surface Temperature data (GISST, Rayner et al., 1996) on an ENSO index, Niño3.4, which is defined as SST anomaly averaged over 170°W-120°W, 5°S -5°N. The IOD anomaly pattern is obtained from EOF analysis on SST anomalies, and the SAM is the EOF1 of NCEP mean SLP anomaly (Kalnay et al., 1996).

Figure 1.2: Total rainfall trend over the period 1950-2002 (courtesy of BMRC).

Figure 1.3: Relationship between winter rainfall anomalies over MDB region and winter eastern Indian Ocean SST anomalies (averaged over an area bounded by 5°S-10°S and 100°E-110°E), and between winter rainfall anomalies over MDB region and winter Niño3.4 index. The figure shows that for MDB region, the winter rainfall is influenced more by SST in the eastern Indian Ocean.

Figure 1.4: Time series of summer NWA rainfall in terms of percentage of climatology. NWA is defined as the area of 110°E-130E, 10°S-20°S.

Figure 1.5: Wind-drive ocean circulation (in Sv,  $1 \text{ Sv} = 10^{-6} \text{ m}^3 \text{ s}^{-1}$ ) calculated using NCEP winds, a) over the period of 1948-1967, and b) over the period of 1981-2000. The comparison shows a stronger EAC flow passing the Tasman Sea, consistent with what is predicted by couple climate models.

Figure 2.1: Upper panel, illustration of the Island Rule in the Indo-Pacific system, superimposing on annual mean winds. Three islands are included. For island such as Australasia, the circulation around the island can be obtained from the path integral of the wind stress around a path like the red loop QRST. Lower panel, transport in (absolute value) using NCEP monthly mean winds for Australasia, which is the modeled Indonesian Throughflow.

Figure 2.2: Time [years] required for the long baroclinic Rossby waves to traverse the South Pacific Ocean from the eastern boundary (from Qiu and Chen, 2006). Notice that the contour intervals are not uniform.

Figure 2.3: Wind-driven climatological circulation for southern summer (upper panel) and southern winter (lower panel) based on NCEP winds. Unit in Sv ( $1 \text{ Sv} = 10^6 \text{ m}^3 \text{ s}^{-1}$ ).

Figure 2.4: a) Difference in 20-year averaged wind stress curl ( $\text{N m}^{-3}$ ) based on ERA40 winds, and b) thermocline depth (m) between the pre- and post-1980 period (post-1980

minus pre-1980) based on the Simple Ocean Data Assimilation (SODA) (Carton and Giese, 2007).

Figure 2.5: Decadal difference in wind-driven circulation (1981-2000 average minus the 1960-1980 average). Unit in Sv. The post-1980 period features stronger ENSO, with greater discharge of heat from the equatorial Pacific to the tropical latitudes.

Figure 3.1: Evolution of normalized D20 anomaly pattern obtained from CEOF analysis in the whole Indo-Pacific domain covering half of an ENSO cycle at a phase interval of  $22.5^\circ$ . Negative values are in dashed contour.

Figure 3.2: The relationship between D20 anomalies at the central WA coast ( $114^\circ$ - $118^\circ$ E,  $17^\circ$ - $22^\circ$ S) and gridpoint D20 and zonal wind stress anomalies at various lags with a 3-month interval. To show a discharge signal at the WA coast at Lag 0, the WA time series is sign-reversed before analysis. Positive correlations imply deeper depths, and negative lags mean the WA D20 lags.

Figure 3.3: Time series of D20 anomaly at the central WA coast (thick solid) and at off-equatorial NP (thin solid) ( $150^\circ$ - $155^\circ$ W,  $17^\circ$ - $22^\circ$ N). Since the WA time series lags that of the NP by 9 months, the NP time series is shifted forward by 9 months to maximize the correlation. (From Cai et al., 2005c).

Figure 3.4: Time series of D20 anomalies at the central WA coast (black) wind stress anomalies in the Niño3.4 ( $120^\circ$ - $170^\circ$ W,  $5^\circ$ S- $5^\circ$ N) region (red, rescaled for plotting) and D20 anomalies in the SEWP ( $155^\circ$ - $160^\circ$ E,  $0^\circ$ - $5^\circ$ S) region (dashed, rescaled for plotting by multiplying a factor of 0.5 because of larger amplitude than the WA D20 time series). (From Cai et al., 2005c).

Figure 3.5: Comparisons of SODA and GISST data. Black line represents SODA, while red line represents GISST.

Figure 3.6: Outputs from the SODA-POP reanalysis (Version 1.4.2), showing correlation between Niño3.4 and gridpoint D20 at various lags with a 3-month interval. Positive correlations imply deeper depths, and negative lags mean the Niño3.4 lags. Left column is for the post-1980 and right column for the pre-1980 period. A value of 0.28 indicates statistical significance at 95% confidence level (from Shi et al., 2007)..

Figure 3.7: The same as Figure 3.6, but with time series of D20 in a Philippine Sea (PS) box ( $120^\circ$ E- $125^\circ$ E,  $12.5^\circ$ N- $17.5^\circ$ N). To show discharge signals the PS D20 is sign-reversed before analysis for comparisons with Figure 3.6.

Figure 3.8: The same as Figure 3.7, but with time series of D20 averaged over a central WA box ( $112^\circ$ E- $120^\circ$ E,  $15^\circ$ S- $22^\circ$ S). To show discharge signals the WA D20 is sign-reversed before analysis for comparisons with Figure 3.6 (from Shi et al., 2007).

Figure 3.9: Coupled model results: a), time series of correlation between Niño3.4 and the WAD20 at Lags +3 (black curve) and +6 (blue) (i.e., 3 months and 6 months, respectively, after an ENSO event peaks), and time series of standard deviation of Niño3.4 (red curve), calculated using a 20-year sliding window; b) and c), patterns of one-standard deviation anomalies of SST and zonal wind associated with ENSO for a strong transmission period (year 315); d) and e), the same as b) and c) but for a weak transmission period (year 215).

Figure 3.10 Maps of “signal to noise” ratio defined as the standard deviation of a signal over the standard deviation of noise for the coupled model (left column) and SODA-POP (right column) in terms of D20. See text for details. Upper row shows patterns for a strong transmission period (model year 315, and post-1980) while lower row shows those for a weak transmission period (model year 215 and pre-1980 SODA) (from Cai et al., 2007).

Figure 3.11: (a) Observed zonally averaged temperature trend since 1960 ( $^{\circ}\text{C}$  per 50 years). (b) The same as (a) but in a model ensemble (eight members) with all forcing including solar variability, volcanic, ozone, increasing aerosols, increasing  $\text{CO}_2$ . (c) The same as (b), but with aerosol fixed at pre-industrial level (from Cai et al., 2007)..

Figure 4.1: Observed annual total rainfall trend (mm) based on the BMRC rainfall data over 1951-2000. Blue colour shows rainfall increase and red indicates rainfall reduction. The area in the Northwest corner (dotted line) is defined as NWA in this paper.

Figure 4.2: Observed climatology (left column) and trend (right column) of seasonal total rainfall (mm) over 1951-2000. The data are stratified into December-January-February (DJF), March-April-May (MAM), June-July-August (JJA), and September-October-November (SON).

Figure 4.3: Map of correlation between NWA rainfall and grid-point SST (both linearly detrended) for each season using data for the 1951-2000 period. Correlation coefficients greater than 0.28 are significant at a 95% confidence level.

Figure 4.4: Maps of correlation of Australian rainfall with Niño3.4 (left column) and with EIO SST (right column) for each season using data for the 1951-2000 period (from Shi et al., 2008b).

Figure 4.5: Patterns of SST (GISST, in  $^{\circ}\text{C}$   $^{\circ}\text{C}^{-1}$ ) and wind (NCEP, maximum vector 0.02  $\text{N m}^{-2}$   $^{\circ}\text{C}^{-1}$ ) anomalies associated with ENSO. These are obtained by regressing linearly detrended SST and wind fields onto linearly detrended Niño3.4 (from Shi et al., 2008b).

Figure 4.6: Patterns associated with detrended DJF rainfall EOF after removing variances associated with ENSO (see text for details) in the domain of  $110^{\circ}\text{E}$ - $135^{\circ}\text{E}$ ,  $10^{\circ}\text{S}$ - $25^{\circ}\text{S}$  (from Shi et al., 2008b). These patterns are obtained by regressing grid-point Australia rainfall anomalies onto the time series of the EOF1 and EOF2.

Figure 4.7: SST patterns associated with EOF1 and EOF2 shown in Fig. 4.6 (from Shi et al., 2008b). Shown are obtained by regressing SST anomalies onto the time series of the EOF1 and EOF2. Units are °C per unit of the EOF time series.

Figure 4.8: Anomaly patterns of MSLP (mb per unit of EOF time series) and winds ( $\text{N m}^{-2}$  per unit of EOF time series) associated with EOF1 and EOF2 shown in Fig. 4.6 (from Shi et al., 2008b). Shown are obtained by regressing anomalies onto the rainfall time series of the EOF1 and EOF2. The regression coefficients of surface winds are plotted as vectors.

Figure 4.9: The same as Fig. 4.8, but for cloud cover (from Shi et al., 2008b).

Figure 4.10: DJF total rainfall trends (mm) over 1951-2000 projected onto EOF1 (a) and EOF2 (b), and the sum of them (c) (from Shi et al., 2008b). Since these trends are obtained by projecting onto DJF rainfall with variance associated with ENSO removal, the ENSO related trend is generated and added to (c) to yield (d).

Figure 4.11: Panel a), SST trend (°C) resulting from the sum of trends associated with DJF rainfall EOF1 and EOF2 of DJF rainfall shown in Fig. 4.6. These trends are calculated by projecting raw DJF SST anomalies onto time series of the DJF rainfall EOFs (see text for details). Panel b), the total trend of raw SST. Panels c) and d), the same as a) and b) except for MSLP. A uniform value  $0.35^{\circ}\text{C}$  is taken out from b) and a value of 1.4 mb is subtracted from d), respectively (from Shi et al., 2008b).

Figure 4.12: Model climatology (left column) from a 300-year control experiment of seasonal total rainfall (mm) and trend (right column) in seasonal total rainfall (mm) for 1951-2000. The data are stratified into December-January-February (DJF), March-April-May (MAM), June-July-August (JJA), and September-October-November (SON) (from Shi et al., 2008b).

Figure 4.13: Map of correlation between modeled NWA rainfall and model grid-point SST (both linearly detrended) for each season using outputs from a 300-year control experiment. Correlation coefficients greater than 0.12 are significant at a 95% confidence level (from Shi et al., 2008b).

Figure 4.14: Maps of correlation of Australian rainfall with Niño3.4 (left column) and with EIO SST (right column) for each season using outputs from a 300-year control experiment model outputs (from Shi et al., 2008b).

Figure 4.15: Panel a), pattern of model SST ( $^{\circ}\text{C } ^{\circ}\text{C}^{-1}$ , contour) and wind ( $\text{N m}^{-2} \text{ } ^{\circ}\text{C}^{-1}$ , vectors) anomalies associated with model ENSO-like variability. These are obtained by regressing model SST and wind anomalies onto the model Niño3.4 index in the 300-year control experiment. Panel b), EOF2 (16.8% of the remaining variance) of model SST and the associated model wind fields (vectors) after removing variance associated with ENSO-like variability, and c), correlation between time series of model EOF2 shown in b) and model rainfall.

Figure 4.16: Patterns of model rainfall EOF after removing variances associated with ENSO and IOD (see text for details). Patterns are obtained by regressing rainfall anomalies onto the time series of the model EOF1 and EOF2 in the domain of 110°E-135°E, 10°S-25°S. EOFs 1 and 2 account for 47.6% and 20.7% of the remaining variance.

Figure 4.17: SST patterns associated with model rainfall EOF1 and EOF2 shown in Fig. 4.16. Patterns are obtained by regressing model SST anomalies onto the time series of the EOF1 and EOF2 (from Shi et al., 2008b).

Figure 4.18: Anomaly patterns of MSLP (mb per unit of EOF time series) and winds ( $\text{N m}^{-2}$  per unit of EOF time series) associated with DJF rainfall EOF1 and EOF2 in the 300-year control experiment. Patterns are obtained by regressing model MSLP anomalies onto the time series of the rainfall EOFs (from Shi et al., 2008b).

Figure 4.19: As in Figure 4.18, but for the cloud cover (from Shi et al., 2008b).

Figure 4.20: Panel a), Model DJF SST trend pattern ( $^{\circ}\text{C}$ ) with all anthropogenic forcing imposed (ALL ensembles). Panel b), total trend (mm) of the DJF rainfall estimated from the unrealistic relationship between EIO SST and Australian rainfall in the 300-year control experiment (from Shi et al., 2008b).

Figure 4.21: Panel a), Observed DJF SST anomalies ( $^{\circ}\text{C}$ ) over EIO against NWA rainfall (mm). Panel b), the same as a) but from the 300-year control experiment.

Figure 4.22: Time series of 50-year trends of NWA DJF rainfall obtained using a sliding window applied to the multi-century control experiment of Mk3.5 without climate change forcing, a) total 50-year trend, and b) percentage of climatology.

Figure 5.1: Ensemble-mean change averaged over the period of 2055-2085, a) zonal wind stress ( $\text{N m}^{-2}$ ), b) wind stress curl ( $\text{N m}^{-3}$  scaled by a factor of  $10^{-6}$ , and c) vertically integrated barotropic streamfunction (Sv,  $1 \text{ Sv} = 10^6 \text{ m}^3 \text{ s}^{-1}$ ). Note that compared to panels (b) and (c), panel (a) has a  $5^{\circ}$  southerly shift to show the maximum wind change is at  $60^{\circ}\text{S}$ . The pattern correlation coefficients between individual ensemble members are in the range of 0.95-0.98 for a), 0.87-0.95 for b), and 0.93-0.99 for c) (from Cai et al., 2005).

Figure 5.2: Transport streamfunction (Sv) from Godfrey's Island Rule model forced by model winds from, a) control experiment, b) ensemble-mean of warming experiments averaged over 2055-2085, and c) difference between b) and a). The pattern correlation coefficients between individual ensemble members are in the range of 0.95-0.98 for zonal wind stress change and 0.87-0.96 for meridional wind stress change.

Figure 5.3: Change in transport streamfunction (Sv) from Godfrey's Island Rule model forced by model winds as the difference between the control experiment and ensemble-mean of warming experiments averaged over 2055-2085.

Figure 5.4: Time series of latitude in which the model EAC reaches a maximum in one experiment.

Figure 5.5: Rainfall changes (a) in  $\text{mm day}^{-1}$  and (b) in percentage of control climatological values. Left column is for summer (December – February, DJF) and right column is for winter (June – August, JJA).

Figure 5.6: Correlation between time series of east coast rainfall (averaged over  $150^{\circ}\text{E}:155^{\circ}\text{E}$ ,  $33^{\circ}\text{S}:38^{\circ}\text{S}$ ) and rainfall everywhere (a), SST (b), and MSLP and wind vectors (c). Left column is for summer and right column is for winter. An absolute value greater than 0.115 is statistically significant at a 95% confidence level. Maximum vector represents a value of 1.4.

Figure 5.7: Correlation between time series of east coast SST (averaged over  $150^{\circ}\text{E}:155^{\circ}\text{E}$ ,  $33^{\circ}\text{S}:38^{\circ}\text{S}$ ) and grid-point rainfall (a) and SST (b). Left column is for summer and right column is for winter.

Figure 5.8: The same as in Fig. 5.7, but between NINO3.4 grid-point rainfall (a) and SST (b).

Figure 5.9: The same as in Fig. 5.7, but between IO SST EOF1 and grid-point rainfall (a) and SST (b).

Figure 5.10: The same as in Fig. 5.6, but between MSLP EOF1 (the SAM) time series and circulation fields.

Figure 5.11: Changes of MSLP (hPa) in the warming experiments from the control climate averaged over a 31-year period between 2055 and 2085 (a), and pattern of MSLP EOF1 in the control experiment.

Figure 5.12: Changes averaged over a 31-year period between 2055 and 2085 of (a) SST ( $^{\circ}\text{C}$ ), (b) longwave radiation at the top of the atmosphere ( $\text{W m}^{-2}$ ), and (c) surface shortwave radiation ( $\text{W m}^{-2}$ ). Left column is for summer and right column is for winter.

Figure 5.13: Rainfall changes (in  $\text{mm day}^{-1}$ ) for all seasons, (a) DJF, (b) MAM, (c) JJA, and (d) SON.

# Glossary and Acronyms

**ALL:** experiment included all forcing

**AXA:** all forcing except those related to anthropogenic aerosols

**BC:** black carbon

**BMRC:** the Australian Bureau of Meteorological Center

**CEOF:** complex empirical orthogonal function

**D20:** 20<sup>0</sup>C isotherm

**DJF:** December, January, February.

**ENSO:** El Niño-Southern Oscillation. Acronym for El Niño–Southern Oscillation, coined in the early 1980s in recognition of the intimate linkage between El Niño events and the Southern Oscillation, which prior to the late 1960s had been viewed as two unrelated phenomena. The global ocean–atmosphere phenomenon to which this term applies is sometimes referred to as the “ENSO cycle.”

**El Niño:** a term originally used to describe the appearance of warm (surface) water from time to time in the eastern equatorial Pacific region along the coasts of Peru and Ecuador

**EAC:** East Australian Current

**EIO:** Eastern Indian Ocean.

**EOF:** empirical orthogonal function

**GCM:** General Circulation Model.

**GISST:** Globe Sea Ice and Sea Surface Temperature.

**JJA:** June, July, August

**Kelvin wave:** a type of low-frequency gravity wave trapped to a vertical boundary, or the equator, which propagates anticlockwise (in the Northern Hemisphere) around a basin. The flow is parallel to the boundary and in geostrophic balance with the pressure gradient perpendicular to the boundary.

**La Niña:** the appearance of colder-than-average sea surface temperatures (SSTs) in the central or eastern equatorial Pacific region (the opposite to conditions during El Niño).

**IO:** Indian Ocean

**IOD:** Indian Ocean Dipole, a warm water region in the area around Indonesia and New Guinea, and a relatively colder region in the central Indian Ocean west of Australia, giving rise to rain-producing systems that extend across Australia from north-west to south-east.

**IOCI:** Indian Ocean Climate Initiative, a climate research program established by the Western Australian Government in collaboration with the BMRC and CSIRO to identify the causes of the serious rainfall decreases and the consequential impact on water resources experienced in southwest Western Australia since the 1970s.

**IOTA:** Indian Ocean Thermal Archive

**IPCC:** Intergovernmental Panel on Climate Change.

**MAM:** March, April, May

**MDB:** Murray Darling Basin

**MOM:** Modular Ocean Model

**MSLP:** mean sea level pressure. The atmospheric pressure at mean sea level, either directly measured or, most commonly, empirically determined from the observed station pressure.

**NCEP:** National Centre for Environmental Prediction

**NINO3.4 index:** the average sea surface temperature anomaly in the region bounded by 5°N to 5°S, from 170°W to 120°W. This region has large variability on El Niño time scales, and is close to the region where changes in local sea-surface temperature are important for shifting the large region of rainfall typically located in the far western Pacific.

**NP:** North Pacific

**NWA:** North West Australia.

**POM:** particulate organic matter

**Rosby waves:** large-scale motions in the ocean or atmosphere whose restoring force is the variation in Coriolis effect with latitude. The waves were first identified in the atmosphere in the 1939 by Carl-Gustaf Arvid Rossby who went on to explain their motion.

**SAM:** Southern Annular Mode, also referred to as Antarctic Oscillation (AAO). It is the dominant pattern of non-seasonal tropospheric circulation variations south of 20°S, and it

is characterized by pressure anomalies of one sign centered in the Antarctic and anomalies of the opposite sign centered about 40°S -60°S.

**SEA:** South East Australia

**SH:** Southern Hemisphere

**SODA-POP:** Simple Ocean Data Assimilation - parallel Ocean Programme

**Southern Oscillation Index:** an indicator based on the pressure gradient between the quasi-stationary low pressure region over Indonesia and the centre of the subtropical high pressure cell over the eastern Pacific Ocean; traditionally, Darwin and Tahiti are used as the sites for determining the magnitude of the Southern Oscillation; a negative SOI is associated with higher than normal pressures over Darwin and drought conditions over much of eastern Australia.

**SON:** September, October, November

**SST:** sea surface temperature.

**SWWA:** southwest Western Australia.

**Thermocline:** The transition layer between the mixed layer at the surface and the deep water layer. The definitions of these layers are based on temperature.

**WA:** Western Australia

**XBT:** expendable bathythermograph. XBT has been used by oceanographers for many years to obtain information on the temperature structure of the ocean to depths of up to 2000 meters.